Vortex Imaging in Novel Superconductors

Desoky, Waled

Award date:
2013

Awarding institution:
University of Bath

Vortex Imaging in Novel Superconductors

Submitted by

Waled Mohamed Ahmed Desoky

A thesis submitted for the degree of Doctor of philosophy

Department of Physics

University of Bath

June 2013

COPYRIGHT

Signed:

Waled Desoky

Acknowledgment

I would like to thank my supervisor Professor Simon Bending for his never-ending patience, encouragement, generous support, helpful guidance and understanding during my PhD project. Many thanks for Dr. Alessandro Narduzzo's help including project discussion and the sharing of expertise. Also, I would like to thank the Egyptian government for funding and continuous care and support. Thanks also to all staff members of the Physics Department for their collaboration. Appreciations go to my Mum, Dad, and sisters and all other members of my family. I'll not forget my wife for her patience and continuous support.

Abstract

High resolution scanning Hall probe microscopy and Hall magnetometry have been used to investigate the magnetic properties of single crystal samples of Co-doped Sr-122 and Ba-122 iron- based superconductors and high quality MgB_2 thin films. We have made a quantitative analysis of the evolution of the profiles of well-isolated vortices as a function of temperature, and used a fitting procedure to extract the temperature-dependent magnetic field penetration depth, $\lambda(T)$. This, in turn, allowed us to infer the temperature-dependent superfluid density which has been compared with α-model results for a two band superconductor. Fit parameters yield insights into the symmetry of the order parameter at the electron and hole pockets as well as the relative contributions of the bands to the superfluid density in the iron-based crystals. Vortex imaging and 'local' magnetisation measurements, with a static Hall probe parked just above the sample surface, also yielded important information about the distribution of pinning sites, the strength of vortex pinning and the possible presence of material inhomogeneities in all samples. Finally, we have investigated vortex spatial distributions over large areas in high quality MgB_2 thin films using our mK SHPM. A careful statistical analysis of vortex positions in these films shows unusual anisotropies, with evidence of a second weak peak in the nearest neighbour vortex-vortex bond length distribution at small distances. This result was completely unexpected as one would predict such 'type 1.5 superconductivity' effects to be suppressed by strong scattering in MgB_2 thin films.

Table of Contents

List of figures

List of tables

Chapter One: Introduction

1.1. Motivation

Iron-based superconductors form a new class of high temperature superconductors that were discovered in February 2008. The astonishing thing about these new material families is that they contain iron, an element normally associated with ferromagnetism rather than superconductivity (which is generally destroyed by ferromagnetic order). The high upper critical fields and relatively high critical current density in this group are good evidence that these compounds can be competitive with MgB_2 and even high critical temperature (T_c) cuprates. Moreover, the first high temperature superconductors, the cuprates, have been studied intensively for more than 20 years, but scientists still do not understand the microscopic mechanism at work. Finding the first non-cuprate high temperature superconductors can help to unveil the mystery of superconductivity and it is possible that the clues as to how these materials work could lead to the design of room temperature superconductors.

Magnesium diboride (MgB_2) is unlike any other known superconductor and has surprising and unique properties, it has a very high critical temperature (~39K), simple structure (intermetallic compound), a limited grain boundary weak-link problem relative to cuprate superconductors, an upper critical field that is much higher than most superconducting magnets that are currently used, and is made of inexpensive elements. Finally it was the first material to show multiple gap phenomena on different bands and many theoretical and experimental studies suggest a new vortex interaction potential (type 1.5) which leads to the formation of vortex “islands” and “labyrinths” due to the existence of short-range repulsion and long range attraction (i.e. effectively type-1 and type-2 simultaneously). All of these properties of MgB_2 have excited strong interest amongst scientists in recent years as it believed that they may play key roles in applications in the near future.

The initial preparation work in this research project was the successful fabrication of sub-micron GaAs/AlGaAs Hall sensors for scanning Hall probe microscopy. This was performed in the Nanofabrication Facility using optical and electron beam lithography and chemical etching. Completed devices showed excellent signal-to-noise characteristics and good spatial resolution at low temperatures.

The first research objective was to perform detailed vortex-resolved imaging studies of 122 iron-pnictide single crystal samples as a function of temperature and magnetic field intensity using Hall probe microscopy. Single crystal samples were provided through collaborations with groups in Cambridge and Tokyo. The ultimate goal of this work is to infer as much as possible about the mechanism of superconductivity by measuring the temperature dependence of the penetration depth and superfluid density in these samples. In addition, the low field pinning forces have been investigated by studying the deviation of vortex structures from an ideal triangular lattice.

The second objective was to study the temperature-dependent penetration depth and superfluid density in MgB_2 thin films. Experimental data were then fitted to a two-band α-model. In addition, we have investigated vortex spatial distributions over large areas in these high quality MgB_2 thin films provided by collaborators at MIT. Statistical distributions of nearest neighbour vortex-vortex distances after Delaunay triangulation show unusual anisotropies, with evidence of a bi-modal histogram in the vortex-vortex distribution. This result was completely unexpected as one would predict type 1.5 effects to be completely suppressed by disorder (short mean free path) in MgB_2 thin films.

1.2. Structure

The thesis is divided into six chapters: chapter two presents a broad overview of some of the most fundamental experimental properties of superconductors, together with key theories (the London equation, John Bardeen, Leon Neil Cooper and John Robert Schrieffer (BCS) theory and

Ginzburg-Landau theory) of superconductivity that describe the superconducting length scales and the energy gap. These are fundamental in determining the behaviour of superconductors. The significant differences observed in type I and type II superconductors are explained and the behaviour of vortices in the latter discussed. Chapter two also includes a brief introduction to iron-pnictide superconductors and MgB_2, including the crystal and band structures as well as the physical properties of both compounds.

An overview of the individual imaging techniques for the mapping of magnetic fields in superconducting samples is presented in chapter three along with a detailed description of the scanning Hall probe microscope.

Chapter four introduces the basic principles and technology of Hall effect sensors. It also describes the fabrication processes used to make sub-micron GaAs/AlGaAs Hall sensors for low temperature scanning Hall probe microscopy (SHPM). The same technique can be used to record local magnetic images of superconducting and ferromagnetic materials.

In chapter five, studies of temperature- and field-dependent vortex structures in Co-doped $SrFe_2As_2$ and Co-doped $BaFe_2As_2$ (with different concentrations) single crystals grown in Cambridge and Tokyo are described. Careful fitting of the vortex profiles has allowed insights into the symmetry of the order parameter in the electron and hole pockets responsible for superconductivity in this multiband material via estimates of the temperature dependence of the superfluid density. In addition, distortions to the ideal vortex lattice have been quantified to generate lower bounds on typical pinning forces in these materials.

Chapter six extends the study of field-dependent vortex structures and temperature-dependent superfluid density to MgB_2 thin films. Investigations have been made of broken symmetry vortex structures over large areas in high quality thin films of this two-band superconductor with different thicknesses. A careful statistical analysis of the vortex positions in these films reveals unusual anisotropies, with evidence of bi-modal peaks in the vortex-vortex bond length distribution, a result that was completely

unexpected as one would predict such type 1.5 effects to be suppressed by strong scattering in MgB_2 thin films. Finally, chapter seven presents the final conclusions and future prospects.

Chapter two: Introduction to Superconductivity

2.1. A brief history of superconductivity

The phenomenon of superconductivity was discovered in 1911 by Heike Kamerlingh Onnes when he studied the resistivity of mercury as a function of the temperature down to liquid Helium temperature. He found that the electrical resistivity of mercury suddenly dropped to zero when the sample was cooled to 4.2K, as shown in figure 1[1]. In the following years, superconductivity was observed in many elements in the periodic table such as tin and lead at very low temperatures; these elements are often called the simple elemental superconductors.

The next generation of superconducting materials were the intermetallic compounds, such as niobium-tin, vanadium-silicon and niobium-titanium, which were discovered during the 1930s, with the highest critical temperature being 23 K for niobium-germanium Nb_3Ge [2]. In addition to the absence of resistivity, the diamagnetic properties of superconducting materials (Meissner effect) were discovered by Meissner and Ochsenfeld in 1933 [3]. After that the London brothers derived their London equations to describe the Meissner effect and extract the London penetration depth [4].

In the 1950s, two aspects of superconductivity were explored for the first time, its macroscopic and microscopic properties. The macroscopic theories were developed by the Soviet scientists Ginzburg and Landau (G-L theory) [5], who phenomenologically discussed superconductivity based on the concept of an order parameter (OP) and characteristic length scales. Using the G-L theory, Abrikosov showed that superconducting materials can be divided into two categories; Type-I and Type-II [6]. At approximately the same time, the first microscopic theory of superconductivity was developed by three American physicists: Bardeen, Cooper and Schrieffer, known as the BCS theory [7].

However, although this can describe the low temperature superconducting phenomenon, it cannot fully explain the existence of high temperature superconductivity.

In early 1986, two researchers, Johannes Bednorz and Karl Müller at the IBM research laboratories in Zürich, synthesised a new class of superconductors reaching T_c=30 K in the compound BaLaCuO. They described this discovery as that of a new class of superconducting materials (copper-oxide ceramics) and gave birth to a new era of high temperature superconductivity (HTSC) [8]. Following this, the highest T_c of these materials reached up to 133K [9], which encouraged researchers to attempt to discover other compounds having high T_c. However, HTSC has not yet been widely used due to intrinsic disadvantages such as high anisotropy weak links and the high cost of the raw materials when fabricated in tape form.

In 2001, superconductivity was discovered in MgB_2 at temperatures as high as 39K by Japanese scientists [10]. Several years later, in February 2008, another Japanese group discovered superconductivity in an Fe-As compound, LaFeAsO, with T_c=26K [11]. After this discovery, it was found that SmFeAsO, in which La is replaced with Sm, displays an even higher T_c of 55K [12]. As a result, a new and extremely interesting family of iron-based superconductors started to attract the attention of the superconductivity community (see figure 2) [13].

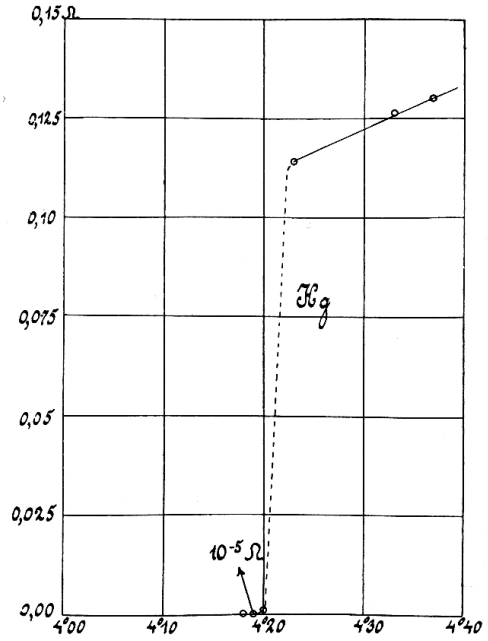

Figure 1: The phase transition of mercury from the normal state to the superconducting state [1].

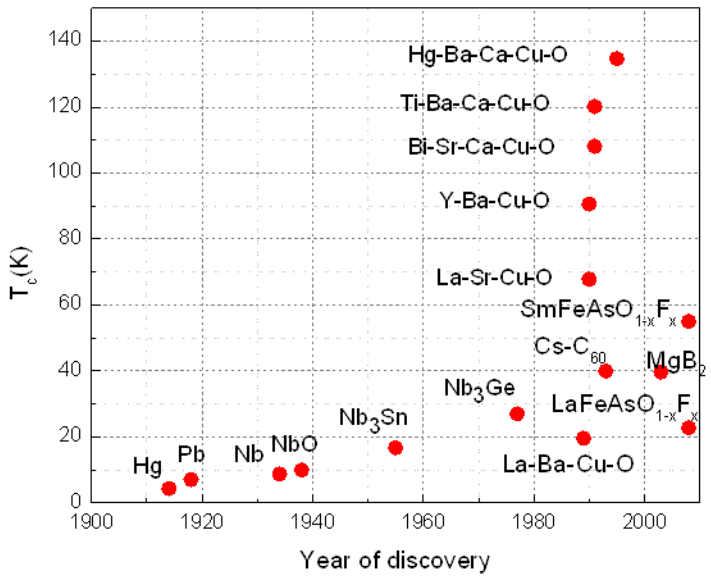

Figure 2: High temperature superconducting materials discovered since 1911 and their critical temperatures.

2.2. Properties of superconductors

Superconductors exhibit two distinctive properties, zero resistivity and the Meissner effect.

Zero resistivity

The first significant property of the superconducting phenomenon is the phase transition at the critical superconducting temperature, T_c, leading to zero electrical resistance (see figure 1). The best method to demonstrate the complete disappearance of resistance is through experiments with persistent supercurrents which can last for many years [1].

Meissner effect

The second important property of superconductors is the complete expulsion of magnetic fields; the magnetic flux density inside a superconductor remains zero when it is placed in a magnetic field and the susceptibility is χ =-1 (perfect diamagnetism). This phenomenon is called the Meissner effect, as mentioned above, which was discovered by Meissner and Ochsenfeld in 1933 [3].

There are two history-dependent features of perfect diamagnetism in superconductors:

The first known as Zero-Field Cooled (ZFC) measurements, refers to when the normal state is cooled below T_c without any magnetic field present and an external magnetic field is then applied creating supercurrents that screen the field from the superconductor. The second Field Cooled (FC) measurement is when a magnetic field is applied to the same material in its normal state and the field penetrates the material, thus leading to the some value of the magnetic induction inside and outside. The field is then expelled from the superconducting material when it is cooled below T_c.

The final results for both changes appear identical as shown in figure 3. This sketch also presents the effect of a magnetic field on normal metals[14]. Experimentally, the superconducting state is destroyed by a specific magnetic field, known as a critical magnetic field, H_c, which is related

thermodynamically to the free-energy difference between the normal and superconducting state in zero field. The critical magnetic field can also be produced by a critical transport current density, J_c, at the superconductor surface which drives the superconductor into the normal state. The critical magnetic field is often given by the empirical equation:

$$H_c(T) = H_c(0)\left(1 - \left(\frac{T}{T_c}\right)^2\right). \quad (2.1)$$

In general, the superconducting state is bounded by three critical parameters, as shown below; to sustain the superconducting state materials should be kept below their respective critical values. Figure 4 shows the superconducting state as a region beneath a curve known as the "critical surface" defined by the three critical parameters, J_c, B_c, and T_c, where $B = (H + M)\mu_0$:

- **The critical temperature**; materials remain in the normal state above this temperature and in a superconducting state below.
- **The critical magnetic field**; the external magnetic field for which the material exhibits a superconducting state below this value and the normal state above.
- **The critical current density**; corresponds to the current density at which dissipation begins to occur in the superconductor.

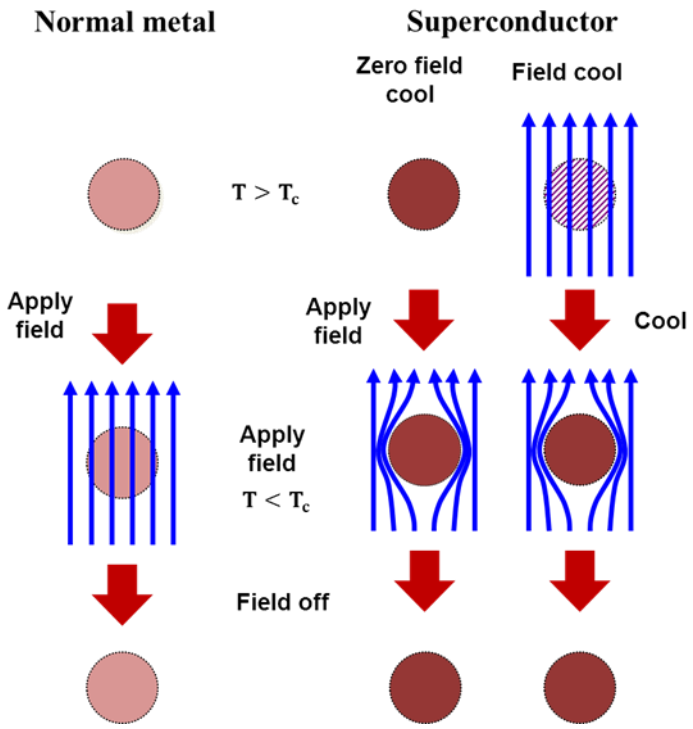

Figure 3: The effect of Zero-Field Cooling and Field Cooling on a normal and a superconducting metal.

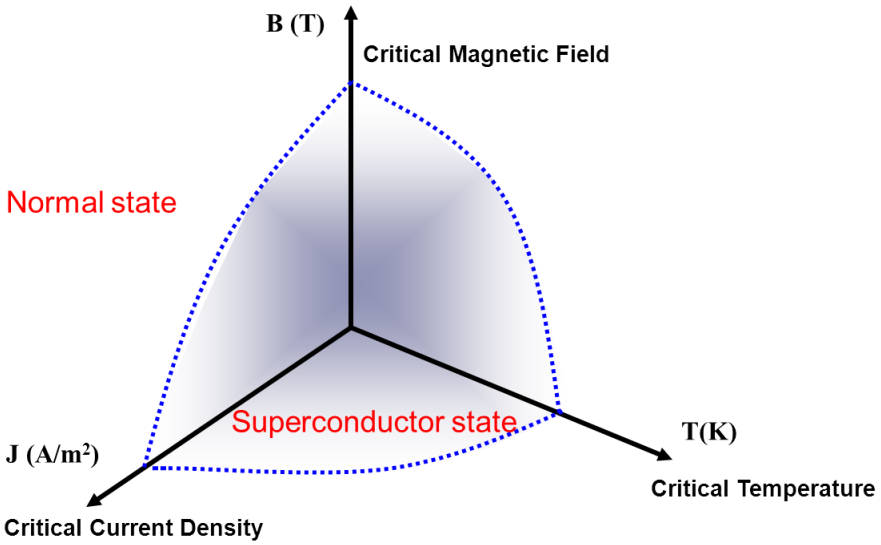

Figure 4: An illustration of a superconducting critical surface.

2.3. Theory of Superconductivity

The aim of this section is to illustrate the historical turning points in relation to the evolution of models and theories which make up the foundation of the physics of superconductors.

2.3.1. London equations

The London equations formed the first phenomenological theory of superconductivity and provide an understanding of perfect diamagnetism (Meissner effect) and the zero resistance of superconductors [4].

The London equations are based on the principle of the two fluid model [15] in which there is a mix of two kinds of electron density, normal, n_n, and superconducting, n_s , the total density of free electrons being given by $n_{total} = n_n + n_s$. The fraction of superconducting electrons increases with decreasing temperature below the critical temperature and at *T*=0K $n_{total} = n_s$. This indicates that superconductors below T_c are composed of two electron fluids, (normal electron fluid and the fluid of superelectrons), with the relative densities between the two fluids controlled by temperature [16]. The concept of the two fluid model was strongly supported at the time by thermodynamics as well as the results of various measurements [16].

The London brothers proposed two equations to describe the two fundamental phenomena of superconductivity [4]. Their development began with a description of the motion of superconducting electrons in an electric field, E, as given by

$$m\frac{dv_s}{dt} = eE, \tag{2.2}$$

where v_s, m, e and E are the velocity, mass and charge of the carriers and the constant electric field respectively. The supercurrent density can be defined as:

$$j_s = en_s v_s. \tag{2.3}$$

By substitution of equation 2.3 in equation 2.2, the first London equation becomes:

$$E = \frac{m}{e^2 n_s}\frac{dj_s}{dt}\,. \tag{2.4}$$

Equation 2.4 describes the zero resistance state (resistanceless), since any electric field accelerates the superconducting electrons rather than simply sustaining their velocity against resistance as described in Ohm's law in a normal conductor. By taking the curl of equation 2.4 and combining it with one of Maxwell's equations:

$$\nabla \times E = -\frac{dB}{dt}\,, \tag{2.5}$$

$$\frac{dB}{dt} = -\frac{m}{n_s e^2}\left(\nabla \times \frac{dj_s}{dt}\right). \tag{2.6}$$

The magnetic flux within the superconductors must be a constant with a value of zero; this can be only the case if B dies away rapidly with distance, so they assumed that equation 2.6 not only applies to dB/dt but to B itself.

$$B = -\frac{m}{n_s e^2}\nabla \times j_s. \tag{2.7}$$

Equation 2.7 is the second London equation which describes the diamagnetism exhibited by the superconductor. Using Maxwell's equation

$$\nabla \times B = \mu_0 j_s \tag{2.8}$$

and

$$\nabla \times (\nabla \times A) = \nabla(\nabla \cdot A) - \nabla^2 A, \tag{2.9}$$

equation (2.7) becomes

$$\nabla^2 B = \frac{1}{\lambda_L^2} B, \tag{2.10}$$

where the lengthscale λ_L (magnetic field penetration depth) is defined by:

$$\lambda_L = \sqrt{\frac{mc^2}{4\pi n_s e^2}}. \tag{2.11}$$

Here n_s , and λ_L are the number density of the superelectrons and the penetration depth respectively.

From equation 2.10, it can be seen that the external magnetic field decays exponentially with a characteristic length λ_L when a superconducting slab is in the presence of a magnetic field, In addition, the current density decays exponentially with the penetration depth to screen the magnetic field from the interior of the superconductor (see figure 5) [17]. The penetration depth λ_L depends on temperature due to the temperature dependence of n_s, and can often be approximated by the empirical formula given below and sketched in figure 6 [13]:

$$\lambda_L(T) = \frac{\lambda(0)}{\sqrt{1-(\frac{T}{T_c})^4}}, \tag{2.12}$$

where $\lambda(0)$ is the value of the penetration depth at 0 K.

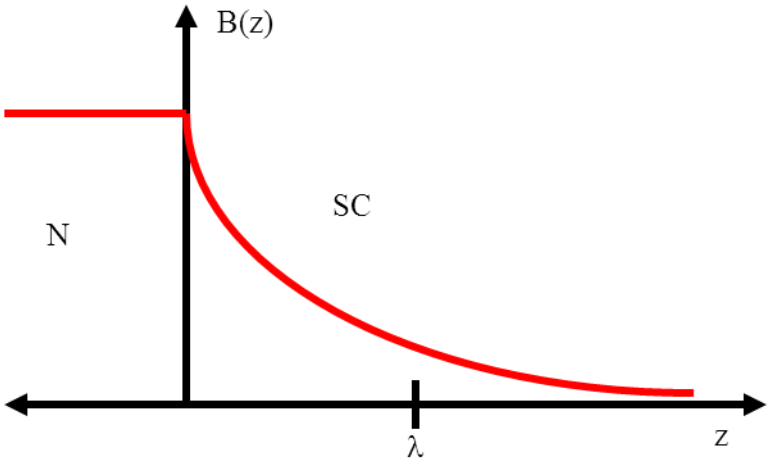

Figure 5: The behaviour of magnetic induction at the interface between a normal and a superconducting material.

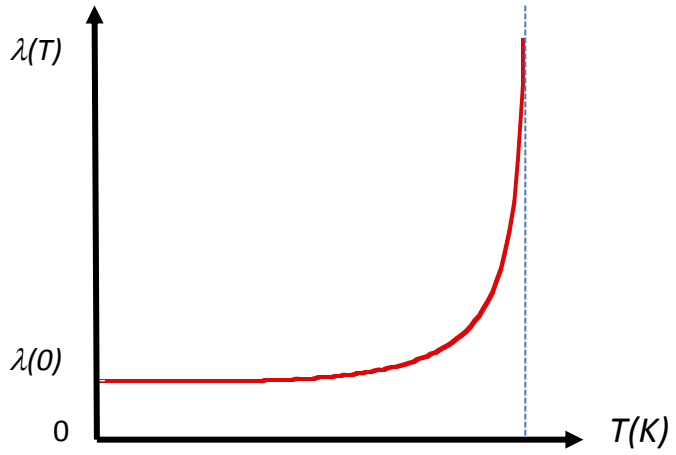

Figure 6: The temperature dependence of the penetration depth, *λ(T)*.

2.3.2. The Ginzburg-Landau Theory

Although the London theory provided a good semi-quantitative description of the Meissner effect and the electromagnetic properties of type-I superconductors, it cannot describe type II superconductors. In 1950, Ginzburg and Landau formulated a new phenomenological theory based on an order parameter, which provides a good macroscopic description of the superconducting state using quantum mechanics, while the London

theory is purely classical. The G-L theory assumes that the superconducting electrons, n_s, are described by an effective wavefunction ψ, and treated as a complex order parameter given by [5]:

$$n_s = |\psi|^2. \tag{2.13}$$

Ginzburg and Landau postulated that the free-energy density of the superconducting state, f_s can be expanded in powers of ψ, where the values of ψ and $\nabla\psi$ are small near T_c.

$$f_s = f_n + \alpha|\psi|^2 + \frac{\beta}{2}|\psi|^4 + \frac{1}{2m^*}\left|\left(\frac{\hbar}{i}\nabla - e^*A\right)\psi\right|^2 + \frac{\mu_o}{2}|H_a - H|^2, \tag{2.14}$$

where f_n is the free energy density of normal state, α and β are coefficients of the GL theory. H_a and H are the external applied magnetic field and the magnetic field within superconductor respectively. $e^* = 2\mathrm{e}$ and $m^* = 2m$ are the charge and mass of superconducting electron pairs respectively and A is the magnetic vector potential ($B = \nabla \times A$).

The most useful feature of GL theory for applications to inhomogeneous superconductors (such as type-II) is minimisation of the overall free energy of equation 2.14 by following a standard variational procedure, leading to the two Ginzburg-Landau differential equations:

$$\alpha\psi + \beta|\psi|^2\psi + \frac{1}{2m^*}\left(\frac{\hbar}{i}\nabla - e^*A\right)^2\psi = 0 \tag{2.15}$$

and

$$J_s = \frac{e^*\hbar}{2m^*i}(\psi^*\nabla\psi - \psi\nabla\psi^*) - \frac{e^*}{m^*}\psi^*\nabla\psi A. \tag{2.16}$$

Equation 2.15 takes the Schrödinger-like form with energy eigenvalue -α, while the equation 2.16 describes a superconducting current J_s in quantum-mechanical form.

In the case of an inhomogeneous superconductor in zero magnetic field, the equation (2.15) can be re-written as:

$$\psi + \frac{\beta}{\alpha}|\psi|^2\psi + \frac{\hbar^2}{2\alpha m^*}\nabla^2\psi = 0. \quad (2.17)$$

From equation 2.17, the coherence length can defined as $\xi(T) = \sqrt{\frac{\hbar^2}{2m^*|\alpha(T)|}}$

Finally, the theory contains two parameters, the penetration depth, λ, characterising the screening of the magnetic fields within the superconductor and the coherence length, ξ, which is the shortest characteristic scale over which the order parameter ψ can vary. The inclusion of a coherence length was an improvement over the London theory and allowed the description of the type II mixed state. G-L theory was able to calculate the S/N surface energy by incorporating quantum effects arising from the gradient of the wavefunction at the interface between a normal and a superconducting state (this will be discussed in detail in subsection 2.5). As a consequence, it predicts the existence of two different classes of superconductors known as type I and type II.

The Ginzburg-Landau parameter

The GL parameter κ is the ratio of the two characteristic length scales. This ratio defines the type of superconductor as shown in figure 7 [17]:

$$\kappa = \frac{\lambda(T)}{\xi(T)}$$

$$\text{Type I} \qquad \kappa = \frac{\lambda}{\xi} < \frac{1}{\sqrt{2}},$$

$$\text{Type II} \qquad \kappa = \frac{\lambda}{\xi} > \frac{1}{\sqrt{2}},$$

where λ is the penetration depth, and ξ is the coherence length.

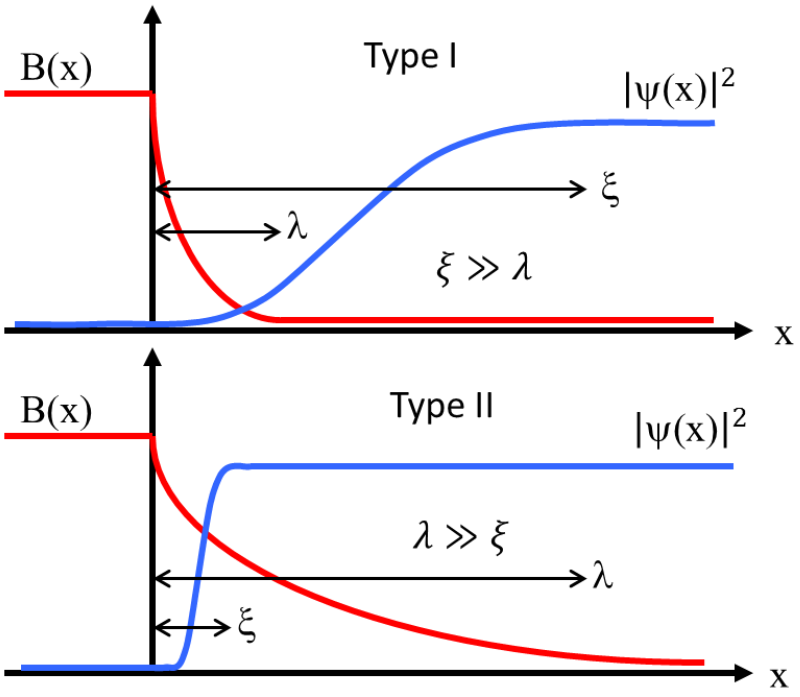

Figure 7: Illustration of an N/S interface in a type-I and a type-II superconductor.

2.3.3. Bardeen Cooper Schrieffer theory (BCS)

Although the Ginzburg-Landau theory provides an explanation for the electromagnetic properties of superconductors in high fields, it cannot explain the microscopic mechanism of superconductivity, e.g. the isotope effect, where the critical temperature is altered by incorporating different isotopes of the same elements. The discovery of the isotope effect suggested that superconductivity was in some way related to an interaction between the electrons and the crystal lattice. This feature of superconductivity was explained by a microscopic theory which was formulated in 1957 by Bardeen, Cooper and Schrieffer [7]. They proposed that a electron-phonon interaction could explain the absence of electrical resistivity in the superconducting state.

Cooper pairs

In BCS theory, the electrons form pairs near the Fermi surface due to the electron-phonon interaction. These bound electron pairs became known as Cooper pairs and only a very weak interaction was required to bind the electrons, this being provided by their interaction with the crystal lattice. This concept was first proposed by Frohlich in 1950 [18] and the physical idea of how Cooper pairs travel through the crystal is shown in figure 8. When the first electron travels through the lattice, it is attracted to nearby positive ions creating a local polarisation in the system. The second electron is in turn attracted by the positive region created by the first electron. In this way, Cooper pairs are formed whereby both electrons are indirectly bound together.

Cooper pairs can form when the attraction between the electron pair is greater than the Coulomb repulsion between them. The coherence length, ξ, represents the typical size of a Cooper pair, which can be up to a few μm in some conventional superconductors like Al.

The binding energy of Cooper pairs will be maximum when they have opposite momenta $(k, -k)$, and minimum exchange correlation energy when they have opposite spins ($k\uparrow$, $k\downarrow$). Thus, the ground state of Cooper pairs in the superconducting state has zero angular momentum, the pairing in this state is known as the singlet state (S=0).

The ground state BCS wavefunction for a Cooper pair is given as;

$$|\psi_{BCS}\rangle = \prod_k \left(u_k^* + v_k^* c_{k\uparrow}^\dagger c_{-k\downarrow}^\dagger\right)|0\rangle, \tag{2.18}$$

where u_k^*, v_k^* are complex cofficients where $|u_k|^2 + |v_k|^2 = 1$, $|0\rangle$ is the empty (vacuum) state, and $c_{k\uparrow}^\dagger c_{-k\downarrow}^\dagger$ is the electron operator for electron pairs with opposite spin. The occupied probability of the Cooper pair *($k\uparrow$, $-k\downarrow$)* is $|v_k|^2$, and the unoccupied probability is $|u_k|^2 = 1 - |v_k|^2$.

The Hamiltonian for an ensemble of Cooper pairs is

$$H = \sum_{k,\sigma=\uparrow,\downarrow} \left(\frac{\hbar^2 k}{2m} - \mu\right) c^{\dagger}_{k\sigma} c^{\dagger}_{-k\sigma} + \frac{1}{2}\sum_{k,k'} c^{\dagger}_{k\uparrow} c^{\dagger}_{-k\downarrow} V_{k,k'} c^{\dagger}_{k'\uparrow} c^{\dagger}_{-k'\downarrow}, \qquad (2.19)$$

where μ is the chemical potential, the term $\varepsilon_k = \left(\frac{\hbar^2 k}{2m} - \mu\right)$ represents the band energy dispersion and $V_{k,k'}$ is an attractive interaction. The ground state can calculated by minimization of the expectation value of H.

$$\frac{d}{du_k}\langle\psi_{BCS}|\sum_{k,\sigma=\uparrow,\downarrow}\left(\frac{\hbar^2 k}{2m} - \mu\right) c^{\dagger}_{k\sigma} c^{\dagger}_{-k\sigma} + \frac{1}{2}\sum_{k,k'} c^{\dagger}_{k\uparrow} c^{\dagger}_{-k\downarrow} V_{k,k'} c^{\dagger}_{k'\uparrow} c^{\dagger}_{-k'\downarrow} |\psi_{BCS}\rangle = 0 \qquad (2.20)$$

The expression for the excitation energy of quasiparticles in a superconductor is given by

$$E_k = \sqrt{\left(\frac{\hbar^2 k}{2m} - \mu\right)^2 + \Delta^2} = \sqrt{\varepsilon_k{}^2 + \Delta^2} \qquad (2.21)$$

where the Δ is the energy gap in the excitation energy spectrum, as shown in figure 9. The energy gap decreases with increasing the temperature up to T_c,.

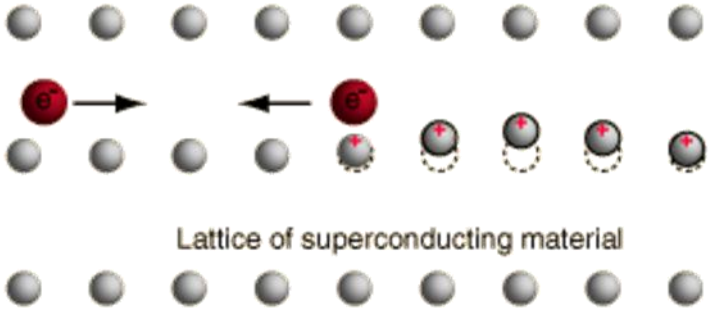

Figure 8: The formation of a bound Cooper pair via the electron-lattice interaction.

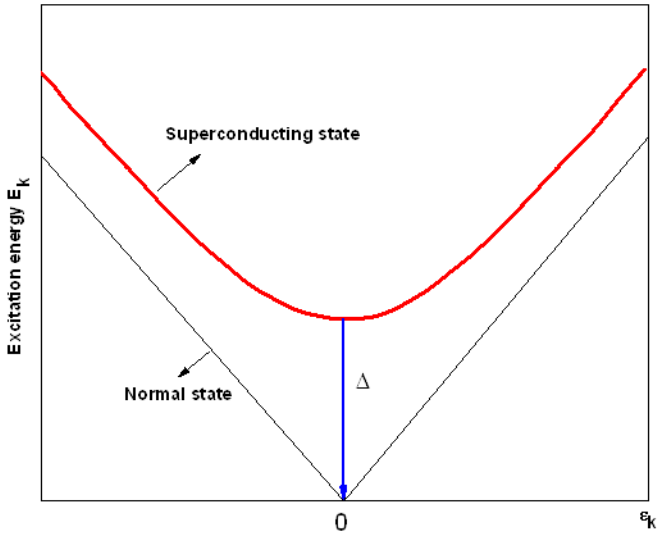

Figure 9: Diagram of the quasiparticle excitation spectrum.

Energy Gap

According to BCS theory, the Cooper pairs are formed by electrons with opposite spins and wave vectors. The ground state of a pair is separated from the excited states by an energy gap, 2Δ. This is twice the binding energy of a Cooper pair (the energy required to break the paired state by thermal fluctuations). The magnitude of the gap at zero temperature, $\Delta(0)$, is related to the superconducting transition temperature T_c, by [19]

$$2\Delta(0) = 3.528 k_B T_c, \tag{2.22}$$

where k_B is the Boltzmann constant. The temperature dependence of the BCS energy gap reveals that Δ(T) falls to zero at T_c, as shown in figure 10. Additionally the temperature dependence of the energy gap near the critical temperature is given approximately by the formula [20]

$$\frac{\Delta(T)}{\Delta(0)} \approx 1.74\sqrt{1-(T/T_c)} \tag{2.23}$$

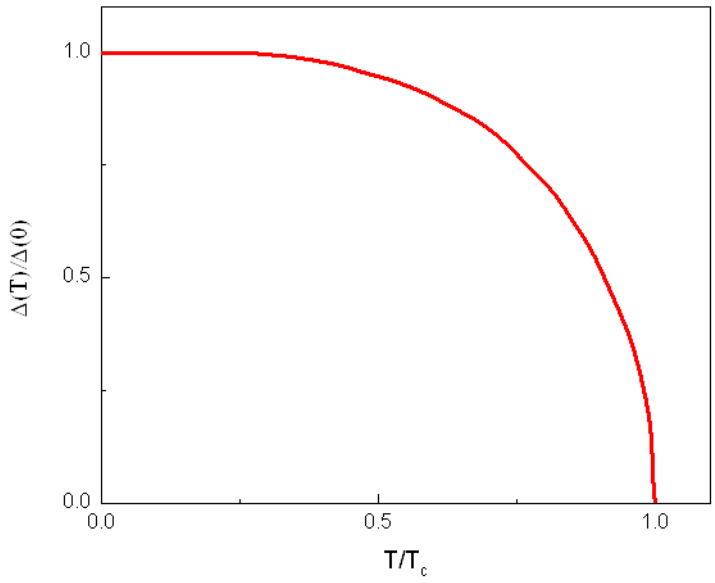

Figure 10: The normalized BCS gap function $\Delta(T)/\Delta(0)$ as a function of temperature [20].

2.4. Multiband Superconductivity

According to the postulates of BCS theory, all electrons on an isotropic Fermi surface (FS) contribute equally to the superconducting pairing, yielding a constant superconducting gap, Δ. However, different states can occur when the FS has multiple bands and the electrons from these contribute to the superconductivity of a anisotropic material. That is, the electrons on different FS bands have different electron-phonon coupling strengths leading to different superconducting energy gaps, leading to what is now known as multiband superconductivity [21].

The behaviour of multiple band superconductors is divided into three groups according to the coupling strengths, which depend upon their relative compatibility with pair exchange. The first is weak interband coupling, where the superconducting bands behave almost independently and have separate critical temperatures as shown in figure 11 (a). The second, intermediate interband coupling, is illustrated in figure 11 (b),

whilst the third is strong coupling, where the weaker band fully adopts the T_c of the stronger band as shown in figure 11 (c).

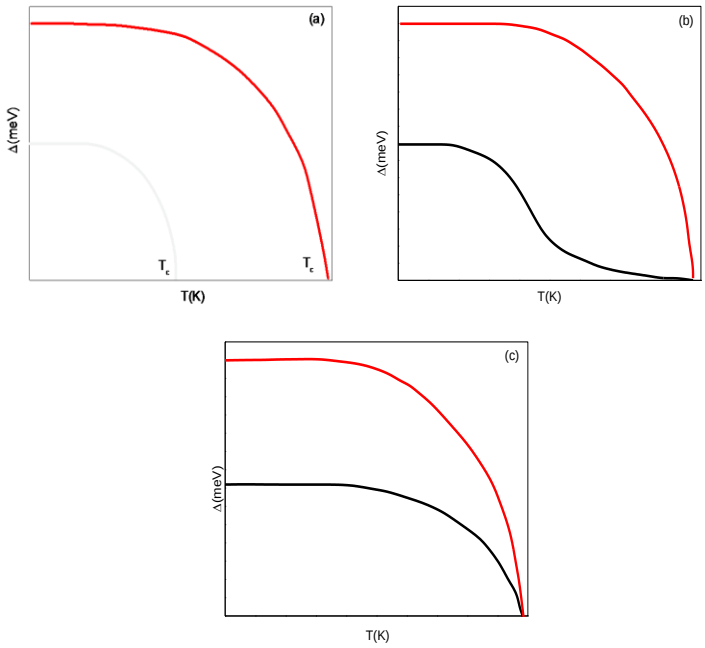

Figure 11: The red and black lines show the larger and the smaller gap bands, respectively, for (a) weak, (b) intermediate, (c) relatively strong coupling multi-band superconductors [21-24].

The superconducting gap is a very important quantity in superconductors as it is closely related to the Cooper pair state and the superconducting order parameter. Consequently energy gap measurements provide information about the pairing symmetry [25]. Figure 12 (a) represents the fully gapped isotropic s-wave gap as described by the original BCS theory with L = 0 and S = 0 [26, 27]. figure 12 (b) represents the anisotropic d-wave gap with L = 2 and S = 0, whilst figure 12 (c) represents the anisotropic p-wave gap with L = 1 and S = 1 [28].

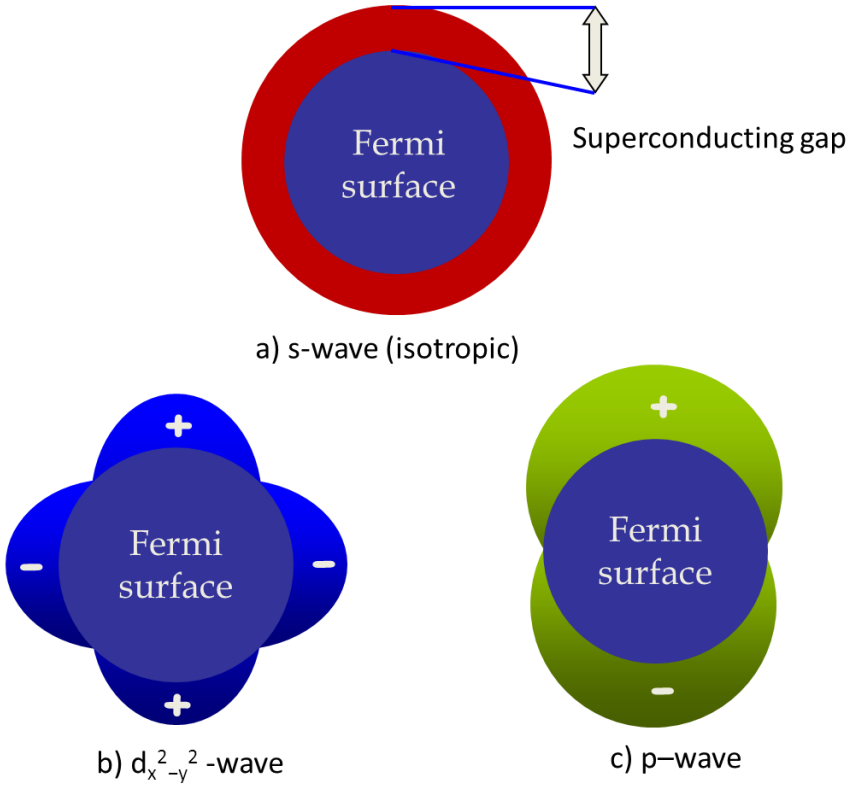

Figure 12: Spherical Fermi surfaces with different order parameter gaps in momentum space [26-28].

Behaviour of the penetration depth and superfluid density for different superconducting pairing symmetries

The magnetic penetration depth, λ, is one of the two essential length scales in superconductors [17] and its behaviour is determined by the number of electrons in the superconducting state (the superfluid density). Precise measurements of the penetration depth and its temperature variation $\Delta\lambda(T) = \lambda(T) - \lambda(0)$ are necessary to characterise the superconducting state, such as the gap structure [29, 30] and the superconducting pairing symmetry. The temperature dependence of λ can be determined from measurements of the temperature dependencies of the specific heat and lower critical field. One common form known as the two-fluid temperature dependence, is given by [30]:

$$\lambda(T) = \frac{\lambda(0)}{\sqrt{1-(T/T_c)^4}}\,, \tag{2.24}$$

In the case of a single s-wave superconducting gap where the effect of impurity scattering is very small (clean limit), the temperature dependence of the penetration depth can be calculated as a function of the penetration depth and energy gap at zero temperature using BCS theory [31], which yields the following dependence up to a value of $\sim \mathrm{T_c}/3$

$$\Delta\lambda(T) \approx \lambda(0)\sqrt{\frac{\pi\Delta(0)}{2k_BT}}exp - \left(\frac{\Delta(0)}{k_BT}\right). \tag{2.25}$$

From equation 2.25, it can be seen that the penetration depth saturates exponentially at very low temperatures. Any small deviation from the ideal behaviour indicates that there are additional quasiparticles at low temperatures due to pair-breaking scattering or nodes in the superconducting gap.

In the case of multigap superconductors such as MgB_2, the penetration depth and its temperature dependence correspond to the single gap case up to a temperature $(T_c/3)(\Delta_{min}/\Delta_{max})$, where Δ_{max} and Δ_{min} are the magnitudes of the largest and smallest gaps respectively. In cuprate superconductors, where the order parameter symmetry is d–wave, it is proposed that superconductivity is mediated by mechanisms other than electron-phonon coupling and the temperature dependence of $\Delta\lambda(\mathrm{T})$ in the clean limit is linear at low temperature, as given by

$$\Delta\lambda(T) \approx \frac{\lambda(0)2ln2k_B}{\alpha\Delta(0)}T. \tag{2.26}$$

The linear temperature dependence of $\lambda(T)$ was first observed by Hardy *et al.* [29] in a BSCCO single crystal, heralding the ability to measure the

temperature dependence of the penetration depth precisely in many different superconductors.

The normalized superfluid density, $\bar{\rho}_s(T)$, is the ratio of the number of superconducting electrons and the total number of charge carriers and is related to the penetration depth via London theory by:

$$\bar{\rho_s}(T) = \frac{n_s(T)}{n_{total}} = \frac{\lambda^2(0)}{\lambda^2(T)} = \left[1 - \frac{\Delta\lambda(T)}{\lambda(0)}\right]^{-2}. \quad (2.27)$$

According to BCS theory for a three dimensional single isotropic gap, the superfluid density in the clean limit can be calculated by substituting equation 2.25 into equation 2.27, giving

$$\bar{\rho_s}(T) = \left[1 - \frac{\Delta\lambda(T)}{\lambda(0)}\right]^{-2} = 1 - \sqrt{\frac{2\pi\Delta(0)}{k_B T}}\, exp - \left(\frac{\Delta(0)}{k_B T}\right). \quad (2.28)$$

It can also be derived in terms of the superconducting gap for a two-dimensional cylindrical Fermi surface with isotropic s-wave pairing:

$$\bar{\rho_s}(T) = 1 - \frac{1}{2kT}\int_0^\infty cosh^{-2}\left(\frac{\sqrt{\varepsilon^2+\Delta^2(T))}}{2kT}\right) d\varepsilon. \quad (2.29)$$

Equation 2.28 is plotted in figure 13 as a black solid line, representing the normalised superfluid density for a single gap s-wave superconductor in the clean limit. It can be seen that the exponential dependence leads to saturation (as shown by the flat line) at low temperatures (below roughly $T_c/3$).

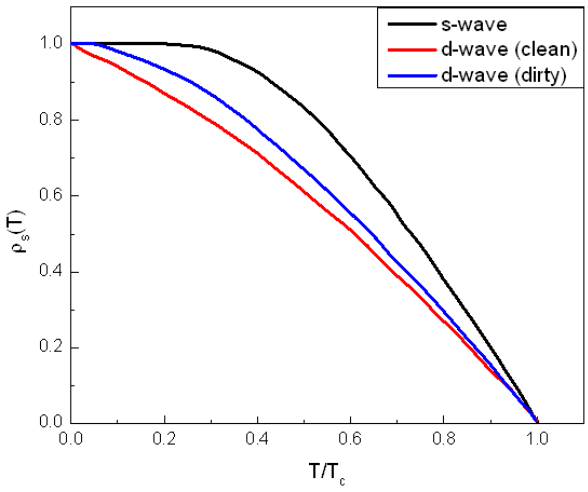

Figure 13: Theoretical curves for the normalised superfluid density and its temperature dependence for the: clean s-wave, clean d-wave and dirty d-wave impurity scattering limits[32].

In the case of d–wave pairing in the high-T_c cuprate superconductors with vertical line nodes in its gap function [33], the normalised superfluid density is given by:

$$\bar{\rho_s}(T) \approx 1 - \frac{2ln2k_B}{\Delta(0)}T \ . \qquad (2.30)$$

The orange solid line in figure 13 illustrates the normalised superfluid density for a clean limit d–wave superconductor, while the blue line in the same figure represents the normalised superfluid density for a dirty limit d–wave superconductor [33].

Finally, the penetration depth and the normalised superfluid density and its temperature dependence represent valuable information about the structure of the gap in a superconductor and $\bar{\rho_s}(T)$ can demonstrate effects associated with multigap superconductivity or anisotropy of the superconducting gap over the entire temperature range up to T_c.

Multigap superconductivity and superfluid density

Many superconductors discovered in recent years are multiband materials with complex Fermi surfaces, for example MgB_2 and the iron-pnictides. These materials may be approximately described by an α-model that was developed to take into account multiple gaps and the associated scattering processes and has been widely used to fit specific heat and penetration depth data [34]. The α-model applies the BCS temperature dependence to both gaps $\Delta_{1,2}$. In order to calculate the total superfluid density $\bar{\rho_s} = x\bar{\rho}_1 + (1-x)\bar{\rho}_2$, where $\Delta_{1,2}$ are evaluated using the following equation, then inserted into equation 2.29 [35].

$$\Delta_{1,2} = \Delta_{1,2}(0)\, tanh\left[\frac{\pi k_B T_c}{\Delta_{1,2}(0)}\sqrt{a_{1,2}\left(\frac{T_c}{T}-1\right)}\right]. \qquad (2.31)$$

x is the fractional contribution from both bands and a is a parameter dependent upon the particular pairing state (related to the size of the jump in a specific heat at T_c). The α-model has played an important role in providing convincing evidence for two-gap superconductivity in materials such as MgB_2 [36] and Co-doped SrFeAs [35].

2.5. Type I and Type II superconductors

Superconductors are divided into two categories depending upon their behaviour in the presence of a magnetic field [6]. The first category, known as Type I superconductors, comprises pure metals whilst the second category, known as Type II superconductors, is constituted from many families such as intermetallic compounds, copper-oxide and pnictide superconductors. Both categories have one common feature: the resistance vanishes below the critical temperature T_c.

Type I superconductors exhibit a classic Meissner state where the magnetic flux is completely expelled from the superconductor up to the critical field, H_c. Above this value all the superconducting properties are destroyed as shown in figure 14(a,c). In type I materials the coherence

length is larger than the penetration depth, so it is not energetically favourable for additional boundaries to form between normal and superconducting phases.

Type II superconductors have two critical fields: the first is the lower critical field, H_{c1}, below which the magnetic flux is completely expelled (Meissner state). The second is the upper critical field, H_{c2}, above which the superconductor reverts to the normal state. Between the lower and upper critical fields $H_{c1} < H < H_{c2}$, the flux partially penetrates into the superconducting specimen (mixed state) as shown in figure 14(b,d). In type II superconductors the penetration depth is larger than the coherence length, and it becomes energetically favourable for additional walls to form between superconducting and normal regions.

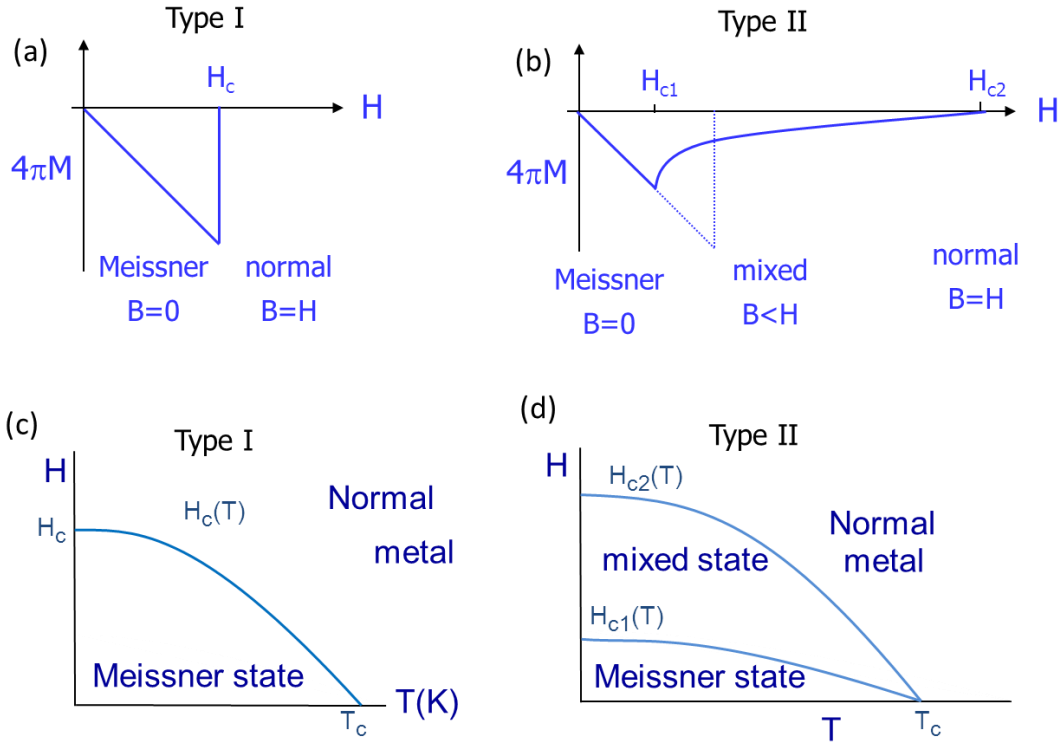

Figure 14: Magnetisation curves and (H-T) phase diagrams for type I and type II superconductor materials.

The Interfacial Energy

It is necessary to calculate the sign of the energy of the interface between normal and superconducting regions in order to identify a superconductor's class**.** This is determined by the two fundamental length scales of a superconductor. For the interface to be stable, the system must be in equilibrium, meaning that the free energy densities of the normal and superconducting phases must be equal as shown in following equation:

$$\frac{1}{2}\mu_0 H_c^2 = f_n - f_s, \tag{2.32}$$

where f_n , f_s are the free energy densities of the normal state and superconducting state respectively. It can be seen from equation 2.32, that decreasing the condensation energy in the material by an amount $f_n - f_s$ is equal to increasing the free energy density of the superconductor by an amount $\frac{1}{2}\mu_0 H_c^2$ due to the exclusion of the applied magnetic field. The order parameter ψ near the interface decreases from a maximum over a maximum distance ξ, and the free energy density therefore increases due to the consequent loss of the condensation energy over the same distance.

The volume of the superconducting region decreases by $\sim A\xi$, when the interface area is equal to A. This makes a positive contribution to the free energy at the interface given by $(f_n - f_s)A\xi$. On the other hand, a decrease in the magnetic energy occurs due to field penetration over the penetration depth, giving a negative energy contribution of approximately $-\frac{1}{2}\mu_0 H_c^2 A\lambda$. These two contributions are not equal and do not cancel because the values of λ and ξ are not equal, and interface energy per unit area is approximately given by:

$$\sigma \simeq \frac{1}{A}((f_n - f_s)A\xi - \frac{1}{2}\mu_0 H_c^2 A\lambda \simeq \frac{1}{2}\mu_0 H_c^2(\xi - \lambda). \tag{2.33}$$

The sign of a surface energy changes from negative to positive when ξ equals λ ($\kappa = 1$). A more accurate calculation using G-L theory illustrates that the change of sign of the surface energy occurs at $\kappa = 1$. Thus for $\kappa < \frac{1}{\sqrt{2}}$ the surface energy is positive and for $\kappa > \frac{1}{\sqrt{2}}$ the surface energy is negative.

2.6. Vortex state (Mixed state)

Above H_{c1} a type II superconductor enters the mixed state with coexisting normal and superconducting regions. The surface energy at the interface between the normal and superconducting regions is negative and the value of the applied magnetic field lies between H_{c1} and H_{c2}. The free energy of the superconductor can hence be minimised by introducing as much normal superconducting interface as possible.

In the mixed state (vortex state), there is partial flux penetration in the superconductor sample. The magnetic flux penetrates the superconductor in cylinders, each called a vortex and containing a single flux quantum, $\phi_0 = {}^{h}/_{2e} = 2.068 \times 10^{-15}$Wb, where h is Planck's constant and e is the electronic charge.

The vortex consists of a cylindrical normal core containing the magnetic flux enclosed by circulating superconducting currents as shown in figure15. The radius of the normal core of a vortex is approximately the coherence length, and the range of the magnetic fields is given approximately by λ. The values of the critical fields H_{c1} and H_{c2} can be calculated in terms of the flux quantum, according to the following equations

$$H_{c1} = \frac{\Phi_o}{4\pi\lambda^2} ln\left(\frac{\lambda}{\xi}\right), \tag{2.34}$$

and

$$H_{c2} = \frac{\Phi_o}{4\pi\xi^2}. \tag{2.35}$$

The penetration of vortices occurs once the applied field is increased beyond H_{c1}. In a perfectly ordered sample the vortices arrange themselves in a stable vortex lattice which should normally be triangular with the separation between vortices (lattice period) equalling $(2\phi_0/B\sqrt{3})^{1/2}$ as shown in figure16. Hence the vortex density increases with increased applied magnetic field. When the applied field reaches H_{c2}, the distance between neighbouring vortices is of the order of ξ, which means that the normal cores of the vortices are in contact with each other and the sample is no longer superconducting. The existence of the triangular vortex lattice was first experimentally observed in 1967 using the Bitter decoration technique [17]

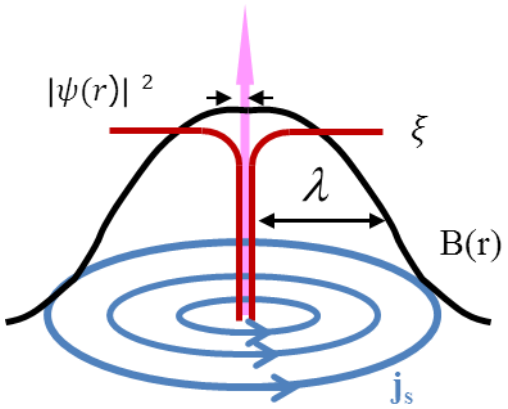

Figure 15: the magnetic induction, current density and order parameter in a vortex as a function of radius **r** from the vortex core.

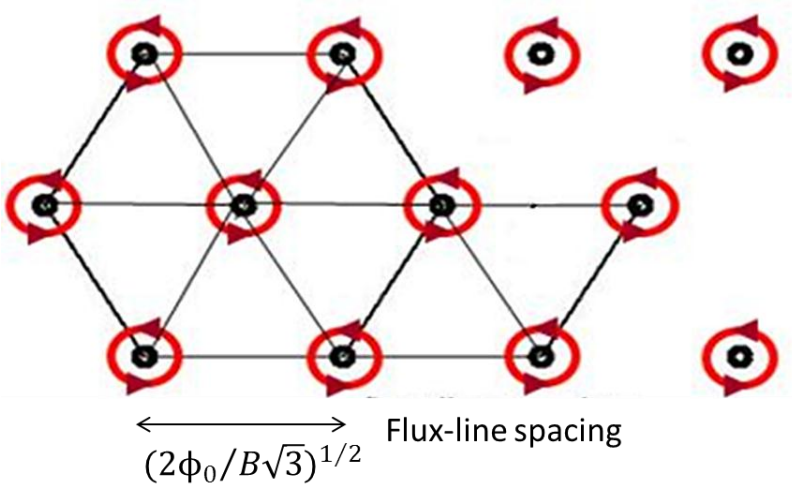

Figure 16: The ideal triangular vortex lattice with lattice period $(\mathbf{2\phi_0/B\sqrt{3}})^{\mathbf{1/2}}$.

Vortex-vortex interactions

In an ideal superconductor (i.e. one with very weak pinning), the vortices arrange themselves in a triangular lattice called the Abrikosov flux lattice. There is a repulsive interaction between vortices due to the circulating supercurrents around each normal core interacting with the magnetic field produced by supercurrents at other flux lines. This interaction can be described by the Lorentz force acting on the supercurrent of the first vortex in the magnetic field of the second giving a force per unit length of:

$$\vec{f} = \vec{j}(r) \times \overrightarrow{\phi_0}, \tag{2.36}$$

where j is the supercurrent density due to first vortex at the position of the second vortex and $\vec{\phi}_0$ is a vector of magnitude of the flux quantum directed along the length of the vortex. For the London model at large vortex separations ($r \gg \lambda$), the magnitude of the force per unit length is approximately given by [37]

$$f = \frac{\phi_0}{2\pi\mu_0\lambda^3}\sqrt{\frac{\pi\lambda}{2r}}exp(-r/\lambda)\ . \tag{2.37}$$

Vortex motion

The most beneficial feature of type-II superconductors is the potential ability to operate in high magnetic fields and carry high current without dissipation, although in reality there can be dissipation due to vortex motion[38]. The simplest geometry to consider occurs when an external magnetic field, H, is applied perpendicular to a current density, j, which is passing through the plane of a superconducting sample. Hence the applied current flows through the vortex cores generating a Lorentz force on the vortex per unit length of:

$$\overrightarrow{F_L} = \vec{j} \times \overrightarrow{\phi_0}, \tag{2.38}$$

where j is the current density (assumed to be uniform) and $\vec{\phi}_0$ is a vector of magnitude of the flux quantum directed along the magnetic field. The resulting flux line motion is perpendicular to the current flow, inducing an electric field perpendicular to the vortex motion and the field direction.

$$\vec{E} = \vec{B} \times \overrightarrow{v_L}, \tag{2.39}$$

where v_L is the drift velocity. When the vortices move they dissipate energy and cause electrical resistance by the appearance of a voltage drop along the sample. Figure 17 shows the directions of the current density, magnetic field and vortex motion.

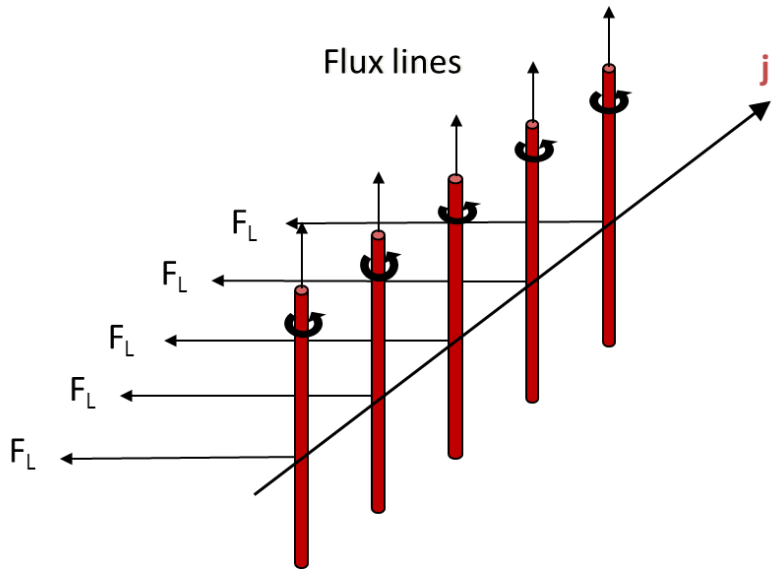

Figure 17: Schematic representation of Lorentz force driven vortex motion.

Flux Pinning

In addition to the Lorentz force, F_L, that causes vortex motion, there is also a mechanism which prevents vortices from moving. This is known as a 'pinning' force because it pins vortices at a fixed location in the

superconductor. In practice, the pinning mechanism results from the spatial inhomogeneity of real materials, such as defects in the crystalline structure, grain boundaries, impurities and voids [17].

The effect of a pinning centre can be understood by considering the free energy associated with the vortex core. The impurities, grain boundary voids etc., cause local variations of the free energy per unit length of a flux line, ε_1, which causes some locations of the vortex to be favoured over others resulting in the flux tubes trying to locate in positions that minimise the total energy, subject to the additional repulsive interaction between vortices.

The material acts like a 'perfect' superconductor when the dissipation is at a minimum due to the pinning force being strong compared to the driving force, when vortex motion is negligible. In practice, thermal excitations can activate 'flux creep' whereby vortices hop from one pinning site to another. When the pinning force is weak compared to the driving force, the vortices can move in a relatively steady motion with their velocities limited by the viscous drag, η and the viscosus force equal to ηv_L. For the simplest geometry, the force balance equation is, $\Phi_0 J = \eta v_L$ and the flux flow resistivity, ρ_f, is defined by $E = j\rho_f$. In any useful superconductor application, flux flow must be avoided and flux creep should be kept to a minimum level [39].

2.7. High temperature superconductors

High temperature superconductors (HTSCs) are a relatively recently discovered family of materials based on copper-oxide planes with a critical temperature up to 130K [40]. An HTSC is generally, a layered structure with tetragonal symmetry, containing CuO_2 conducting layers, which are separated by blocking layers of other atoms, such as Bi, O, Y, Ba, La as shown in figure 18. The charge carriers are transferred from the blocking layer into the CuO_2 planes. The parent compound of cuprates is an antiferromagnetic Mott insulator [41, 42] but doping of the CuO_2 planes leads

to superconductivity. The layered structure of the cuprates also makes them highly anisotropic materials, which vary from strong anisotropy in $YBa_2Cu_3O_7$ (YBCO) to extremely strong anisotropy in $Bi_2Sr_2CaCu_2O_8$ (BSCCO) [43]. That is, the physical properties are very different along different crystal directions.

In a conventional superconductor, the symmetry of the superconducting order parameter or energy gap $|\Delta(k)|$ is s-wave. In contrast, the pairing symmetry of HTSCs is d-wave ($d_{x^2-y^2}$) as indicated by very sensitive experiments probing the energy gap such as Raman scattering [44, 45], Josephson tunnelling and dc-SQUID measurements [46], NMR relaxation experiments [47], angle resolved photo emission spectroscopy (ARPES) [48], and thermal conductivity [49]. Unlike conventional superconductors, there is still no satisfactory theoretical explanation for the microscopic binding mechanism in these materials. However it is almost certain that Cooper pair involves formation a different mechanism from the electron-phonon interaction found in conventional low temperature materials.

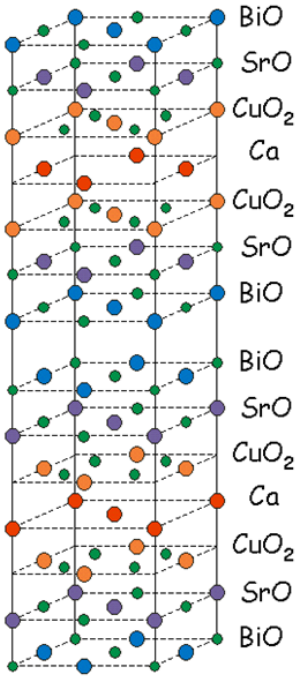

Figure 18: The unit cell of $Bi_2Sr_2CaCu_2O_8$ [50]

The vortex properties of cuprate superconductors can be quite different from those in traditional type-II materials due to the strong anisotropy of the layered structure and the weak interactions between the copper oxide planes.

At small out-of-plane fields (c-axis), pancake vortices are generated confined to the CuO_2 planes and only weakly coupled to their neighbours in adjacent planes. However, in a field parallel to the a-b plane, vortices form between the superconducting planes, known as Josephson vortices [51]. The associated current distributions are highly elliptical, and there is no normal core as the order parameter is already suppressed in the central blocking layer. In tilted fields the vortex can be described as a combination of pancake vortices in the c-direction connected by Josephson vortices in the a-b plane as shown in figure 19 [51].

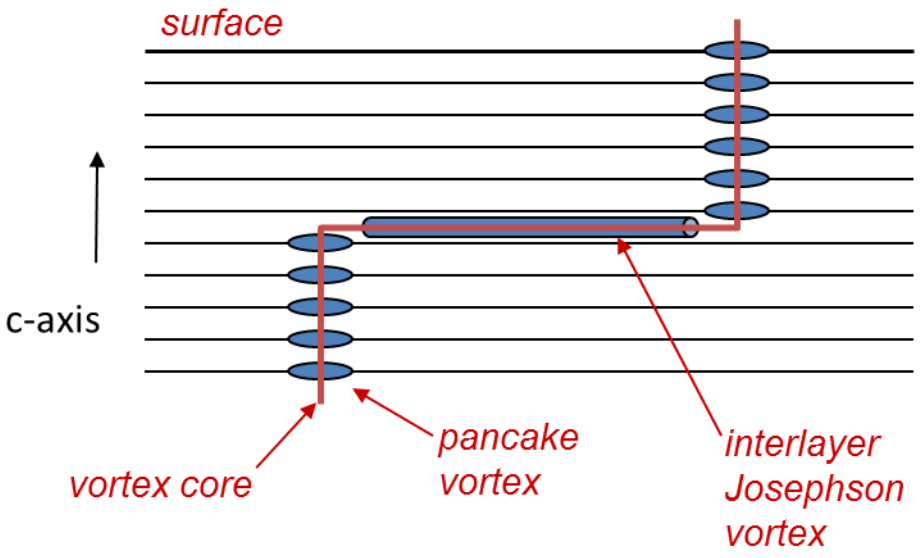

Figure 19: A flux vortex in a tilted field in an anisotropic HTSC [51].

2.8. Iron-based Superconductors

2.8.1. Introduction

Since the discovery of copper oxide (cuprate) high temperature superconductors (HTSCs) in 1986 [8] there have been extensive efforts to find new related superconductors, for example in two-dimensional (2D) transition metal oxides (TMO), borides and nitrides. Promising developments in this area include Li_xNbO_2 [52], Sr_2RuO_4 [53], Na_xCoO_2 [54], and Cu_xTiSe_2 [55], but all have superconducting critical temperatures below 5K. The most striking discoveries are the electron-doped hafnium nitride semiconductor (HfNCl) [56] with T_c = 25K and MgB_2 with T_c=39 K [10].

The superconductivity community has been reinvigorated by the discovery of a new class of layered transition metal pnictides, ROTPn, where R is a trivalent rare earth ion, T is a transition metal ion, O is oxygen, and Pn is a pnictogen atom. A breakthrough with T_c=26K was first reported for electron doped $LaO_{1-x}F_xFeAs$ [11], which was followed by hole-doped $La_{1-x}Sr_xOFeAs$ [57], with a similar value of T_c. The highest values of T_c (41-55K) were achieved by replacing La by Ce,[58] Nd [59] and Sm [12].

The family of iron-based superconductors has been rapidly extended, and can now be divided into five groups; RFeAsO and MFeAsF (1111-type), $M_2Fe_2As_2$ (122-type), Cu_2Sb-type AFeAs (111-type), FeTe and FeSe (11-type) and $Fe_2As_2Sr_4X_2O_6$ (22426-type) where R=rare earth metal; M_1=Sr or Ca, M_2=Ba, Sr, Ca or Eu; A=Li or Na; X= Sc, Cr [58, 60-65].

2.8.2. The lattice structure and physical properties of different families

Iron-pnictide compounds have tetragonal symmetry with no magnetic order at room temperature. Moreover the crystal structure of all such pnictides shares a common two-dimensional FePn layer, where Fe atoms

form a 2D square sub-lattice with Pn atoms sitting at the centre of this square, but outside the Fe plane (above and below the plane alternately). The FePn layer is different from the CuO layer in cuprates where the Cu and O atoms are in the same plane. The parent compounds of these iron-pnictides are metallic, while the parent compounds of cuprates are Mott insulators. At temperature, T_S, in the range 100-210K, Fe-pnictides undergo a structural transition from tetragonal to orthorhombic, and a magnetic transition T_N from non-magnetic to stripe antiferromagnetic or spin density wave (SDW) [66-69]. The structural and magnetic transitions can happen simultaneously or one after another, depending on the compound. It has been confirmed both experimentally and theoretically that the magnetic order of Fe at low temperature is stripe-like antiferromagnetism often referred to as a spin density wave (SDW)[66-69]. Upon doping or under hydrostatic pressure, the magnetic order is suppressed and the materials become superconducting.

1111 Structure

Early in 2006 superconductivity was found in LaFePO with a transition temperature T_c=5 K by Hosono's group [70]. Around the same time, various families of transition-metal oxide were discovered to be superconducting with similar low transition temperatures. In contrast, the known copper-oxide high-T_c superconductors show superconductivity far above 30 K. For this reason this discovery by Hosono's group [70] did not attract much attention in the scientific community.

However, in January 2008 the superconductivity community was surprised by another breakthrough of Hosono's group when they reported that T_c=26 K in the closely related system $LaFeAsO_{1-x}F_x$ [11, 70]. Many related superconducting compounds were subsequently discovered belonging to the 1111-family with the general formula $LFePnO_{1-x}F_x$ (Pn = P, As; L = La, Ce, Pr, Nd, Sm, Gd and Dy) [11, 12, 58, 71, 72]. Several of these systems were known to exist a long time before the discovery of superconductivity in the iron-pnictides. The undoped parent compound LFeAsO (L1111) has a

tetragonal layered ZrCuSiAs crystal structure, which consists of iron-pnictide (Fe_2As_2) layers containing the carriers, which are sandwiched between lanthanide oxide (L_2O_2) sheets acting as charge reservoirs when doped [11]. The unit cell consists of two molecules with chemical formula $(RO)_2$ $(FeAs)_2$. The $(FeAs)_2$ layer, which is sandwiched between the $(RO)_2$ layers, serves as a path for charge carrier conduction and the interlayer chemical bonding is covalent. Undoped L1111 is not superconducting and shows an antiferromagnetic transition at 150 K. Superconductivity is induced by doping the lanthanide oxide layers, either by partially replacing oxygen by another element [11], by creating oxygen deficiency [12, 73] or by applying pressure [74]. It has been shown that both electron doping (partially replacing L by Th [65]) and hole doping (partially replacing L by Sr [57]) in L1111 may also lead to superconductivity (see figure 20).

122 Structure

More recently, the discovery of superconductivity at 38 K in $Ba_{1-x}K_xFe_2As_2$ with $ThCr_2Si_2$ structure was reported [62] (see figure 20). Subsequently, superconductivity was found in various related compounds (forming the 122-family of iron-pnictides) including hole doped $Sr_{1-x}K_xFe_2As_2$ and $Sr_{1-x}Cs_xFe_2As_2$ [63], $Ba_{1-x}K_xFe_2As_2$ [62], as well as electron-doped $BaFe_{2-x}Co_xAs_2$[75], $SrFe_{2-x}Co_xAs_2$ [76], and $BaFe_{2-x}Ni_xAs_2$ [77]. In addition, pressure-induced superconductivity was discovered in the parent compounds $CaFe_2As_2$[64], $SrFe_2As_2$ [78, 79], and $BaFe_2As_2$ [78]. Like the 1111 family of superconductors, several of these materials had been previously synthesized by Jeitschko *et al.* [80]. The $M_2Fe_2As_2$ compounds (M122) have a simpler crystal structure in which (Fe_2As_2) layers, identical to those in L1111, are separated by single layers containing elements like Sr, Ca, Ba, or Eu. In the MFe_2As_2 (M=Ba, Sr, Ca, Eu) compounds, $T_N=T_S$, i.e., the structural and magnetic transitions happen simultaneously. Whether the magnetic transition is induced by the structural transition and the nature of the driving force for the structural transition are two important questions

that are crucial to understanding the formation of stripe antiferromagnetic order in the parent compounds.

111 and 11 structure

The 111 family includes many members, such as LiFeAs and NaFeAs which belong to the 111 structure superconductors [81]. These have been found to crystallize in the PbFCl crystal structure and the FeAs layers are separated by Li or Na ions. In contrast to the previous two pnictide families, the transport properties of the LiFeAs materials do not reveal any anomalous behaviour due to magnetic and structural phase transitions. Also, without doping this compound shows a superconducting phase transition below a temperature of T_c = 18K [82, 83], while NaFeAs exhibits a structural transition from a high temperature tetragonal phase to a low temperature orthorhombic phase at T_N = 50K [84].

The 11-structure superconductors are Fe-chalcogenides (FeCh), such as FeTe, FeSe, and FeS. The crystal structure of these compounds is PbO type, which is the simplest of all the Fe-based families. Similar to the other Fe-pnictide families, the unit cell consists of $FeCh_4$ tetrahedra and two FeCh layers are present per unit cell as shown in figure 20[85].

In the case of FeCh compounds, the structural and magnetic transitions happen simultaneously, $T_{N(S)}$ = 70K, which means that at $T_{N(S)}$, the FeCh compounds undergo a transition from a paramagnetic tetragonal phase to an antiferromagnetic orthorhombic or monoclinic phase. The FePn layers in the case of 1111, 122 and 111 prototype compounds are separated by a block layer, while no separating layers are present in the 11-type superconductors. A superconducting transition temperature in a stoichiometric FeSe compound was observed at 8K [86] and the critical temperature was increased to 15K by replacing Se with Te [86, 87]. Moreover, under the application of hydrostatic pressure T_c increases dramatically [88].

Although iron-pnictide superconductors have quite different chemical compositions and structures, they tend to possess a number of common properties. For instance, they all have an extraordinarily high upper critical field, e.g. on the order of 100T in La1111 [35], which makes them very interesting for applications. In addition, the critical current density up to 10^9 A/m^2, is at least as high as for the cuprates [35].

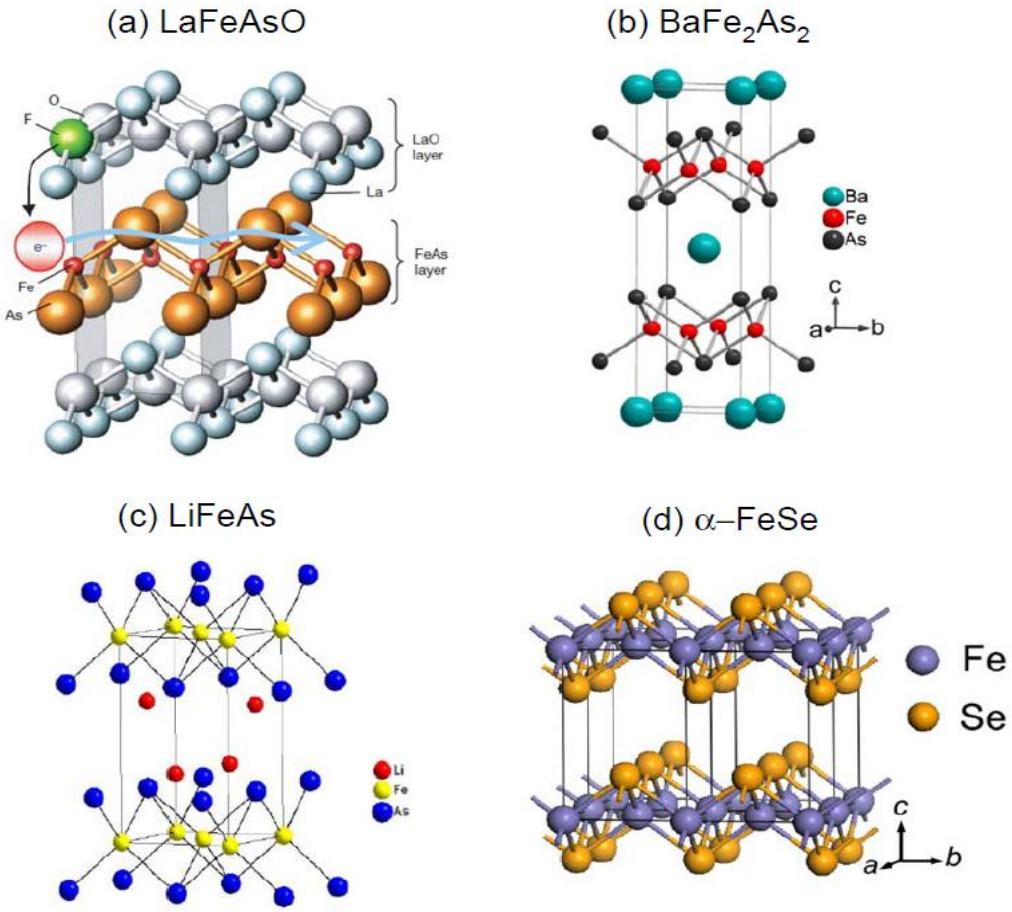

Figure 20: the crystal structures of (a) LaFeAsO [11], (b) $BaFe_2As_2$ [62], (c) LiFeAs [82] and (d) αFeSe [89].

2.8.3. Electronic structure and superconducting gaps

In contrast to cuprates which have one band that crosses the Fermi level and d-wave paring symmetry, the pnictides and MgB_2 have many bands at the Fermi surface, which opens up the possibility of multiband superconductivity. Indeed, MgB_2 was the first experimentally studied example of a multiband superconductor with two s-wave gaps.

After the pnictide superconductors were discovered, many results were published of calculations of the band structure and the density of state using density functional theory [26, 27, 90]. These investigations found that the iron-pnictide parent compounds are semimetallic and the density of states near the Fermi surface is principally composed of the Fe-3d electrons and all five of the As-3d electrons that cross this Fermi surface.

The electronic structure of pnictide materials is composed of two sets of disconnected sheets of Fermi surface, with at least two hole-pockets cantered at the Brillouin zone (Γ-point), and two electron-pockets sited at $(0;\pm\pi)$ and $(\pm\pi; 0)$ (M-points) in the tetragonal unit cell with one iron atom, as shown in figure 21 [90, 91].

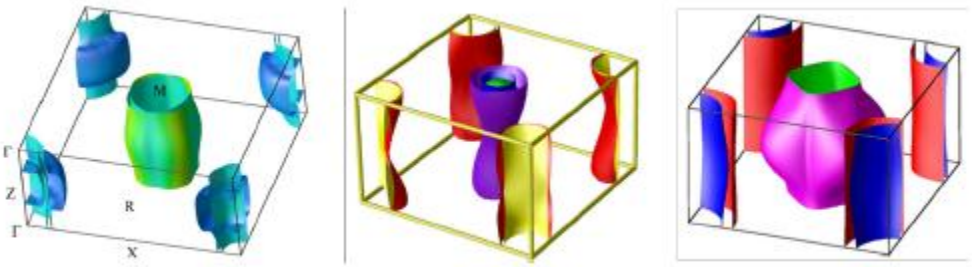

Figure 21: The Fermi surface calculated for the 1111 system (left) [90], 122 system (middle), and the 11 system (right) [91] respectively.

The nesting between the hole and electron pockets in $Ba(Fe_{1-x}Co_x)_2As_2$ has been observed by angle-resolved photoemission spectroscopy ARPES [92, 93] and quantum oscillations [94]. There also appear to be three-dimensional pockets in the complicated band structure of the materials,

which influence the physical properties and need to be taken into account to understand some experimental data.

2.8.4. Phase diagram

Phase diagrams are the most commonly employed way of describing the various properties of any superconductor, graphically revealing structural, magnetic and superconducting phase transitions. In additions to the physical properties, they also illustrate the different methods to induce superconductivity such as electron and hole doping and the application of pressure. Figure 22 illustrates the phase diagrams of three different Fe-based families. Most of these superconductors start from parent compounds with a spin density wave (SDW) order and the structural transition generally occurs almost simultaneously with the SDW transition on going from the high-temperature tetragonal phase to the orthorhombic phase at a low temperatures. Although the antiferomagnetic and superconducting phases generally exclude each other they can co-exist in the 122 structure.

Figure 22 shows phase diagrams of three examples drawn from different pnictide families: (a) shows the effect of doping in the 1111 family which includes F-doped LaOFeAs [95], (b) illustrates electron doping (Co substitution) in the 122 $BaFe_2As_2$ system and (c) electron doping in the 11-system ($Fe_{1:03}Te$) with Se doping [96].

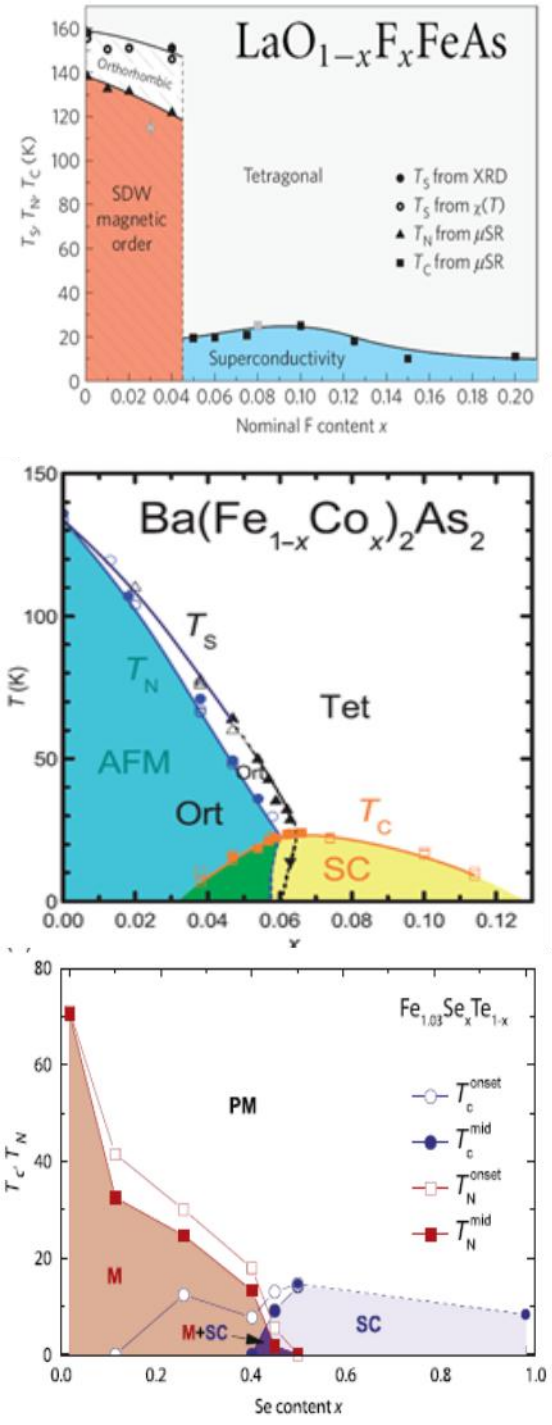

Figure 22: Typical phase diagrams of (a) the 1111 system, (b) the 122 system and (c) the 11 system.

2.8.5. Comparison between cuprates and Fe-Pnictide superconductors

The cuprates and iron-pnictides are the only two classes of materials, which have superconducting transition temperatures, T_c, above 50K. Both classes have a layered crystal structure yet, many differences exist between them, especially in their electronic structures [13]. The iron pnictides may be a multi-band system with s±wave paring, while the cuprates are a single band system with d-wave pairing symmetry. Both classes generally become superconducting after carrier doping of the antiferromagnetic parent compounds.

- Both pnictides and cuprates are type-II superconductors.
- The iron-pnictide parent antiferromagnetic state is metallic, while that in the cuprates is a Mott-insulator.
- In both classes, doping is a very important parameter for determining T_c; if the sample is doped very lightly or very heavily it does not superconduct at all.
- Both the cuprates and the iron pnictides are made of alternate layers of atoms, with the cuprates having CuO_2 sheets and the iron-pnictides having sheets of FeAs.
- Both pnictides and cuprates have varying degrees of anisotropy. The layered structure of the cuprates tends to make them strongly anisotropic materials, whereas the pnictides only have modest anisotropy.

2.9. Superconductivity and properties of MgB_2

2.9.1. Discovery of superconductivity in MgB_2

Magnesium diboride (MgB_2) is an inexpensive simple binary compound material. It was first synthesized in the 1950s, but was only recognised to be a superconducting compound in 2001 when Akimitsu's group published the crystallographic structure and the low temperature physical properties in Nature [10]. The bulk critical temperature of MgB_2 is 39K, which is higher than any other conventional superconductor [10]. This discovery excited a huge amount of scientific interest because the compound has unique and unusual properties. For example, the superconducting critical temperature of MgB_2 is nearly two time higher than any other known binary (intermetallic) compound and its upper critical field is much higher than the peak field of any magnets which are currently in use, e.g. Nb_3Sn solenoids. The weak-link problem in MgB_2 is much less serious than in cuprates and it can be made from relatively cheap materials. These properties suggest that MgB_2 may play a key role in applications in the near future [97]. Moreover this compound, unlike many other known high T_c superconductors, is very simple in composition and structure like other low temperature superconductors, yet was the first to clearly show multigap superconductivity phenomena. For all these reasons, the physical, chemical and electronic properties of MgB_2 remain of very strong interest to scientists to the present day.

2.9.2. Crystal structure of MgB_2

The most significant thing about MgB_2 is its high transition temperature combined with a very simple crystal structure, much like the Nb-based superconductors. This intermetallic compound has a hexagonal (AlB_2) lattice structure with lattice constants a = 0.3086 nm and c = 0.3524 nm. The crystal is composed from alternating Mg and B planes whereby the boron atoms form graphite-like honeycomb layers that are sandwiched between two magnesium layers located above the centres of the boron

hexagons, as show in figure 23. The B layers play an important role in the MgB_2 superconductors, similar to CuO_2 in cuprates and FeAs in pnictides.

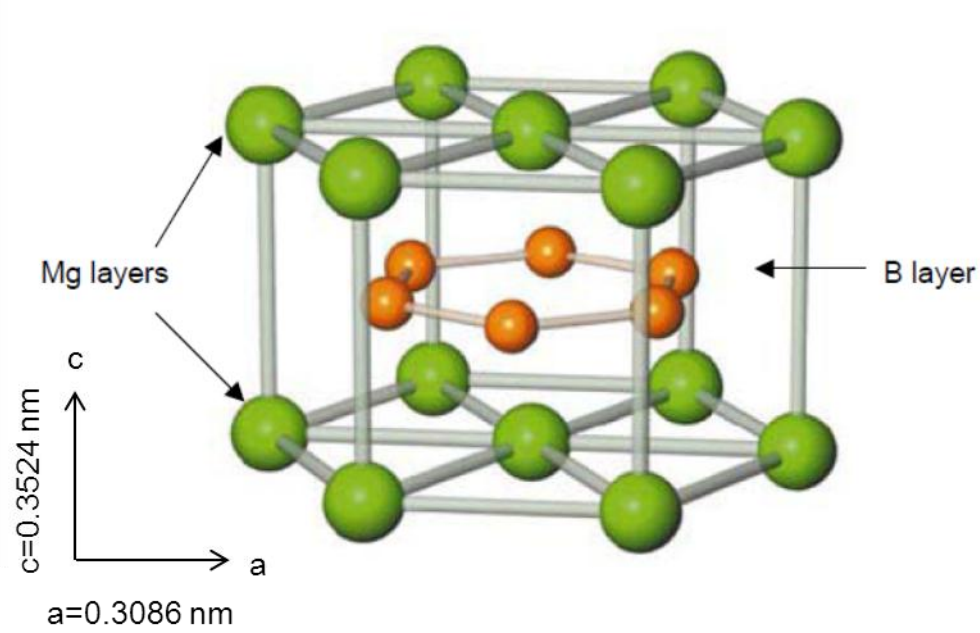

Figure 23: The hexagonal (AlB_2) crystal structure of MgB_2 [10].

The MgB_2 structure shows relatively strong anisotropy, due to the intra-layer B-B bond being shorter than the inter-layer distance and the strong intra-layer bonding combined with a weak inter-layer interaction.

Some of the properties of MgB_2 suggest that it behaves like conventional superconductors, such as the linear temperature dependence of H_{c2} [98] and the isotope effect [98, 99]. In contrast, other properties such as its penetration depth, λ, which varies quadratically with temperature as T_c is approached [100], suggest that it behaves in the same way as HTSC materials. Consequently, some researchers have suggested that it might be the first of a new type of superconductor [101].

2.9.3. Electronic structure

Calculations of the electronic band structure of MgB_2 reveal that the Mg atoms donate their 3*s* electrons to the B layer. Within every B layer, the

overlapping sp^6 orbitals form strong covalent σ-bonds and σ electrons are confined in the boron planes and only conduct in this plane. The p_z orbitals extend between the B layers to form π-bonds. These bonds connect the B planes across Mg ions and allow metallic conduction perpendicular to the B layers. The σ-bonding states are stronger than the π-bonding ones [36, 102]. Figure 24 shows the σ- and π-bonding states at the Fermi level originating from boron $p_{x,y}$ and p_z orbitals, respectively [102].

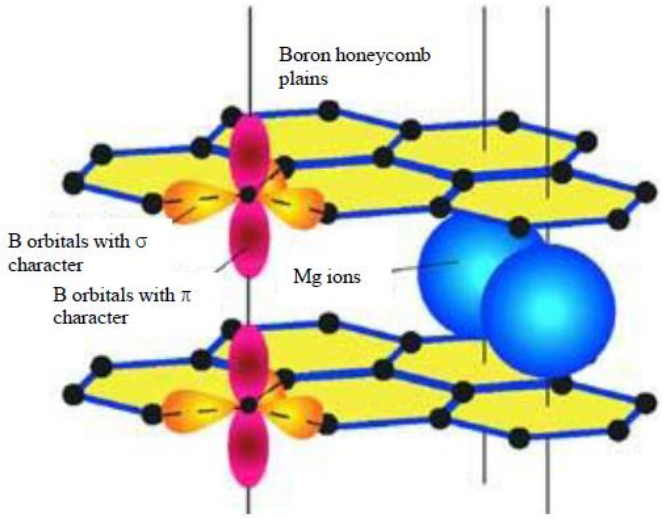

Figure 24: The orbital structure of MgB_2 [102].

The Fermi surface of MgB_2 was calculated long before it was discovered to be a superconducting compound, as shown in figure 25. It is characterised by four separate sheets [36], two of them resemble cylinders (coloured in blue and green), and are generated from the σ-bonding $p_{x,y}$ orbitals of boron and sited around the four Γ-A lines. The other two sheets (coloured in red and blue), which resemble webbed tunnels, are generated from the π-bonding p_z orbitals of boron and sited around K-M and H-L lines.

The smaller cylindrical σ sheets (green) have a superconducting energy gap of $\sim 7.2 \pm 0.1$ meV, while the wider cylindrical σ sheets (blue) have a superconducting energy gap which ranges from 6.4 to 6.8 meV. The π sheets (blue and red) have a gap in the range 1.2 to 3.7 meV. Figure 26

shows the superconducting energy gaps for the σ and π bonding states and their temperature dependencies up to the critical temperature [36].

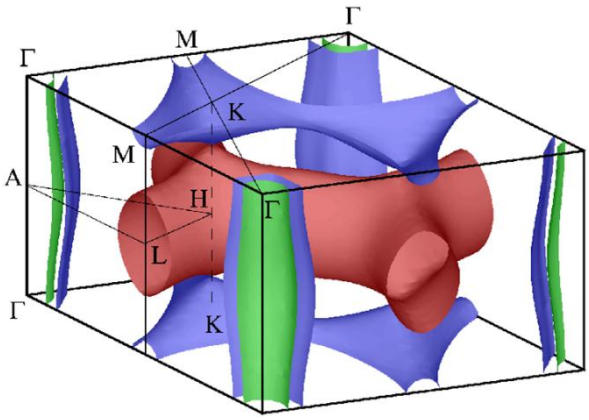

Figure 25: The Fermi surface of MgB_2 at 4K [36].

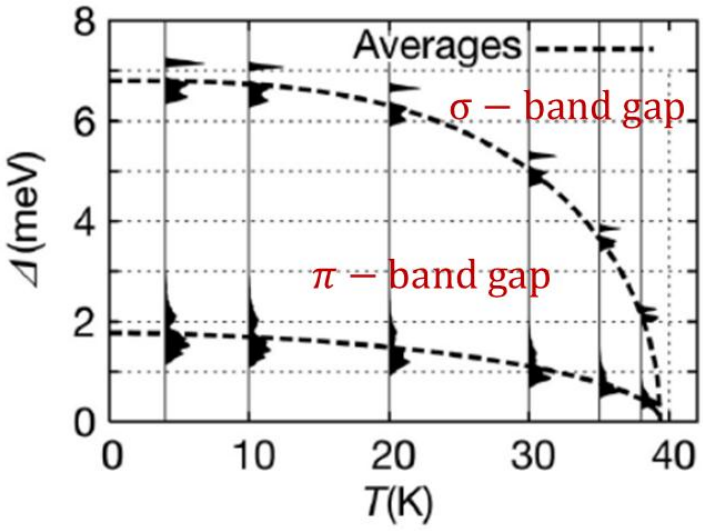

Figure 26: The temperature dependencies of the MgB_2 energy gaps [36].

2.9.4. Anisotropy of MgB_2

The anisotropy of superconductors is an important parameter in understanding its physical properties. The anisotropic properties of MgB_2 arise from their hexagonal crystal lattice structure, which consists of alternating Mg and B sheets. Hence it is natural to expect some properties

to depend on the direction in which electric currents or magnetic fields are applied.

Due to the anisotropic properties of this superconductor, H_{c2} is characterised by the anisotropy ratio $\gamma = H_{c2//ab}/H_{c2//c}$, where the value of γ ranges between 1.1 and 9 [103], and the values of $H_{c2//}$ at T= 0K ranges between 6-12 T for MgB_2 bulk wires, tapes and powders, giving considerable promise for applications. This anisotropy is also revealed in textured polycrystalline samples since all grains tends to exhibit common crystallographic orientation in these materials.

2.9.5. Advantages of two gap superconductivity

The possibility of two energy gaps was verified for the first time in MgB_2, and revealed as two distinct isotropic superconducting gaps with average values of around 2.8 meV and 7 meV, due to the π and σ bands respectively. This was confirmed by several different experimental techniques, such as Raman spectroscopy [104] and specific heat measurements [105]. These conclusions were also supported by the temperature dependence of the penetration depth, λ, measured in both single crystals and polycrystalline MgB_2 samples [106] and used to calculate the superfluid density [107]. Although the pairing in MgB_2 is believed to be due to electron-phonon interactions, being a two-gap superconductor it cannot be described by the conventional BCS theory.

From an applications point of view, the value of $H_{c2}(0)$ can be increased by the introduction of charge-carrier scattering impurities into the lattice. This leads to a reduction in the coherence length and an increase in H_{c2}. This rule has been used for the design and manufacture of low temperature superconducting materials over the years. In a two band superconductor, such as MgB_2, there are many scattering sources with different scattering rates. The first one is intra-band scattering within the σ and π bands and the second is inter-band scattering between the σ and π bands. Controlling these inter- and intra-band scattering rates could make

it possible to have very high H_{c2} values in MgB_2, such as 40-50 T in polycrystalline MgB_2 and 74 T in thin films.

2.9.6. Type 1.5 superconductivity

Superconductors can be divided into two classes; type-1 and type-2 according to the behaviour of such materials in a magnetic applied field. In type-1 superconductors, the magnetic field cannot usually penetrate the material, but under certain conditions, such as after rapid quenching from $> T_c$, this can be achieved and vortices formed, which attract each other and vanish upon collision. In type-2 superconductors, the field can penetrate the materials in the mixed state by forming tiny quantized vortices which increase in number with field strength. In this case vortices repel each other and as their numbers grow in an increasing applied magnetic field, they form a vortex lattice [6, 17].

In 2009, Moshchalkov *et al*., were the first to use Bitter decoration show the existence of both types of vortex interaction in high quality single crystals of MgB_2, terming them type-1.5 superconductors. In this type, the vortices repel each other at short distances and attract each other at long distances, becoming arranged into striped and gossamer patterns depending on the strength of the magnetic field and the temperature of the sample [101].

This type-1.5 phenomenon may be explained by supposing that there are two nearly independent superconducting fluids (superconducting electrons), which interact (flow) with one to another as predicted in 2005 by Egor Babaev. He conjectured that the state consists of an interacting mixture of two superconducting components, one type-I and one type-II (see table 6.1) [108].

Two-component superconductors (type-1.5) have two order parameters, ψ_1, ψ_2 [109], and hence will have more than two length scales (not two

lengthscales as is usual in single band superconductors). In many theoretical studies it was supposed that the vortex interaction involves non-monotonic interaction potentials in type1.5 materials, where there is long range attractive force due to an overlap of the outer cores of the vortices and short range repulsive force owing to electromagnetic interaction. If this were the case, then it would imply that there should be a semi-Meissner states with vortex clusters at intermediate fields. In addition, the surface energy at the interface between the normal and superconducting state will be positive at the boundary of the vortex cluster and negative inside, as show in table 1 [108-110].

In 2009, Moshchalkov *et al*. observed an unusual group of vortices with shorter intervortex distances than the average one $a = \left(2\,\phi_o/B\sqrt{3}\right)^{1/2}$, which they terned gossamers. The new vortex structure in MgB_2 applies to all two-band gap superconductors. The two-component character of MgB_2 [111] relates to two different types of electronic bonding, π and σ, giving rise to two superconducting gaps with energies Δ_π = 2.2 meV and Δ_σ = 7.1 meV respectively [36, 112]. Consequently, one can postulated two values of the G-L parameters for the π and σ bands, these being $\kappa_\pi = \lambda_\pi/\xi_\pi = 0.66 < 0.71$ and $\kappa_\sigma = \lambda_\sigma/\xi_\sigma = 3.68 > 0.71$. As a result it can seen that an MgB_2 single crystal could have properties of both type-I and type-II superconductors simultaneously [101].

Finally, Moshchalkov *et al.* suggested that, type-1.5 superconductors can be prepared artificially by placing a thin slab of type-I materials onto a thin layer of type-II materials, and also conjectured that the same phenomena could be observed in iron-based samples as well as any other two-band superconductors.

Table 1: General comparison between superconductor type (type-I, type-II and type-1.5 [109, 110].

	Type-I	Type-II	Type-1.5 (multi-component)
G-L parameter	$\kappa = \frac{\lambda}{\xi} < \frac{1}{\sqrt{2}}$	$\kappa = \frac{\lambda}{\xi} > \frac{1}{\sqrt{2}}$	Type-1.5 have two G-L parameter simultaneously : $\kappa_1 = \frac{\lambda_1}{\xi_1} > \frac{1}{\sqrt{2}}$ $\kappa_2 = \frac{\lambda_2}{\xi_2} < \frac{1}{\sqrt{2}}$
Type of vortex-vortex interaction	Attractive 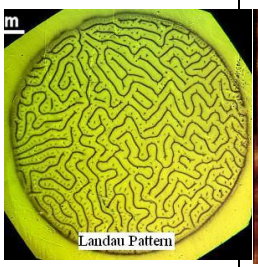	Repulsive 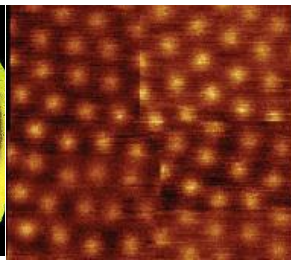	Long range attractive and short range repulsive 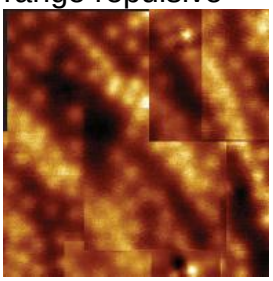
Surface energy sign at the interface between the normal and superconducting states	Positive	Negative	Negative energy inside a vortex cluster and positive energy at its boundary
Superconducting behaviour in a external magnetic field	(i) At low field Meissner state (ii)At relatively larger field, macroscopically large normal domains. 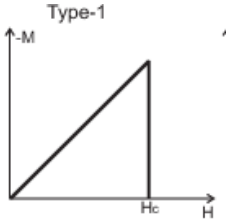	(i) Meissner state below Hc_1 (ii) Mixed state between the Hc_1 to Hc_2 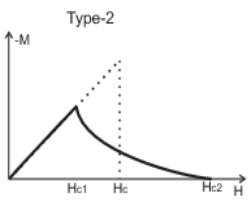	(i) Meissner state below Hc_1 (ii) Between Hc_1 and Hc_2,a semi-Meissner state. (iii) Vortex lattice at high fields 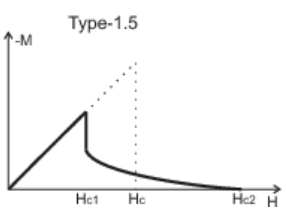

Chapter three: Magnetic imaging &SHPM

3.1. Introduction

The aim of this chapter is to provide an overview of existing and commonly used techniques for magnetic imaging and characterising magnetic properties. The first scanning probe microscope emerged in the early 1980's with the invention of Scanning Tunnelling Microscopy (STM) at the Zürich Research Laboratory of International Business Machines (IBM) by Binnig and Rohrer [113]. The success of Binning & Rohrer with STM technology was closely followed by the development of several other novel scanning probe microscopes, such as the Atomic Force Microscope (AFM), invented in 1986 [114], Magnetic Force Microscopy (MFM), Lateral Force Microscopy (LFM) [115], Ballistic-Electron-Emission Microscopy (BEEM) [116], Scanning Ion-Conductance Microscopy (SICM) [117], Near-field Scanning Optical Microscopy (NSOM) [118], Scanning Thermal Microscopy [119], Scanning Tunnelling Potentiometry (STP) [120], Scanning Hall Probe Microscopy (SHPM) [121] and Scanning Superconducting Quantum Interferences Device Microscopy (SQUID) [122].

A common feature of the majority of the aforementioned microscopes is the ability to investigate a surface phenomenon; their use is well established in surface science to manipulate individual atoms or spin moments on various samples [123]. They can also be employed to investigate domain structures in ferromagnetic materials [124] and vortex structures in superconducting materials [125] using a microscopic sensor to generate an image by manipulating the sensor over the sample surface.

3.2. Overview of magnetic imaging techniques

All magnetic imaging techniques have different strengths and weaknesses. It is therefore essential to bear in mind the main properties of each technique in order to determine which imaging tool is most suited to

the task in hand. The main properties of magnetic imaging techniques that should be taken into account when choosing imaging techniques are as follows:-

- Spatial resolution.
- Minimum detectable field.
- Possibility of quantitative measurements.
- Possibility of measuring other parameters besides magnetic field (such as magnetic susceptibility).
- Invasiveness.

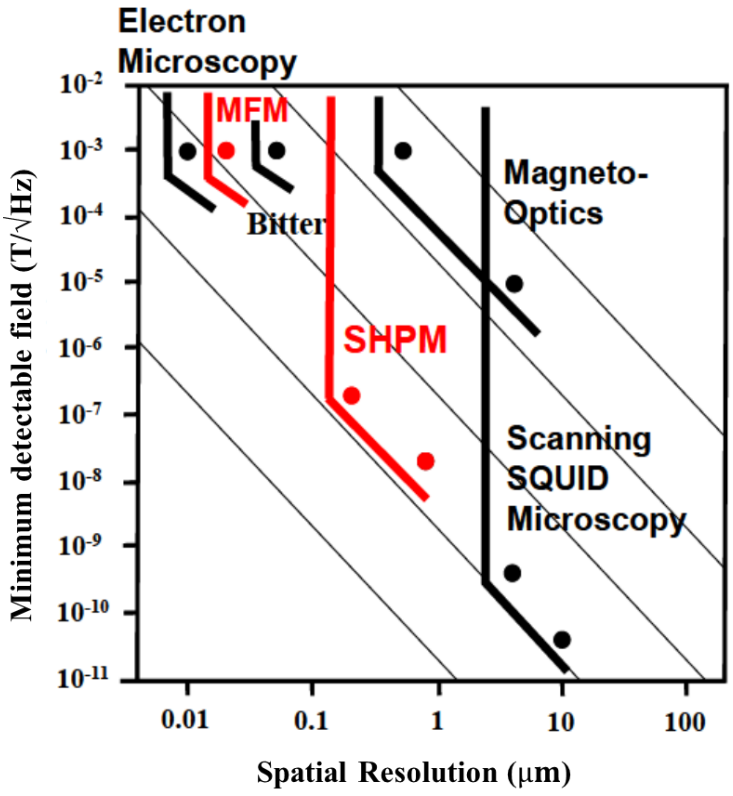

Figure 27: A graph comparing the minimum detectable field and spatial resolution of the principal magnetic imaging techniques [121].

Figure 27 shows a comparison of minimum detectable field and spatial resolution for many leading techniques. The highest spatial resolution is exhibited by electron microscopy, while the highest field resolution is exhibited by scanning SQUID microscopy. The diagonal lines running across the figure provide an indication of the equivalent flux sensitivity.

The SHPM is ideal for investigating vortex matter in superconductors and to lesser extent magnetic domains in ferromagnetic materials, because it represents a good compromise between spatial resolution and field sensitivity.

3.2.1. Bitter decoration

The Bitter-Decoration or Powder Pattern technique is the first method that was developed to image magnetic and vortex structures. It was developed by Bitter in 1931 [126]. In addition the first observation of the Abrikosov vortex lattice was obtained in 1967 by Essman and Trauble using Bitter decoration [127]. In this method, fine particles of a ferromagnetic element such as iron, are dispersed over the magnetic structure using one of various techniques, such as evaporation or liquid suspension. The ferromagnetic particles attract to and deposit on the surface where the magnetic field gradient is highest. The surface is then imaged with an optical [126] or scanning electron microscope (SEM) depending upon the dimension of the patterns. Recently techniques have been developed utilising STM, the magneto-optical Kerr effect or MFM to observe and image the deposited magnetic particles [128].

The liquid suspension method relies upon covering the surface with a colloidal suspension of magnetic particles. These particles accumulate on the areas where magnetic fields are present, and the success of this method depends upon the size of the particles [128]. In the evaporation method, a filament made from a ferromagnetic material such as iron, nickel or cobalt is heated and the particles travel several centimetres in helium gas at low pressure to the sample and deposit under the influence of the magnetic field.

The Bitter Decoration method is a non-quantitative method, i.e., although it allows the direct visualisation of the shape and dimension of the magnetic pattern, no quantitative information can be extracted regarding the magnitude and the direction of magnetisation and the spatial resolution of the technique depends upon the size of the particles. In addition, the

magnetic particles stick on the surface of the sample and may prevent the use of the same sample again without prior cleaning. This demonstrates that the Bitter-Decoration approach is an invasive one. Finally the Bitter-decoration method is only suitable for low magnetic fields below ~ 10mT [129].

3.2.2. Scanning Tunnelling Microscope

The Scanning Tunnelling Microscope (STM) is a surface analytical piece of equipment and widely used in surface science to investigate the microscopic electronic structures of metals [130], semiconductors [131] and superconductors [132], as well as to manipulate individual atoms or spin moments on different materials [133]. More recently, the STM has been combined with cryogenic systems for special measurements. The STM probe is based on tunnelling to/from a conducting tip, which is mounted on a three-dimensional piezoelectric drive. A coarse approach system brings the STM tip into very close proximity to the conducting surface of a sample. If the tip and sample are close enough, electrons can tunnel through the potential barrier represented by the air gap due to the overlap of wave functions. In order to create a tunnelling current, a potential difference is applied between the tip and the sample. The resulting tunnelling current is very sensitive to the potential barrier and the tip to sample separation [134].

For metal surfaces, the electron density near the Fermi energy, E_F, is high, so that with a small bias voltage (typically several tens mV) the tunnelling current is several nA. However, for semiconductors or poorly conductive metals, a bias voltage as high as 1V is applied to obtain on the order of a hundred pA of tunnelling current. The tunnelling current can be measured as a function of the location (x,y), bias voltage V and tip-sample separation z and the output images can yield several important quantities for the sample, such as the topography, the local density of states, etc.

The STM can operate in two modes according to the type of information required. In the first mode of operation, the tip is scanned over a flat plane parallel to the surface and the tunnelling current recorded. This is the 'constant height' mode of operation. The tunnelling current depends exponentially on the tip-sample distance, so the 'constant height' mode is only useful with very flat samples [135]. Therefore, a more common mode of operation is the 'constant current' mode, where a feedback loop adjusts the tip height to maintain the same tunnelling current as the tip is rastered over the sample surface. In this mode, the feedback voltage is proportional to the vertical position of the tip. Scanning in this mode provides a topographic map of the surface of the sample [136, 137]. In general there are many types of complementary measurements: topography mode and current-imaging tunnelling spectroscopy (CITS) mode. In addition, superconductor/insulator/superconductor (S/I/S) measurements and Josephson tunnelling in SS-STM can be used when the tip of STM is fabricated from superconducting materials such as Pb.

3.2.3. Atomic and Magnetic Force Microscopy (AFM, MFM)

Since the Atomic Force Microscope was invented by Binnig *et al*, in 1986 [114], it has become a sophisticated and popular probe for studying a wide range of materials and properties. This technique was invented to measure the van der Waals force between the tip and atoms on the surface [138], as well as long range interactions, such as electrostatic forces (surface charge and capacitance[139, 140]) and magnetic forces[141]. The force sensor is based on a microfabricated cantilever with a sharp tip. This cantilever works like a spring and responds to a force F according to Hooke's law:

$$x = \frac{-F}{k}, \tag{3.1}$$

where k is the spring constant of the cantilever, and x is the deflection of the end of the lever. The deflection of a cantilever is measured by a sensitive sensor and is used to obtain the topography of a sample. There are several methods for deflection measurement such as a tunnelling sensor fixed above the lever [114], a laser and split photodiode [142], a fiberoptic interferometer [143], and a piezoresistive lever [144].

Magnetic Force Microscopy (MFM) uses the same techniques as AFM with the exception that the cantilever tip is coated with a magnetic material [141], This makes the tip sensitive to the magnetic forces from the sample in addition to the short-range atomic force probed by AFM. The output images from an MFM contain information about both the topography and the magnetic properties of the surface. Typically, the magnetic forces dominate for longer tip-to-sample separations than the range of the Van der Waals force. At the same time, most modern MFM systems require a preliminary topographic scan at a close distance followed by a secondary scan at a further distance. The primary topographic scan is later used to guide the cantilever on the surface in order to separate topographic and magnetic effects. With current MFM techniques a resolution of $\sim$ 20 nm can be achieved [145]. Very recently, a 10nm resolution MFM with low temperature imaging capability has become commercially available; the high spatial resolution of MFM technology makes it very valuable.

In the most common measurement modes, the measured signal from the MFM tip is actually proportional to the force gradient, and thus the second derivative of the magnetic field. This makes it more complicated to interpret MFM images quantitatively as compared to scanning SQUID or Hall probe images and it is also much more invasive. However MFM offers significantly better spatial resolution than SQUIDs or Hall probes [145].

3.3. Scanning Hall probe microscopy (SHPM)

Scanning Hall probe microscopy (SHPM) is a relatively new technique, which was first demonstrated by Chang et al [121] in the early 1990's. The SHPM is a powerful quantitative and non-invasive technique for imaging localized surface magnetic field distributions on sample surfaces with high spatial and magnetic field resolution (~ 100 nm & 70 mG/Hz$^{0.5}$), over a wide range of temperatures, 30mK–300K. It is based on the change in Hall voltage when a nanoscale Hall probe is scanned over the sample surface to image the local surface magnetic field distribution. The Hall probe is frequently mounted onto the piezoelectric scanner tube of a commercial low-temperature scanning tunnelling microscope (LT-SHPM) with a stick-slip coarse approach mechanism as shown in figure 28a. In general, Hall probes are fabricated from a two dimensional electron gas (2DEG) heterostructure with low charge carrier density. The active Hall sensor is patterned about 5-10 μm away from the corner of a deep mesa etch which is coated with gold to act as an integrated tunnelling tip. The relative tilt angle of ~ 1– 2^{o} between sensor and sample ensures that this is the closest point to the sample surface as shown in figure 28b. The Hall voltage is proportional to the perpendicular component of the magnetic field as induced by the local magnetic induction, and the maximum scan range is typically 40×40 μm^2, 14×14 μm^2 and 4×4 μm^2 at 300 K, 77 K and 4.2 K, respectively. The time to capture one image depends on the image size, scan speed and scan mode.

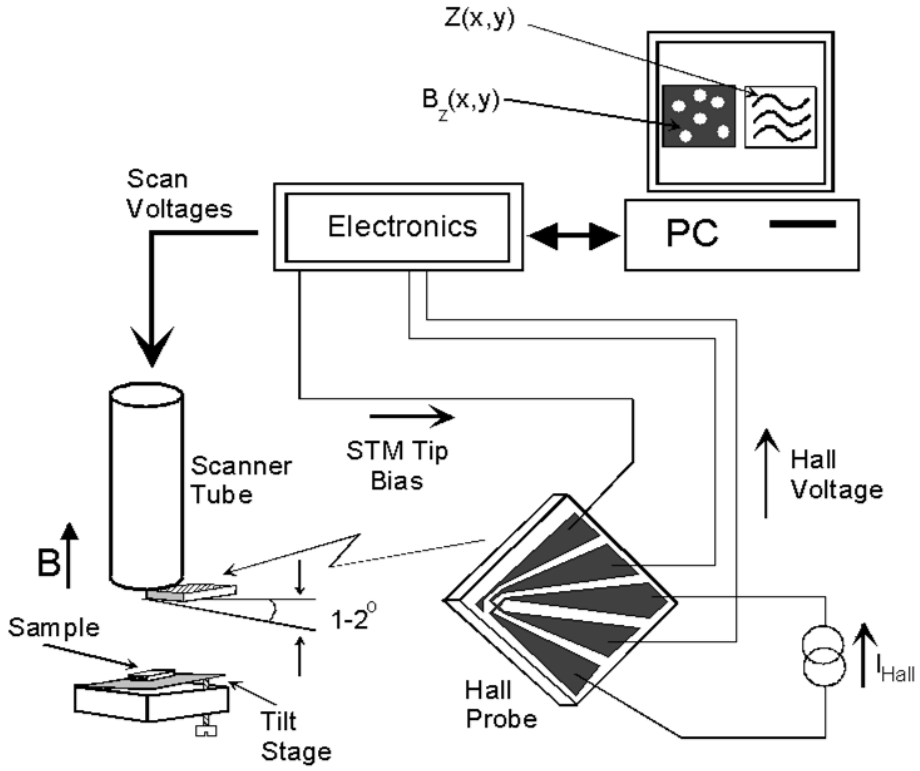

(a)

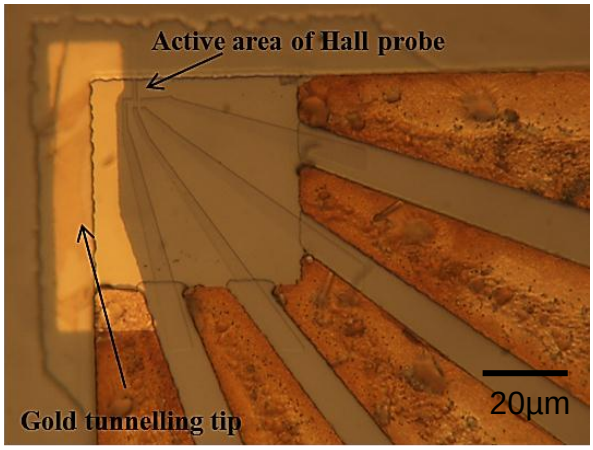

(b)

Figure 28:(a) Schematic diagram of a scanning Hall probe microscope [121], (b) optical micrograph of a 0.8 µm spatial resolution Hall probe.

The SHPM can operate in two modes; the STM tracking mode (figure 29a) and the flying mode (see figure 29b). In the STM tracking mode the sample is approached until a tunnelling current is established between the corner of the Hall sensor chip (tip) and the sample. The Hall probe is then scanned across the surface to measure the magnetic field and surface topography simultaneously. This mode of operation provides the highest sensitivity because it has the smallest probe-sample separation, but in this mode there a is risk of crashing the head. In the flying (lift-off) mode the sample is approached until a tunnelling current is established, then the tip is retracted a certain height above the sample, and the Hall probe scanned much more rapidly with a slightly lower spatial resolution. The main advantages of this mode are speed and avoidance of the risk of a 'head crash' often encountered during the much slower scans with STM tracking.

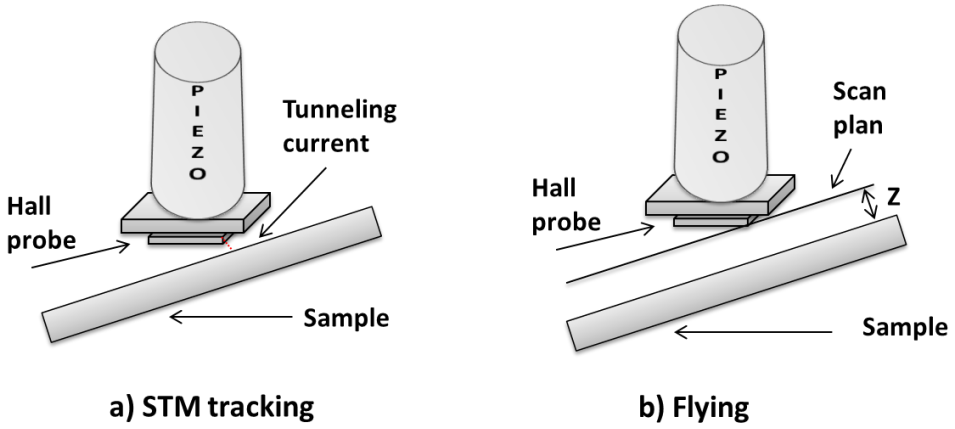

Figure 29: Schematic diagram showing the STM tracking and flying modes of SHPM [121].

The LT-SHPM Nanomagnetic instruments used in this work can be divided into two parts, the microscope body and the SPM electronic controller unit which communicates with the computer.

The microscope body

The microscope body combines all mechanical and electrical parts and consists of a scanner head, flanges, radiation baffles and sample rod, as

show in figure 30, The body fits inside the cryostat with the sample at the centre of a superconducting magnet for low temperature measurements. The temperature of the microscope must be lowered gradually, typically $<$ 2K/min. If there is a large change in temperature over a short time interval, the piezoelectric tube can be damaged.

The head of the scanner is composed of a sample puck, slider piezo, slider, probe head and a scanner piezo, which is used for the high resolution scans and fine approach, as shown in figure 31. The sample puck is fixed to the probe with a spring with an electrical connection for the STM tip. The slider piezo is used for the coarse approach and the coarse *xy* movements. The scan range of the scanner piezo tube of our system is ~ 56µm x 56µm at room temperature in the *xy* plane with a z-extension range of ~ 4.8 µm (the piezoelectric coefficient depends strongly on the temperature). The Hall probe is fixed to the probe head which is located on the scanner piezo. The sample is stuck to the sample holder with silver paint in order to carry the voltage bias to the sample. The front and reverse sides of the sample holder are screwed to each other and a spring allows coarse adjustments of the sample on a slider plate. Sapphire balls between the sample holder and the plate allow this motion to occur smoothly. The slider puck is fixed to the quartz tube using a leaf spring, the angle between the Hall probe and the sample is set using spring tensioned alignment screws as shown in figure 32.

Figure 30: Low temperature SHPM Nanomagnetic Instruments Ltd. head and sample rod [146].

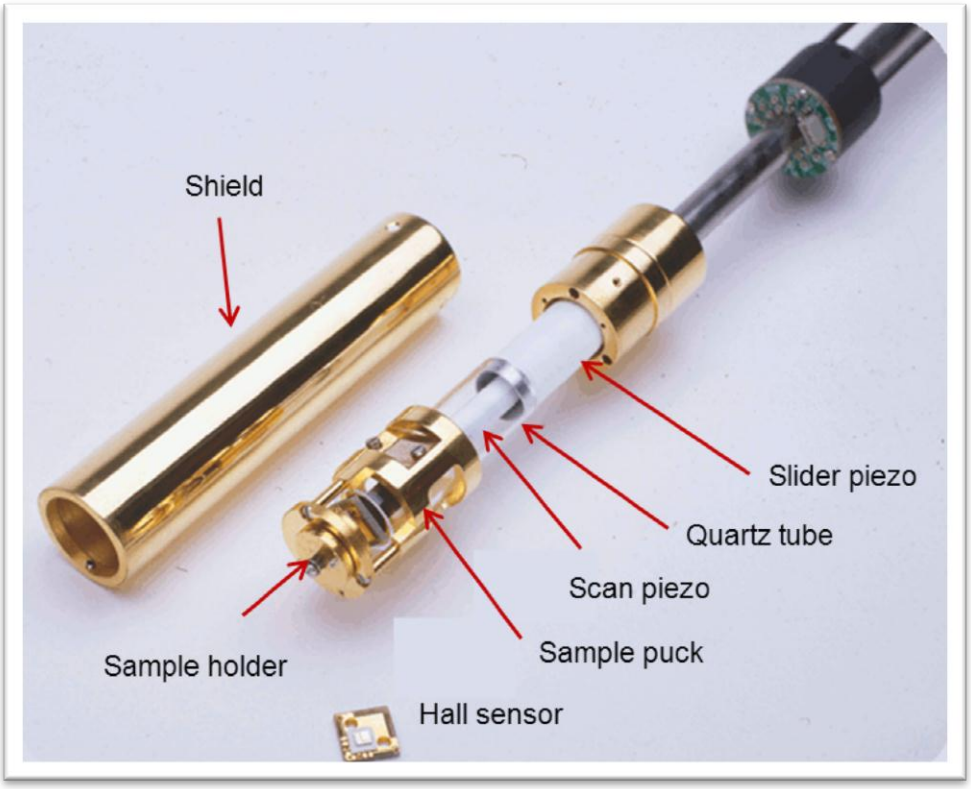

Figure 31: Detailed view of the LT-SHPM (adopted from) [146].

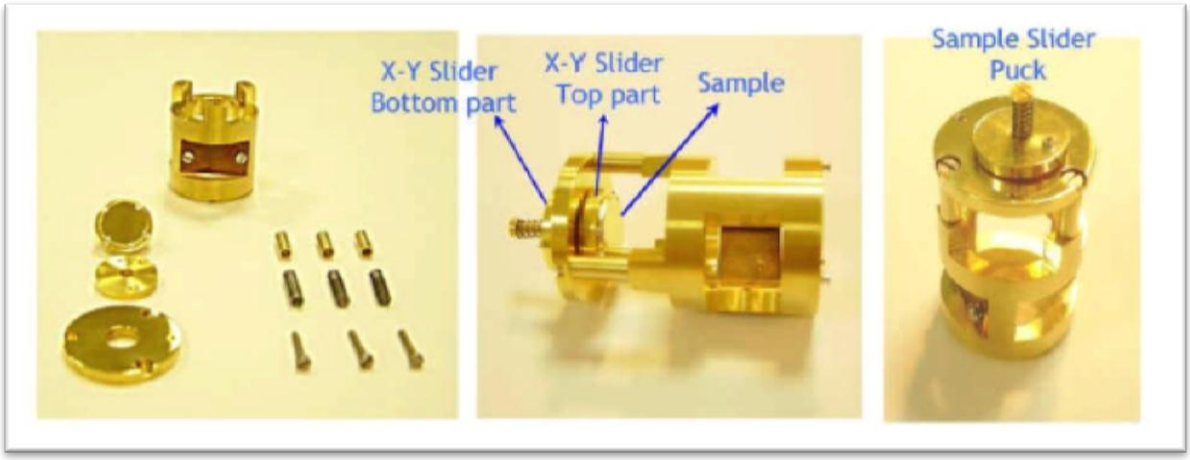

Figure 32: Mounting mechanism for the sample on the holder and then on the slider puck [146].

The Electronics

Operation is controlled by the SPM electronics system. The computer and software are used as the interface for inputting and outputting data, image processing and image saving. The electronic system consists of eight different electronic cards with different functions.

- **Power Supply card**: Supplies the LT&HV power for the whole electronics system.
- **Scan DAC**: Supplies the LT scan voltages in the x-y-z directions.
- **High Voltage Amplifier**: This card generates the high voltages to drive the piezotube in the x-y-z directions.
- **Slider Card**: The slider card provides the t-dependent waveforms for the slider piezoelectric tube.
- **AD Converter Card**: This assists the computer in controlling the electronics and SPM head. It obtains data from interfaces by converting the analog signals to digital ones and also generates analog signals for e.g. controlling the sample voltage.
- **Hall Probe Amplifier Card**: This card regulates the Hall current applied to the sensor and reads out of the Hall voltage from the amplifier. The amplifier contains selectable filters, and provides output $V_{Hall\ out}$ which forms the z-axis of images and can also be viewed on the oscilloscope.

– **Tunnel current controller card**: This controls and determines the value of the tunnelling current (eg., 1nA), the bias voltage between the sample and the tip of the sensor, and reads out the actual tunnelling current between the sample and tip. This can also be viewed on the oscilloscope.

3.4. Magnetic and spatial resolution

Spatial resolution is one of the most important considerations for a magnetic imaging technique since it determines the usability of a probe. The spatial resolution is not only determined by the size of the Hall probe L, but also the height, h, of the Hall probe above the sample surface. Both parameters contribute to the absolute spatial resolution for Hall probes. The xy spatial resolution scales roughly as $\sqrt{L^2 + h^2}$. Thus to obtain a good spatial resolution it is important to have a small active Hall bar and a small distance to the sample. In this regard, the distance between the tunnelling tip and the active Hall sensor, d, and the angle ,α, between the sample and the Hall sensor need to be as small as possible. The Hall probe scan height is determined by the height, h, between the sample and the tunnelling tip, and the sample-probe angle α by the relation $h_{tot} = h + d\tan\alpha$, where the value of angle α usually is around 1-2 degrees and $h' = d\tan\alpha$ (see figure 33).

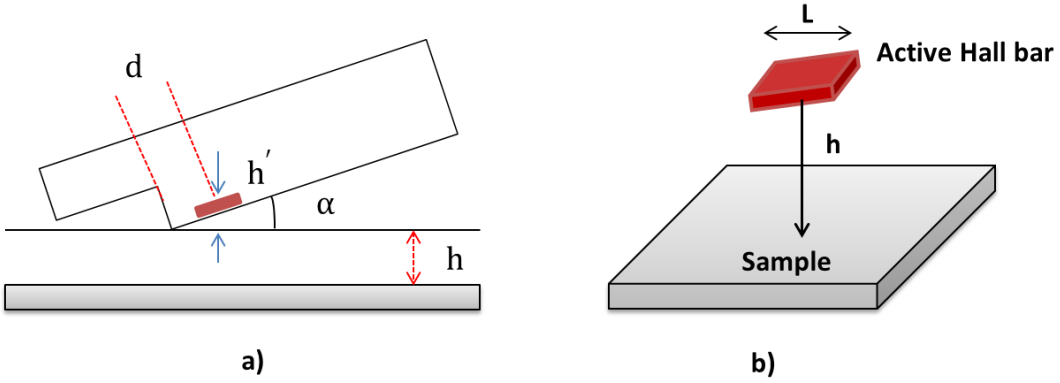

Figure 33: Parameters determining the spatial resolution of the Hall sensor.

Chapter Four: Experimental methods

4.1. Hall probe micro-magnetometry

Hall micro-magnetometry sensors are sensitive and non-invasive tools to detect magnetic flux patterns at the nanoscale over a wide range of temperatures and magnetic fields. The ability to understand, fabricate and control the properties of nanoscale magnetic structures helps to identify new physical phenomena and possible future industrial applications. In this chapter, the basic principles of Hall sensors will be introduced including the Hall effect and the main characteristics of the Hall magnetometer, followed by Hall probe fabrication and imaging systems.

4.2. Basic principles of Hall sensors

In this section, the basic principles of Hall sensors are introduced such as the 2D Hall effect, upon which the Hall devices are based, the Hall sensor material (GaAs/AlGaAs heterostructure) and their figures of merit.

4.2.1. 2D Hall effect

Hall probes are sensors for magnetic fields. These are based on the Hall effect that was discovered In 1879 by Edwin Hall [147]. The Hall effect occurs when a charge current flows in a perpendicular magnetic field. The charge carriers are deflected in the transverse direction due to the Lorentz force and generate the Hall voltage assuming that the current flows through the material strip in the x-direction and a magnetic induction, *B*, is applied along the z direction (as shown in figure 34). The total force acting on the charge carriers is given by [147].

$$\vec{F} = q(\vec{E} + \vec{v} \times \vec{B}), \tag{4.1}$$

where q and v are the charge and the drift velocity of the carriers respectively. The resulting Lorentz force acts in the negative y-direction and generates the electrostatic field, E_y, that prevents any

further charge accumulation. In steady state conditions, $eE_y = ev_xB_z$ and the current flows straight along the x-direction. The Hall voltage is thus given by

$$V_H = wE_y = v_xB_z = \frac{j_xB_z}{ne}\ , \tag{4.2}$$

where w is the width of the conductor, j_x is the current density in the x direction and n is the charge carrier density. Since $j = I/wd$ (d is the sample thickness), the final relation is

$$V_H = R_HIB_z, \tag{4.3}$$

and the Hall coefficient, R_H, is defined as

$$R_H = \frac{E_y}{j_xB} = \frac{1}{ned}\ . \tag{4.4}$$

In the case of a 2DEG, the Hall coefficient can simply be written as $R_H = 1/n_{2d}e$, where n_{2d} is the two dimensional carrier density of the 2DEG.The Hall voltage, V_H, is proportional to the magnetic field and the current and inversely proportional to the carrier density, n, of the conductor. Thus, the Hall effect can be used to determine n and the sign of charge carriers in a material.

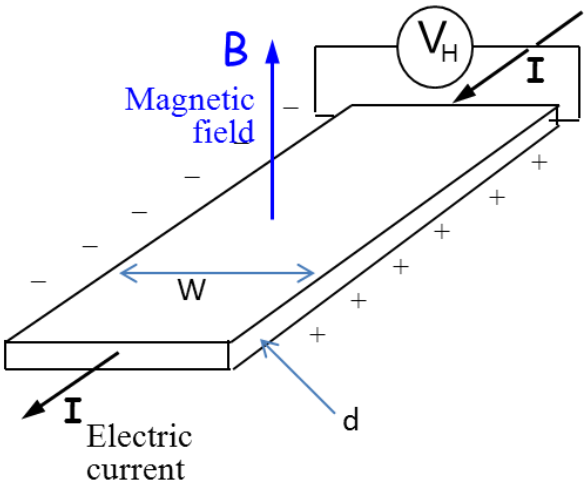

Figure 34: The Hall effect characterised by the formation of a transverse electric field due to the Lorentz force.

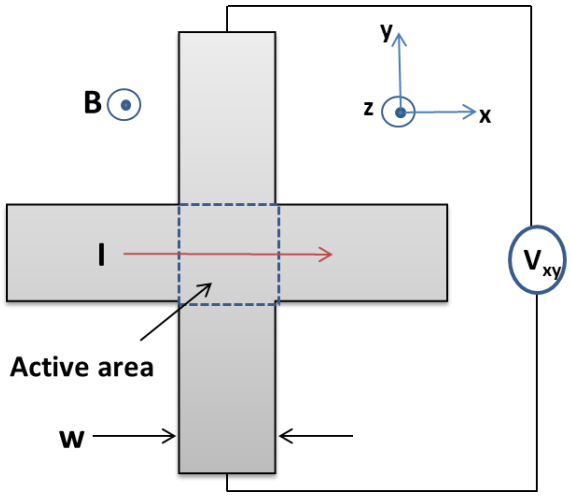

Figure 35: A diagram of a simple Hall cross.

4.2.2. Hall probe devices

The Hall cross is the simplest geometry for a Hall probe as shown in figure 35. The Hall effect can be used to measure the magnetic field if the charge density, n, is known. The Hall signal (Hall voltage) is proportional to the magnetic induction which threads the active area when the sample is

placed near the Hall probe. In this case the Hall device can be used as a field sensor if the material characteristics, device geometry and the bias current are known [148].

4.2.3. Hall probe material

The efficiency of the Hall effect is based on the relationship between the Hall voltage and the bias current as shown by the following equations

$$\frac{V_H}{I} \sim \frac{I}{nd} B_z, \tag{4.5}$$

$$\frac{V_H}{V} \sim \mu B_z, \tag{4.6}$$

$$\frac{V_H}{P^{1/2}} \sim \left(\frac{\mu}{nd}\right)^{1/2} B_z, \tag{4.7}$$

where n is the carrier density, d the plate thickness, μ is mobility of the free carriers and $P = IV$ is the dissipated power.

From equations (4.5), (4.6), the ratio of the Hall voltage and the drive current is inversely proportional to the carrier density and the thickness of the plate. At the same time, the ratio of the Hall voltage and the drive voltage is directly proportional to the mobility of the charge carriers. This indicates that a suitable material for a Hall sensor must have a low carrier concentration and/or a relatively thin Hall plate and high carrier mobility. The Hall effect in a semiconductor is typically large because it has low carrier concentration ($\sim 10^{14}$-10^{18} cm^{-3}) as compared to metals which have very large carrier densities. High carrier mobility and low carrier concentration also give a high Hall voltage per square root power as shown in equation (4.7).

The semiconductor compounds InSb and InAs have the highest value of room temperature electron mobility, i.e. μ_n ~8×10^4 $cm^2\ V^{-1}\ s^{-1}$ and μ_n ~3.3×10^4 $cm^2V^{-1}s^{-1}$, respectively. However these compounds have high carrier densities at room temperature due to their small band gaps: E_g=0.18 eV and E_g = 0.36 eV, respectively. For this reason, it is often more appropriate to choose an extrinsic semiconductor with a larger band

gap, preferably doped n-type because the electron mobility is larger than the hole mobility in all known semiconductors. Semiconductor heterostructures are relatively new materials which are fabricated by epitaxial growth techniques. These heterostructures contain a low density two-dimensional electron gas (2DEG) with extremely high mobility. Thus they are ideally suited for the fabrication of Hall sensors[149]. The GaAs/AlGaAs heterostructure will be discussed in the next section. This is used in this work as the Hall sensor material and can attain electron mobilities of the order of μ ~2.89×10^{6} $cm^{2}\ V^{-1}\ s^{-1}$ at low temperature.

4.2.4. GaAs/AlGaAs heterostructure

The most widely used material system for fabricating 2DEGs is gallium arsenide (GaAs), which is a III-V semiconductor. A cross-sectional view of a typical GaAs/$Al_xGa_{1-x}As$ heterostructure is shown in figure 36. Beginning from a substrate wafer of semi-insulating GaAs, a thick layer of undoped GaAs is first grown. This is followed by a spacer layer of undoped AlGaAs and then a layer of AlGaAs doped with Si. Finally a thin cap layer of GaAs is added to protect the reactive AlGaAs layer. An energy band diagram showing the formation of a 2DEG at the interface between the undoped GaAs and the AlGaAs layers is presented in figure 36. The difference in the energy of the conduction band in these two materials gives rise to a narrow potential in discrete energy levels that define the bottom of the 2D sub-bands. The remote AlGaAs n-type dopants provide electrons which fill up these bands [121].

The electron density is controlled by the spacer layer thickness and the doping concentration. For a sufficiently thick spacer layer thickness the mobility is determined by the unintentional impurities in GaAs as opposed to ionised donors. These are in turn determined by the cleanliness of the growth chamber. Thus the mobility can be controlled by adjusting the spacer layer thickness since it spatially separates the main source of scattering, the charged donors in the doped AlGaAs layer, from the plane of the 2DEG [121].

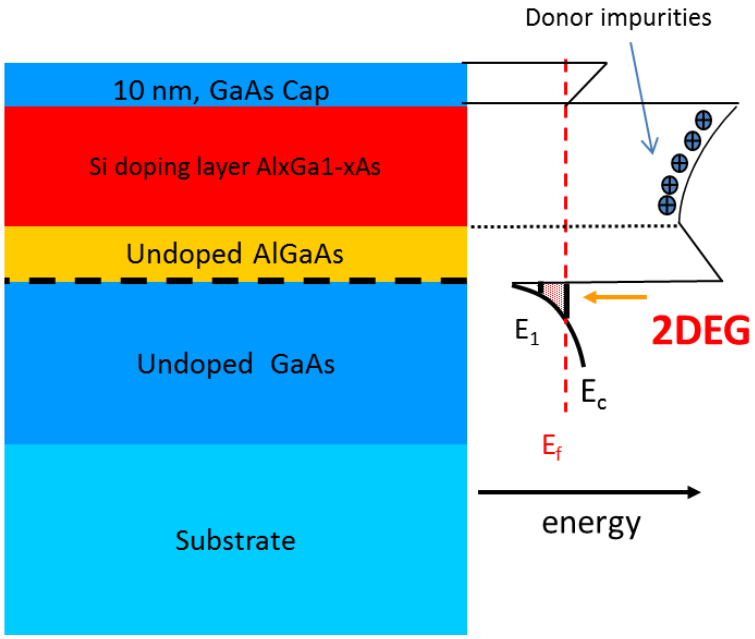

Figure 36: (Left) Typical layer structure for a GaAs/$Al_xGa_{1-x}As$ heterostructure. (Right) schematic energy band diagram [121].

4.2.5. Hall probe sensitivity

The Hall sensor works as a signal transducer to convert the component of the magnetic induction threading the active area (input signal) into a Hall voltage (output signal). The signal to noise ratio (SNR) is the most important figure of merit of a Hall sensor. It is defined as the ratio between the Hall signal ($V_H = I_{Hall} R_H B$) and the electrical noise present in the measurements. The signal to noise ratio (SNR) should be maximised for better performance.

$$SNR = \frac{R_H I_{Hall} B}{V_{Johnson}} \tag{4.8}$$

where the Johnson noise, ($V_{Johnson} = \sqrt{4k_B T R_s \Delta f}$), due to thermal fluctuations is often assumed to be the main source. It is generated by random motion of the charge carriers and depends on the series

resistance of the device, R_s, the measurement bandwidth, Δf and the absolute temperature, T, [150].

From equation 4.8, it is clear that by increasing the value of the driving current the SNR noise can be increased, but above a critical value low frequency noise is found to increase rapidly. In addition the value of the current may also be bounded by self-heating effects. Hence it is clear that there is an optimal value for the drive current, I_0 , which is material dependent and maximises the SNR [151].

4.3. Hall probe sensor fabrication

The fabrication of the Hall sensors was performed on GaAs/AlGaAs heterostructures in which a 2DEG was formed at one of the GaAs/AlGaAs interfaces. The process took place in a class-1000 clean room at the University of Bath using various process techniques such as photolithography, thermal evaporation, electron beam lithography and wet etching. There are six production steps in Hall sensor fabrication:-

- Metallisation (Ohmic contact formation).
- Mesa etch.
- Tip metallisation.
- Hall probe etch (Fine etch).
- Deep etch.
- Scribing and cleaving into four devices.

4.3.1. Process Techniques

1. Optical lithography

Optical lithography is a technique used to obtain the accurate transfer of a pattern from a mask onto a resist layer. This is achieved by bringing the mask into contact with the resist, shining a UV light through the mask and then developing the resist. The first element of optical lithography is the photoresist, an organic polymer in a solution which is sensitive to ultra violet (UV) light. There are two types of resist: positive resist where the UV

light weakens bonds within the polymer and negative resist where the bonds are strengthened by exposure. For the positive resist used here bond breaking produces a duplicate of the mask design (whereas negative resist produces a negative of the mask). The resist is dropped onto a wafer which is then spun at high speeds to spread the resist into a thin film. The spinning speed and duration lead to a controlled layer thickness. At this stage the resist is normally baked for 30 minutes at 90^0C to remove any residual if this is in preparation for an etching process (see figure 37). If the design requires material to be deposited onto the wafer via evaporation, the resist is baked for 15 minutes, soaked in chlorobenzene for 5 minutes and then baked for a further 15 minutes. This process hardens the top surface of the resist, as shown in figure 37 giving an overhang profile after developing [152]. To transfer the pattern a mask aligner is used. This is essentially a powerful microscope combined with x, y, z, sample translation and rotation stages and an ultra violet light source. The exact exposure time varies with the age of the UV bulb and is typically around 10 seconds. Under or over exposure will make it difficult to obtain a sharp developed pattern but this can be compensated for by altering the development time. Each resist has its associated developer, a chemical solution which attacks the weak bonds and dissolves the polymer. Typical development times are between 30-60 seconds depending on the exposure time, after which the reaction is quenched by washing with deionized water (DI). The final result should show clean sharp boundaries between the resist layer and the exposed wafer surface[153].

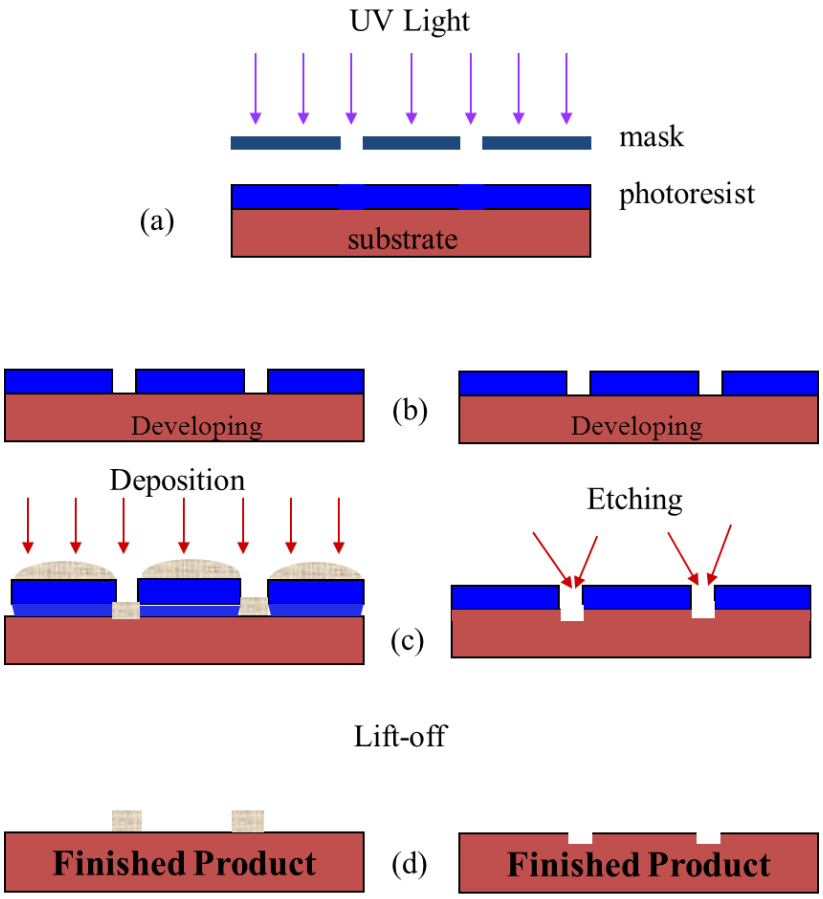

Figure 37: Key steps in device processing: A) The wafer is prepared with resist ready for UV exposure through a mask; B) wafer and resist after development, C) deposition of new material by evaporation (left) and etching (right); E) finished wafer after removal of resist.

2. Metallisation (Ohmic contact formation)

The purpose of the metallisation (Ohmic contact formation) is to realise low resistance electrical connections to the device which are necessary for allowing current to flow into it. Ohmic contacts for GaAs/AlGaAs Hall probe sensors require four different layers to be evaporated: 66nm of germanium, 134 nm of gold, 10 nm of titanium and a further 200 nm of gold). The first two layers are designed to make good electrical contacts once the layers are alloyed and diffused down into the sample to the depth of the 2DEG [154].

The diffusion process is controlled by annealing using an oven with a regulated inert gas (95% N_2 and 5% H_2) flow and a powerful illumination source which rapidly heats samples placed on a Si wafer in the chamber. The diffusion of contacts depends on the temperature and anneal time. As the temperature increases the germanium/gold layers alloy and diffuse into the wafer. The Titanium prevents the surface from becoming rough or balling while the final gold layer helps to reduce the contact resistance and provides a layer suitable for ultrasonic bonding.

3. Wet Etching

The wet etching process uses a wet chemical (usually acidic) solution as an etchant to remove material, and proceeds through chemical reactions occurring at the surface. There are many factors which affect the rate of chemical reactions, such as temperature, bubbles and crystalline orientation. As with all chemical reactions, etching is very sensitive to temperature. A 10°C increase in temperature can increase the etch rate by a factor of two. Freshly mixed etchants may be hot, while some etching conditions may produce bubbles, usually hydrogen, which can adhere to the surface being etched and cause non uniform etching. This can be alleviated by agitation or using surface-active (wetting) agents. There is a strong tendency for etching to result in exposure of various crystalline planes. This process can be adversely affected by poor adhesion of the resist mask or diffusion effects. If the mask material does not adhere

perfectly to the wafer surface the resulting etch profile will be compromised. Unbaked photoresist is particularly susceptible to this problem. Diffusion effects near the mask edge can also lead to a less sharp profile. All these effects must be considered in establishing reproducible and controllable etching processes [153].

The H_2SO_4:H_2O_2:H_2O system is a very common etching solution for GaAs processing. These etchants operate by first oxidizing the surface and then dissolving the oxide, thereby removing some gallium and arsenide atoms. Generally, the etchant will contain one component that acts as the oxidizer and another that is the dissolving agent. In this case hydrogen peroxide is the oxiding agent, while sulfuric acid dissolves the resulting oxide. The rate of etching is determined by the ratio between the components of the etching solution [154]. This etching system is often used for etch polishing substrates, mesa etching, or deep etching.

4. Electron Beam Lithography (EBL)

Electron beam lithography (e-beam lithography) is similar to photolithography, with the main difference being that the pattern is printed with a focused electron beam on a special e-beam resist. This means that the UV light is replaced by a very narrow scanned electron beam and E-beam lithography can attain feature sizes down to 50 nm. In addition, it makes photomasks unnecessary as the electron beam is focused and scanned directly on the resist with the help of a set of electromagnetic lenses. This is done in a UHV environment in a scanning electron microscope (SEM). In this work, the choice of resist is PMMA (Poly Methyl Methacrylate). The quality of the patterning depends upon how well the e-beam is focused [153].

4.3.2. Fabrication steps

1. Substrate preparation

Before beginning the fabrication process, a GaAs/AlGaAs heterostructure is cleaved into 6mm X 6mm square chips using a diamond scriber. During this process some small particles broken from the wafer may scratch or stick to the surface. For this reason the chips are cleaned in a standard way which involves three solvent cleaning steps, namely keeping for five minutes in tricholoroethylene, acetone and isopropanol, respectively in an ultrasonic bath at 15% power. The chips are then dried using high pressure nitrogen gas.

2. Ohmic contact deposition

The clean chips are stuck on glass cover slips (rotated at a 45° angle to spread the resist to the corner of the chip) using Shipley Microposit S1813 photoresist with the active side facing up. They are then baked at 90^0 C for 45 minutes. This step is carried out to ease manipulation of the chips during the fabrication process without scratching them with a pair of tweezers.

Shipley Microposit S1813 (SU1813) resist is spun onto the chips at 3500 rpm for 30 seconds to produce a thick resist layer ($\sim 1.5\mu m$). The resist is then baked in an oven at 90^0C for 15 minutes. After the first baking step, the chips are soaked in chlorobenzene for five minutes to harden the top layer of the resist by removing the solvent from it. This leads to the formation of an overhang profile when patterned. The resist is then baked again for 15 minutes at 90^0C.

To pattern ohmic contacts, the resist is exposed for about 10 seconds (depending upon the age of the UV lamp in the mask aligner) through a chrome-on-glass photolithographic mask using a Karl Suss MJB3 mask aligner. The resist is then developed using Microposit 351 developer. The

H_2O:developer ratio is 3.5:1 and the chips are rinsed in distilled water and dried using a Nitrogen gun.

To form high quality ohmic contacts, the surface oxide is removed from the chips by dipping them in a 1:1 HCl: H_2O solution for 30 seconds and then rinsing them in DI water for 10 seconds. As soon as the oxide is removed the chips are mounted in a thermal evaporator and a low voltage Ar glow discharge used in situ to ensure that the chips are free of organic residues.

The contact materials: 66nm Ge, 134nm Au, 10-20nm Ti and 200nm Au, are evaporated sequentially in the same operation under high vacuum (2-3x10^{-6} mbar) forming high quality metal layers. The first two layers make an ohmic contact with the 2DEG, while the second two layers enable wire bonding using an ultrasonic bonder. The unwanted metals were then 'lifted off' by placing the chips in acetone overnight in a polypropylene beaker and drying with a Nitrogen gun. The chips are annealed under forming gas (95 % N_2 and 5% H_2) at 425^{0}C for 15 seconds in order to form good electrical contact to the 2DEG (see figure 38).

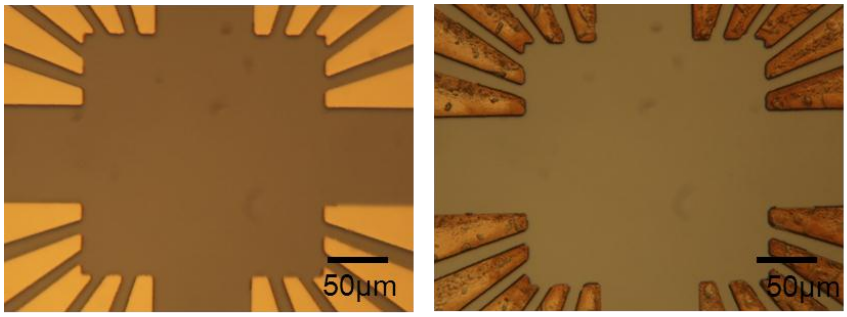

Figure 38: Optical images of ohmic contacts on a chip, (a) after lift-off and (b) after annealing.

3. Coarse lead isolation etching

The 2DEG regions between ohmic contact leads are removed by wet chemical etching using the following steps:-

Firstly the chips were mounted on cover slips following the standard procedure. The chips were then coated with SU1813 photoresist at 5000 rpm for 30 seconds to form a resist layer ≈ 1 μm thick. They were then baked at 90^{o} C for 30 minutes and then exposed in the mask aligner through the mask.

Before etching the surface oxide layer was stripped by dipping the chips in a 1:1 HCl:H_2O solution for 30 seconds. They were then washed in DI H_2O for 10 seconds. Once the oxide was removed, the chips were immediately dipped in (H_2SO_4:H_2O_2:H_2O) (1:8:160) solution to etch them to a depth of 70nm at typical rates of 260nm/min.

Prior to this a test chip was etched and measured with a Dektak Profilometer and the etching rate calculated. The resist was then stripped in acetone and the chips examined under an optical microscope see figure 39.

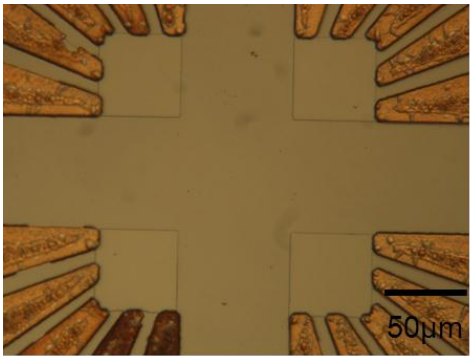

Figure 39: Optical images of a chip after coarse lead isolation etching.

4. Tip deposition (STM)

All patterning and cleaning steps were performed in the same way as for the ohmic contacts except the resist spin speed was increased to 5000 for 30 seconds. The tip was formed from a 10 nm thick layer of Ti followed by 50 nm layer of Au, without any subsequent annealing (see figure 40).

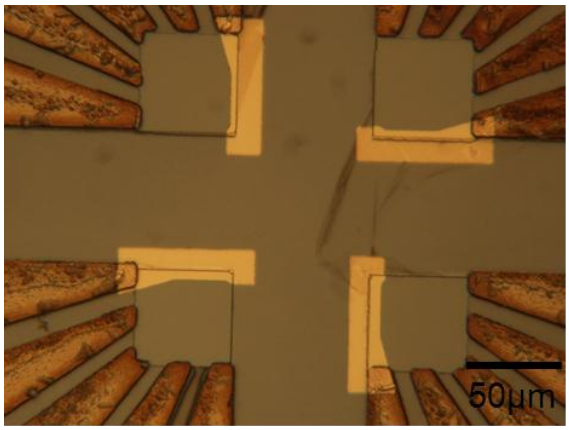

Figure 40: Optical image of a chip after tip evaporation.

5. Hall Bar " fine etch"

Hall probe definition is the most critical step in Hall sensor fabrication. Hall sensors used for scanning Hall probe microscopy and Hall magnetometry in this thesis had sub-micrometer dimensions. This resolution cannot be achieved with the standard optical lithography tools which were discussed earlier in this chapter. As an alternative, electron beam lithography (EBL) was used to pattern these structures.

The chips were cleaned using the standard method but not mounted on a cover slip. The chips were then coated with Poly Methyl Methacrylate (PMMA) spun on at 5000 rpm for 30 seconds. They were then baked for 20 minutes at 155^{o}C on a hot plate. A Hitatchi S4200 field-emission scanning electron microscope (SEM) connected to a Raith Elphy Plus pattern generator was used to write our Hall bar structures with an active size $\simeq$ 0.8 µm, where each 6mmX6mm chip contained four Hall sensors. The resist was developed using 1:3 MIBK (methyl isobutylketone): isopropanol for around 15s, and then the rinsed in isopropanol for 10 seconds.

Following PMMA development, the active area of the Hall probe was defined using a slow etching solution (1:8:1000) H_2SO_4:H_2O_2:H_2O with an approximate etch rate of $\simeq$ 40 nm/min to better control the etching

process. This is performed without using a 1:1 HCl:H_2O dip solution to remove surface oxide as PMMA could react with this solution. The etching process for a sub-micron Hall probe must be carefully controlled. The resistance between ohmic contact leads is measured using a probing station after a minute of etching. If the resistances are too low, the etching process is repeated for 30 seconds; this process was repeated until the resistance of Hall probe leads became around 40 kΩ. After the etching process, the chips were cleaned in acetone and isopropanol to remove the PMMA as shown in figure 41.

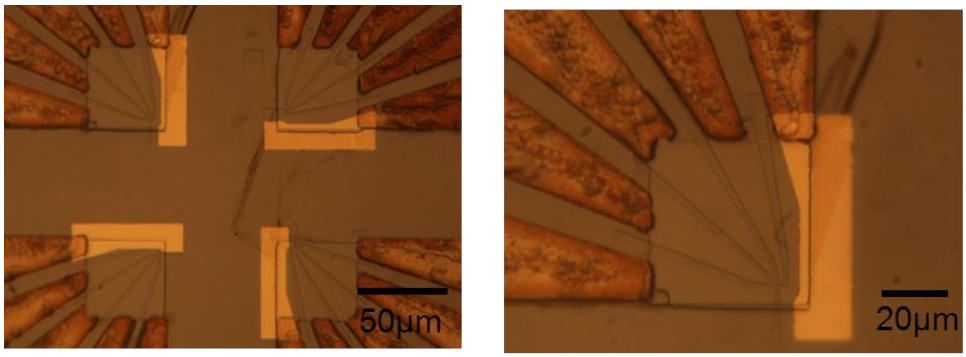

Figure 41: Optical images of a chip after fine etching at different magnifications.

6. Deep etching and sensor separation

The design for making the STM tip places it at the highest point near the corner of the Hall probe to ensure that it comes into contact with the sample first.

Deep etching to a depth of ~1µm was performed in the same way as for coarse lead etching except the etching solution was (1:8:80) H_2SO_4:H_2O_2:H_2O with an approximate etch rate of 540 nm/min, see figure 42. After etching, the chips were cleaved into four Hall probes using a diamond scriber. The resist was then removed with acetone and isopropanol.

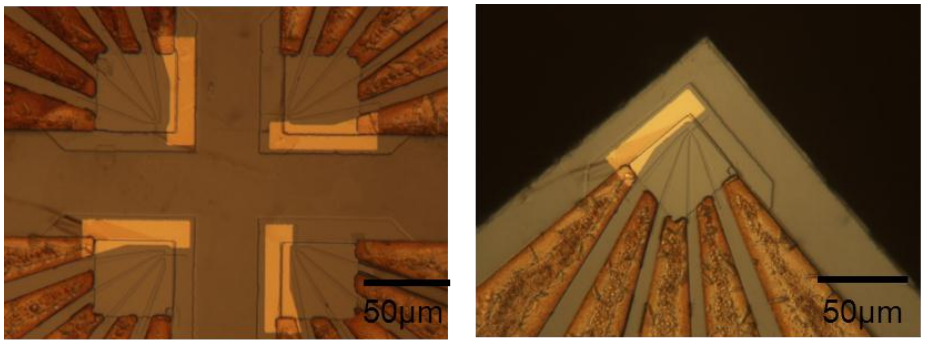

Figure 42: Optical images of the chip: (a) after deep etching and (b) after cleaving.

7. Final test for Hall probe

To ensure there are no open circuit leads in the dark at low temperatures, the resistances of all the leads are measured at 77 K in the dark using a probing station and a home-made liquid nitrogen bath.

8. Mounting of sensors

The Hall sensors were mounted on a chip carrier using Oxford Instruments low temperature epoxy. The Ohmic contact leads were then bonded to the chip carrier using 25 μm diameter gold wire in an ultrasonic wire bonder. The chip carrier was then screwed onto the SHPM Head (see figure 43).

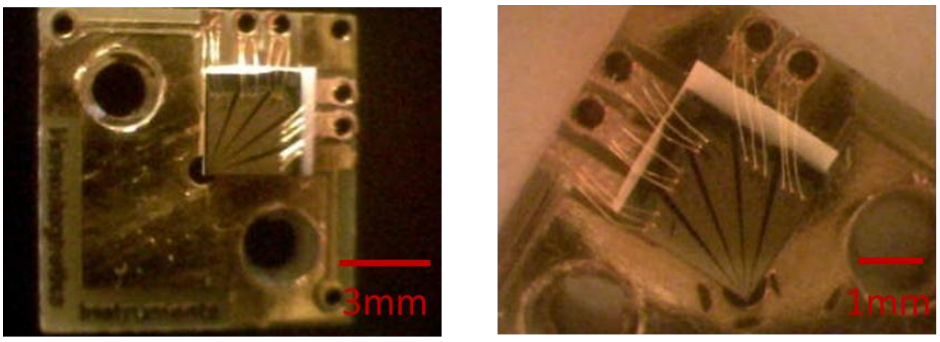

Figure 43: Optical image of a sensor after mounting on a chip carrier and wire bonding and a magnified image of the Hall probe.

9. Mounting the sample on a puck

Before mounting a sample on a sampler holder puck, it was normally coated with gold to form a highly conductive surface allowing a tunnel current to flow between the tip of the Hall probe and the surface of the sample. The sample was then glued onto the sample puck of an XY slider with silver conductive paint and left to dry for 30 minutes.

The sample puck was then mounted on the SHPM Head (see figure 44), and the angle between the sample plane and the Hall probe adjusted to be 1-2 degrees. If the angle between the sample and the Hall sensor was not correct, the sensor could crash into the sample surface and damage both the sensor and the sample. After alignment, a gap is usually left between the Hall sensor and the sample of around 250 µm.

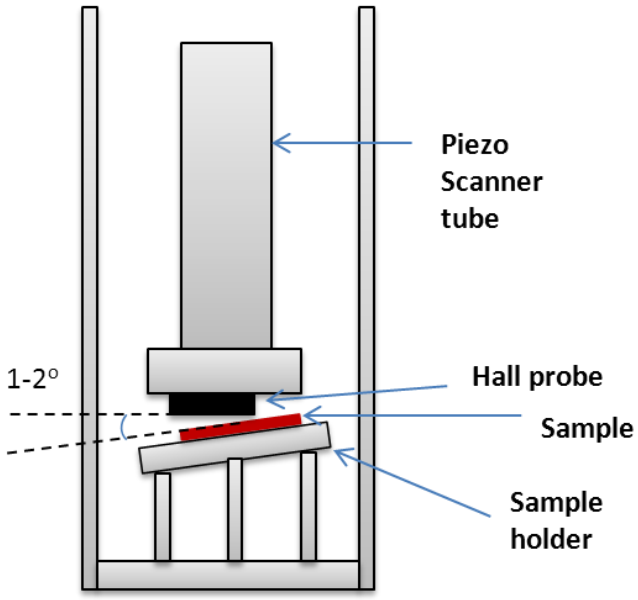

Figure 44: A diagram of the Scanning Hall probe Microscope head after mounting the Hall probe and sample.

10. Sample approach and image scanning

After the system has cooled below T_c, a coarse 'stick-slip' approach mechanism was used to bring the sample and Hall probe together until a

tunnel current was detected at the tip. The puck was then retracted one step, the corners of the sample checked and the sample scanned.

4.4. Cryogenic measurement system

The scanning microscope was housed in an Oxford Instruments variable temperature cryostat system. This could be used to span a wide range of temperatures from 4.2 K to 300 K using Liquid Helium (LHe) and Liquid Nitrogen (LN_2) as coolants. The cryostat consists of an outer vacuum isolation jacket, a Dewar for LN_2 or LHe and a sealed sample space in an inner chamber. A needle valve allows cryogen to flow from the He bath through a heat exchanger around sample space, and the temperature can be controlled using an ITC Model 503 Oxford Instruments Intelligent temperature controller with a Carbon glass sensor (0.1-300K). The cryostat is mounted on a suspended aluminium frame with pneumatic pads to isolate the system from sources of external vibration.

A magnetic field could be applied from a superconducting magnet a solenoid wound from superconducting NbTi wire. The sample must be placed accurately in the centre of the coil to obtain a calibrated field.
The magnet has a superconducting switch which consists of a length of superconducting wire non-inductively wound in parallel with the solenoid with an integrated electrical heater. This superconducting wire is driven normal by raising its temperature using the heater. When the wire switch is ‘open’ current from the power supply can be fed into or out of the superconducting magnet windings. The switch returns to its closed state when the heater is turned off and the switch element becomes superconducting again.
To perform low temperature experiments, the cryostat is normally cooled first by liquid nitrogen in a process called pre-cooling. Once the system has cooled to 77K, the liquid nitrogen can be replaced by liquid helium in the same bath space and the system cooled to 4.2 K. When working at

low temperatures it is vital to have very pure He gas in the sample space. This is because if any impurity or water vapour is present at room temperature, it will liquefy and then solidify on the sample as the system is cooled down. High purity Helium exchange gas is used to flush the system.

4.5. MilliKelvin scanning Hall probe microscope

The milliKelvin Scanning Hall probe microscope (SHPM) head was designed at the University of Bath [155] and is shown in figure 45. The basic concept of this design allows it to be mounted on a commercial Oxford Instruments Heliox ^{3}He refrigerator (Oxford Instruments, Heliox VT-50), and also provides easy access for mounting the Hall sensor and sample, and for precise adjustment of the sensor location and angle with respect to the sample.

The microscope body is designed to fit into an Oxford Instruments variable temperature insert (VTI) which includes an 11T superconducting magnet system within an Oxford Instruments helium cryostat. The microscope body consists of the electrical connector, sample holder, tube scanner and a stack of positioners. All these items are combined together inside a brass holder, with the outside surfaces highly polished to reduce radiation into the head. The base temperature of our system is around 300–400 mK, and this temperature can be maintained with the SHPM head operational for up to 24 h. This time is generally reduced to three hours when the microscopic is scanning. Once the ^{3}He shot is exhausted, a new ^{3}He-condensation cycle is needed to restore mK temperatures which takes about 20 minutes. During the operation of a ^{3}He condensation cycle, the temperature of the 1 K plate is held at ~1.50 K and controlled by the pumping rate of the variable temperature insert (VTI) (the flow rate from the helium bath through a needle valve). The temperature of the Heliox cold plate is controlled by a temperature controller (ITC503).

The controller electronics for the mK-system consists mostly of the commercial SPM-controller from NanoMagnetics Instruments Ltd., which provides scanning signals, automatic surface approach and data acquisition. Several additional electronic units have been built to meet the demands of our microscope system such as a new high-voltage amplifier to increase the scan range 2-3 times. The maximum scan range is about 14μmX14μm at 0.3mK. A three-channel controller for the Attocube positioners was also constructed to provide coarse x-y-z motion [156].

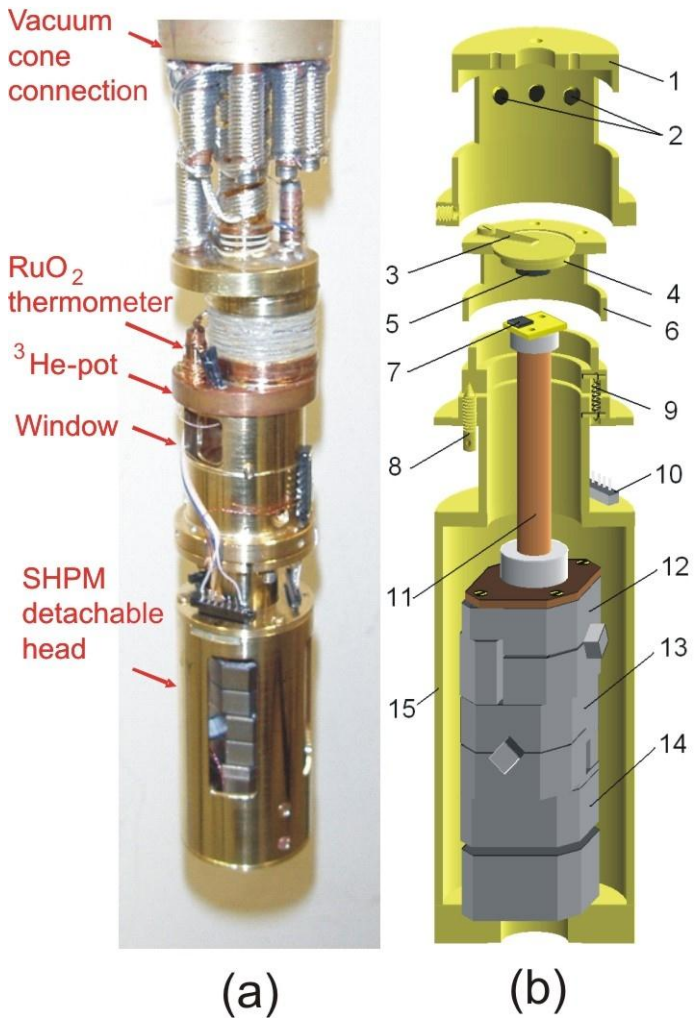

Figure 45: A sketch of a scanning Hall probe microscope head designed to fit on the cold flange of a commercial 3He refrigerator. (1) Receptacle tube, (2) LED array, (3) Bronze flat spring, (4) Sample holder disc, (5) Sample, (6) Sample holder cup, (7) Hall probe,(8) Alignment screw, (9) Extension bronze spring, (10) Electrical connectors, (11) Piezoscanner tube, (12) and (13) ANPx100 positioners, (14) ANPz100 positioner, (15) Brass microscope hull [124, 156].

Chapter five: Multiband superconductivity in Co-doped 122-iron based superconductors single crystals

5.1. Introduction

In 2008, the discovery of superconductivity in the Fe-based system $LaFeAsO_{1-x}F_x$ at 26 K [11] excited new research activity around the world to investigate and understand the properties of these compounds. The highest value of T_c=55K, was achieved by replacing La by Sm in $SmFeAsO_{0.9}F_{0.1}$ [157]. The number of iron-based superconductors rapidly increased after this and is now divided into many families, such as the ternary '122' compounds MFe_2As_2 with the $ThCr_2Si_2$ crystal structure (M = Sr, Ba, Ca), which is based on FeAs layers. The MFe_2As_2 compounds have the simplest crystal structure, and the parent compounds of this family are bad metals with tetragonal crystal structural. The structural and magnetic transitions happen simultaneously in this material [63] ($T_{n(s)}$ = 205K in $SrFe_2As_2$ and 135K in $BaFe_2As_2$ [78]), as discussed earlier. Superconductivity has been discovered in various 122-compounds with hole [62] or electron [75, 158] doping. In addition, hydrostatic pressure can induce a superconducting state in the 122-parent compounds such as $CaFe_2As_2$ [78, 159], $SrFe_2As_2$ [158, 159], and $BaFe_2As_2$ [160]. In general, the T-P phase diagram shows a strong similarity to the T-x phase diagram for hole and electron doping.

Band structure calculations based on the local density approximation indicate that multiple bands contribute to the Fermi surface in the 122-compounds and these contain at least two hole and two electron pockets. Moreover, ARPES measurements [89, 93, 161-163] show isotropic nodeless gaps with two distinct energies on different parts of the Fermi surface and there is growing evidence for an s± pairing state where the sign of the order parameter is reversed on the hole and electron pockets [27, 94, 164, 165]. This s± two-band picture is, however, only an approximate

effective theory and does not take into account the true band structure with up to five bands intersecting the Fermi surface. Hence we are far from having a complete understanding of the physics of these fascinating materials.

The magnetic penetration depth, $\lambda(T)$, and its temperature dependence are sensitive probes of the superconducting gap and order parameter. These measurements have the advantage that they directly probe the normalised superfluid density, $\overline{\rho_s} = (\lambda(0)^2/\lambda(T)^2)$, which is a measure of the number of electrons in the superconducting state and contains information about the temperature-dependent superconducting gaps [29, 30, 166-169]. In this work high resolution scanning Hall probe microscopy was used to measure the local temperature-dependent magnetic penetration depth, $\lambda(T)$, by imaging well-isolated single vortices in high quality single crystals of $SrFe_{2-x}Co_xAs_2$, and $BaFe_{2-x}Co_xAs_2$ samples with different doping levels. A multiple gap fitting procedure was then used to model the superfluid density, yielding insights into the number and structure of superconducting gaps at the Fermi surface.

Fe-based superconductors initially appeared well suited for high current applications as they display high critical magnetic fields with relatively low crystalline anisotropy, and the suggested s± order parameter should favour strong current flow across grain boundaries, in contrast to the situation in d-wave HTSCs. Empirically, however the pnictides have been shown to suffer from intrinsically low critical currents [170-172] and huge magnetic relaxation [171], and there is growing evidence that grain boundaries again represent weak channelling planes for vortices. In addition, nearly all imaging experiments have shown a highly disordered vortex lattice in single crystal samples. Recently, however, it has been shown that the introduction of columnar defects via heavy ion irradiation can considerably enhance, j_c, and strongly suppress vortex creep rates [170, 173]. Hence, a better understanding of vortex matter and pinning

potentials in these materials could yet prove important to enable future high current applications.

5.2. Sample preparation

High quality single crystal samples have been studied of Co-doped 122-$SrFe_{2-x}Co_xAs_2$ prepared by Sebastian's group in University of Cambridge using the flux growth technique[78, 174] and $BaFe_{2x}Co_xAs_2$ samples prepared by Tamegai's group in The University of Tokyo using the self-flux method. Several Ba-122 crystals had been grown with different Co compositions across the superconducting dome; underdoped (UD) with x =0.045; optimally doped (OptD) with x = 0.075; and overdoped (OD) with x=0.113 [175]. Experimental problems associated with the surface topography and sample inhomogeneity of the underdoped (UD) sample, may explain why no useful results were obtained for this the aprticular crystal.

The $SrFe_{2-x}Co_xAs_2$ (x~0.11) sample studied in this work was a high quality single crystal grown by the flux growth technique [78, 174] using starting elements of greater than 99.99% purity and an Fe:As:Sn flux. The sample had dimensions ~ 5mmx5mmx0.1mm, as shown in figure 46. The sample was glued on a piece of alumina sheet and then cleaved with scotch tape. After cleaving, a shiny and smooth sample surface was obtained.

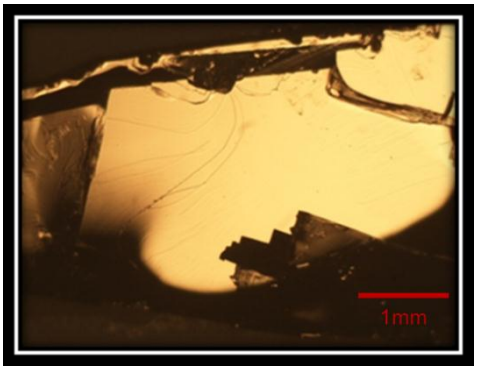

Figure 46: Optical micrograph of the Co-doped $SrFe_2As_2$ single crystal sample after cleaving.

The $Ba(Fe_{1-x}Co_x)_2As_2$ single crystal samples had different Co doping levels that spanned the superconducting 'dome' (see figure 47) and were grown by the FeAs/CoAs self-flux method [175]. After cleaving, fairly shiny samples were obtained but with a fairly rough topography over a lengthscale of 10-100μm, especially the underdoped sample, shown in figure 48. The typical dimensions of crystals were $4x4x0.1mm^3$ and the Co concentrations were determined by energy dispersive X-ray spectroscopy measurements [175].

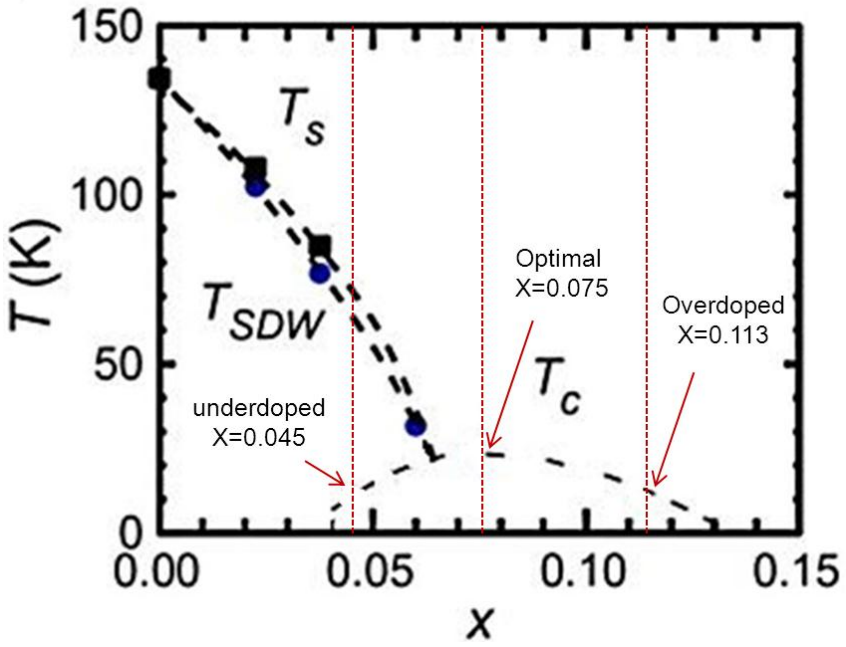

Figure 47: The phase diagram for $Ba(Fe_{1-x}Co_x)_2As_2$. and the location of samples studied in this work[175].

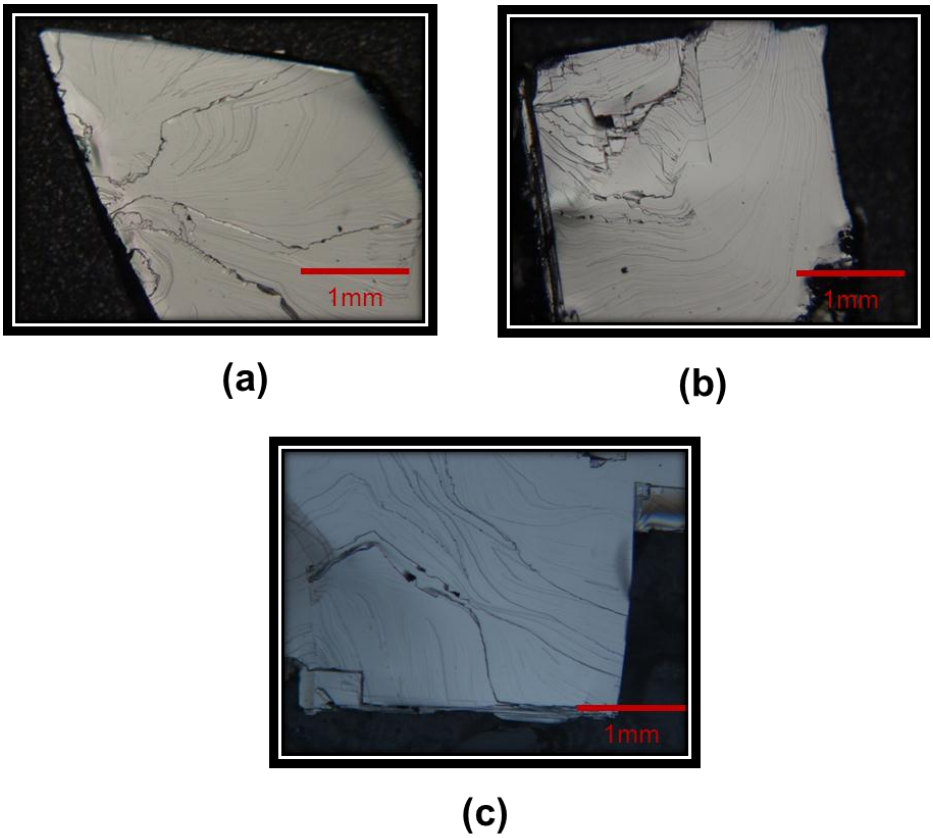

Figure 48: Optical micrographs of the Co-doped $BaFe_2As_2$ single crystal samples with different doping concentrations after cleaving: (a) underdoped (x=0.045), (b) optimum doped (x=0.075) and (c) overdoped (x=0.113).

5.3. Experimental set-up

High resolution scanning Hall probe microscopy (SHPM) was used to perform local magnetic imaging of 122-pnictide samples. As described in chapters 3 and 4, SHPM is a non-invasive magnetic imaging technique whereby a sub-micron Hall effect sensor is scanned just above the surface of the sample to be imaged in order to generate two-dimensional maps of the local magnetic induction. The sub-micron (0.8 μm) Hall probe was microfabricated in a GaAs/AlGaAs heterostructure chip by electron beam lithography and wet chemical etching. The Hall probe was defined approximately 5 μm from the corner of a deep mesa etch, which was coated with a thin Au layer to act as an integrated STM tip. The sample sits on an inertial motor and is first approached towards the sensor until tunnelling is established and then retracted about 100-200 nm allowing for

rapid scanning. The Hall probe makes an angle of about 1° with the sample plane so that the STM tip is always the closest point to the surface, and each 2D map of the magnetic induction is usually divided into 128×128 pixels. If required, several images (~10) can be averaged frame-by-frame to suppress low frequency noise arising from the Hall sensor. A more detailed description of the instrument and scanning technique is given in chapters 3 and 4 [176].

5.4. Results of $SrFe_2As_2$ sample

Figure 49 shows a typical set of 'local' magnetisation loops ($\mu_o M_l = B_z - \mu_o H_z$) of the $SrFe_2As_2$ sample at different temperatures below and above critical temperature. These magnetisation loops were captured by parking the Hall sensor a few hundred nanometres above the surface of the crystal and sweeping the applied magnetic field around a minor hysteresis loop between H=±70 Oe. The height of this loop, ΔM, averaged at H_z=+/-30Oe is a convenient measure of the diamagnetic screening (critical current) and is plotted in figure 50 as a function of temperature. It is seen that ΔM falls steeply towards zero at high temperature and a linear extrapolation of these data yields T_c=13.65±0.05K. The data show a small tail extending up to about 15K, as shown in figure 50. This could be due to residual diamagnetism in the normal state or may arise from weak sample inhomogeneity and the existence of small regions with a slightly higher critical temperature [177].

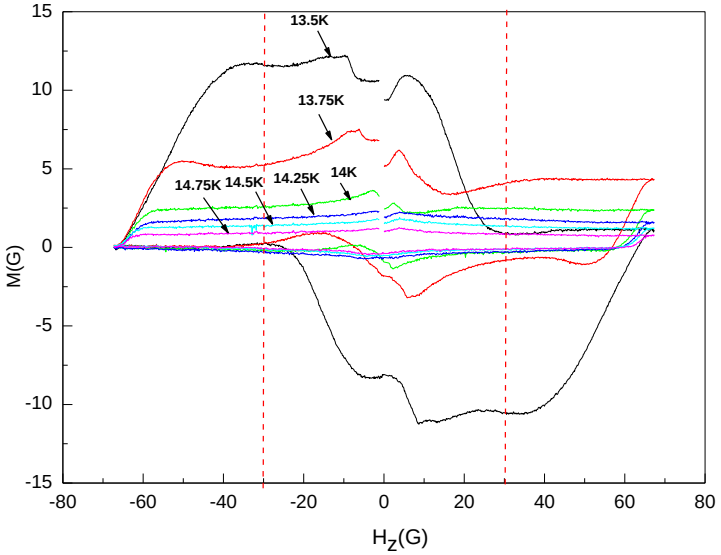

Figure 49: Sets of minor M_l-H_z hysteresis loops captured at different temperatures (see text).

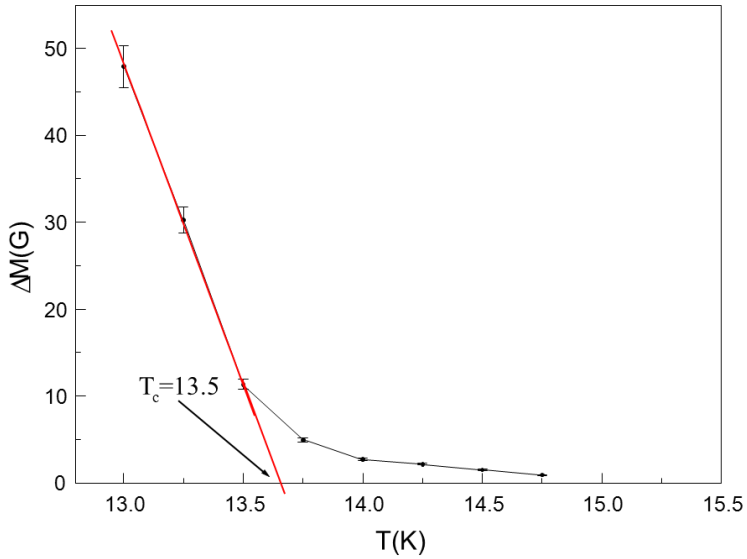

Figure 50: Maximum diamagnetic signal estimated from 'local' magnetisation measurements as a function of temperature (see text).

Figure 51 illustrates vortex-resolved SHPM images of the $SrFe_2As_2$ single crystal after field-cooling to T=8K from the normal state (T>15K) in small perpendicular applied magnetic fields between -4G and +7G. The scan area is ~8μm×8μm and varies a little with temperature due to the temperature-dependence of the piezoelectric tube. About three vortices per Gauss were expected on average in the absence of any diamagnetic screening. In practice, although changes in the number and sign of vortices as a function of field are qualitatively what one would expect, the actual number of vortices seen is considerably less than this estimate indicating quite strong magnetic screening. In addition, the true magnetic field zero is offset by about ~+1.3G due to the earth's field as well as stray fields from nearby ferrous materials.

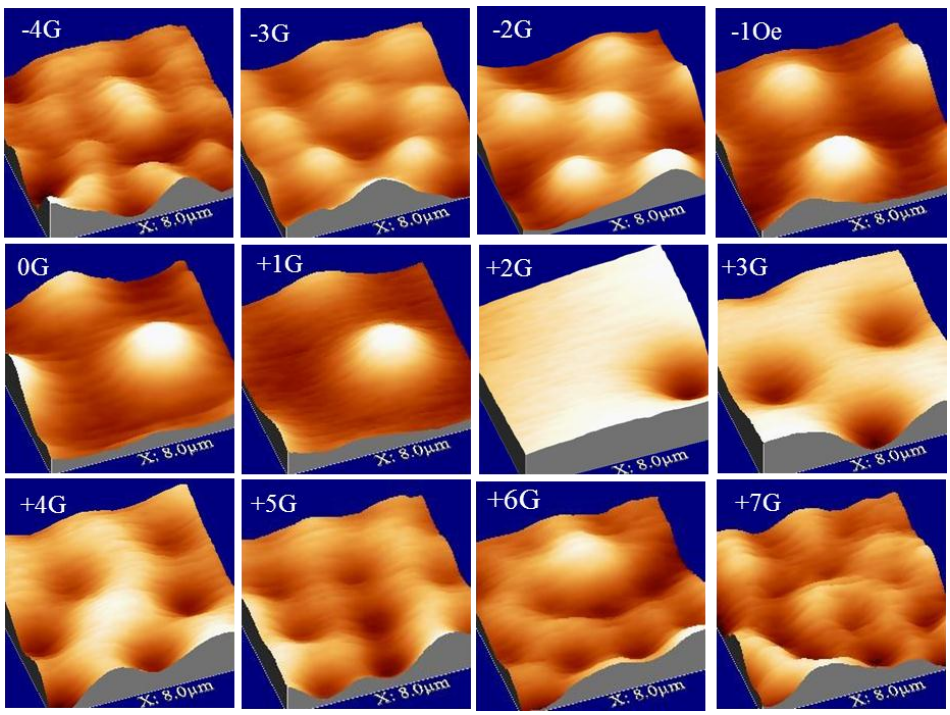

Figure 51: Three dimensional scanning Hall probe microscopy images of vortices in a Co-doped $SrFe_2As_2$ single crystal after field-cooling from above T_c to T=8K in various applied magnetic fields. Scan size ~8μm×8μm.

In order to measure the penetration depth, $\lambda(T)$, the sample was field-cooled in H_z=+1G from above T_c generating one well-isolated vortex as illustrated in figure 52. The first image was captured at T=5K, and the temperature then raised and the sample re-imaged at a number of temperatures up to T_c. During this process, it was crucial to capture all the images at the same scan height at each new temperature and to account for the temperature-dependent scan range of the piezoelectric scanner tube. Figure 53 illustrates a quantitative comparison between the measured vortex profiles and a modified variational vortex model due to Clem given by [35]:

$$B_j = \frac{1}{w^2}\int_{y-\frac{w}{2}}^{y+\frac{w}{2}}\int_{x-\frac{w}{2}}^{x+\frac{w}{2}}\frac{\phi_0}{2\pi\lambda}\int_0^s\left(\frac{\left(\sqrt{q^2+\lambda^{-2}}\right)}{\left(\sqrt{q^2+\lambda^{-2}}+q\right)}\right)\frac{K_1\left(\sqrt{q^2+\lambda^{-2}}\xi_v\right)\exp(-qz)J_0\left(q\sqrt{x'^2+y'^2}\right)qdqdx'dxy'}{\left(\sqrt{q^2+\lambda^{-2}}\right)\lambda K_1\left(\frac{\xi_v}{\lambda}\right)}, \quad (5.1)$$

where $\xi_v(T) = 2.5nm/\left((1-T/T_c)\right)^{\frac{1}{2}}$ is a variational coherence length, $\lambda(T)$ is the penetration depth, z is the sensor scan height measured from the surface of the sample, ϕ_0 is the flux quantum and s is integration cut off. The first term in brackets inside the integral is a correction term proposed by Kirtley *et al.* [178] that accounts for screening at the surface of the sample. With two fit parameters, $\lambda(T)$ and z, the agreement between the model and experimental data is excellent, as illustrated in figure 53 at four different characteristic temperatures for $\lambda(0)$=315nm [35] and z=1.81μm. The fitted scan height is somewhat larger than would generally be expected and probably reflects the fact that the sensor tilt angle is somewhat greater than 1^o in these measurements. However, the excellent fit quality allows the extraction of values of the penetration depth, $\lambda(T)$, at different temperatures and of $\Delta\lambda(T) = \lambda(T) - \lambda(0)$ is plotted in figure 54.

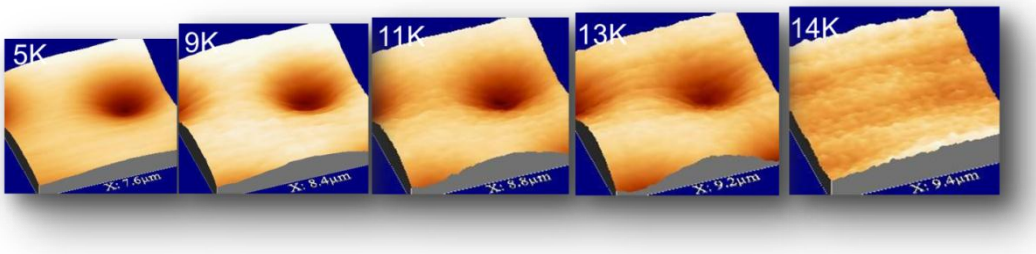

Figure 52: Three dimensional scanning Hall probe images of a single vortex at various temperatures in a single crystal Co-doped (~10%) $SrFe_2As_2$ sample after field-cooling at H=+1Oe. (Note that the scan range becomes smaller at low temperature due to a small reduction of the piezoelectric coefficient of the scanner tube).

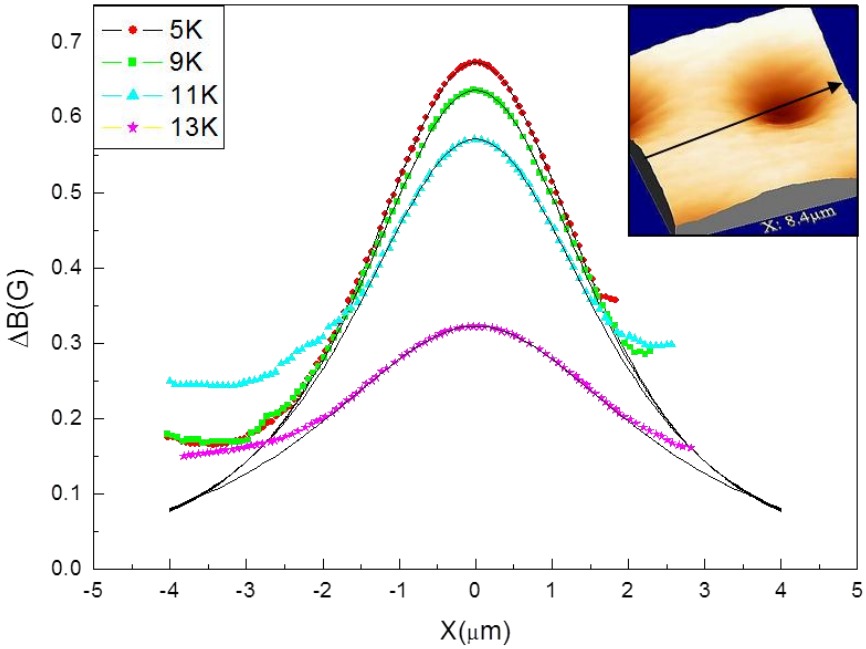

Figure 53: Magnetic field profiles across a single vortex after field-cooling in H_z=+1Oe to the indicated target temperature. The points are experimental data and solid lines are fits to a modified variational model due to Clem. The insert shows how the linescan was constructed across the raw vortex image at T=9K.

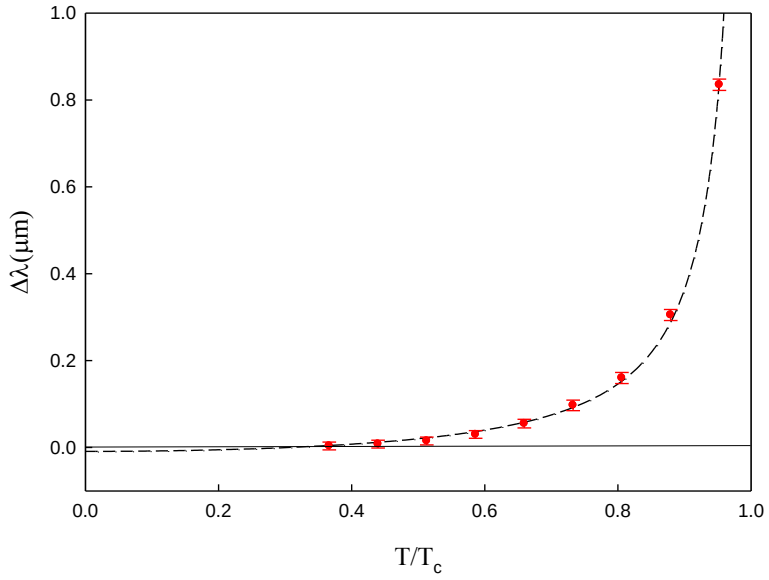

Figure 54: $\boldsymbol{\Delta\lambda(T) = \lambda(T) - \lambda(0)}$ extracted from the fits as a function of temperature.

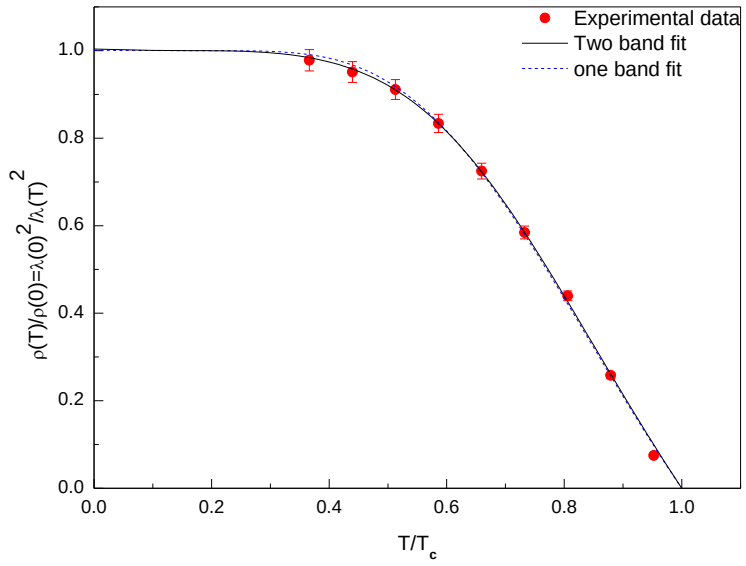

Figure 55: Experimentally estimated temperature-dependent superfluid density, $\boldsymbol{\rho_s(T)}$ (points), and the results of a two band $\boldsymbol{\alpha}$-model (solid line), where $\boldsymbol{p}$=0.49 $\boldsymbol{a_1}$=0.94 ($\boldsymbol{a_2}$=1, Δ_1=4.8kT$_c$, Δ_2=2.0kT$_c$) and the results of a one band model (dashed line) where $\boldsymbol{a}$=0.92, Δ =2.81kT_c (see text).

Following a procedure described by Luan [35, 179] to model MFM data on $Ba(Fe_{0.95}Co_{0.05})_2As_2$ single crystals, the results for penetration depth figure 54 were used to calculate the superfluid density, $\rho_s(T)/\rho_s(0) = \lambda(0)^2/\lambda(T)^2$, which was subsequently fitted to a two band α-model [179, 180] with two full gaps. This model assumes that $\rho_s(T) = p\rho_1(T) + (1-p)\rho_2(T)$, where $\rho_{1,2}(T)$ are the superfluid densities in the two different bands and p is the relative contribution from band 1. The individual superfluid densities have been calculated assuming the following expression for isotropic s-wave pairing [30]

$$\rho_i(T) = 1 - \frac{1}{2kT}\int_0^\infty cosh^{-2}\left(\frac{\sqrt{\varepsilon^2+\Delta_i(T)^2}}{2kT}\right)d\varepsilon, \qquad (5.2)$$

where the gap was assumed to be given by

$$\Delta_i(T) = \Delta_i(0)tanh\left[\frac{\pi kT_c}{\Delta_i(0)}\sqrt{a_i\left(\frac{T_c}{T}-1\right)}\right]. \qquad (5.3)$$

Here a_i is a characteristic parameter that reflects the specific pairing state (e.g., a_i=1 for isotropic s-wave pairing, a_i=4/3 for two-dimensional d-wave, a_i= 2 for s+g-wave and a_i= 0.38 for nonmonotonic d-wave) [30]. Figure 55 illustrates the experimentally measured temperature dependence of the superfluid density (points with error bars) along with fits to a two-band α -model (solid line) with Δ_1=4.8kT_c, Δ_2=2.0kT_c, p=0.49 for Δ_1 , and a_1=0.94, a_2=1. The gap values for the two bands were taken from the results of point contact spectroscopy [35], a_2 was assumed to be unity, and the values of a_1 and p were extracted from an automated fitting routine. Figure 55 also shows the result of a one band fit (dashed line) with a=0.92 and Δ=2.81kT_c for comparison.

The choice of $\lambda(0)$ has a very large effect on the calculation of the values of superfluid density. Hence, the interdependence of $\lambda(0)$ and z were investigated by allowing $\lambda(0)$ to vary by +/-50nm around the accepted literature value and fitting to find z at the lowest temperature reached. It was found that z varied by -/+50nm about the value used to fit the data

here. Fortunately, any error introduced by the choice of $\lambda(0)$ was cancelled to a significant degree when the ratio was plotted as $\lambda(0)^2/\lambda(T)^2$, and the parameter a_1 is somewhat insensitive to it. Figure 56 shows the superfluid density curves for several different values of $\lambda(0)$, representing a realistic assessment of the uncertainty for this parameter.

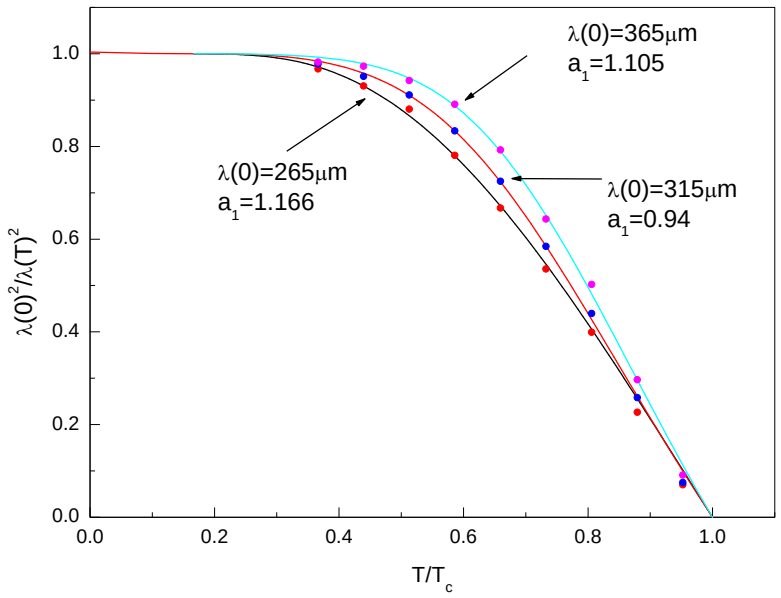

Figure 56: The influence of the choice of $\boldsymbol{\lambda(0)}$ on the calculated superfluid density and the value of fit parameter $\boldsymbol{a}$.

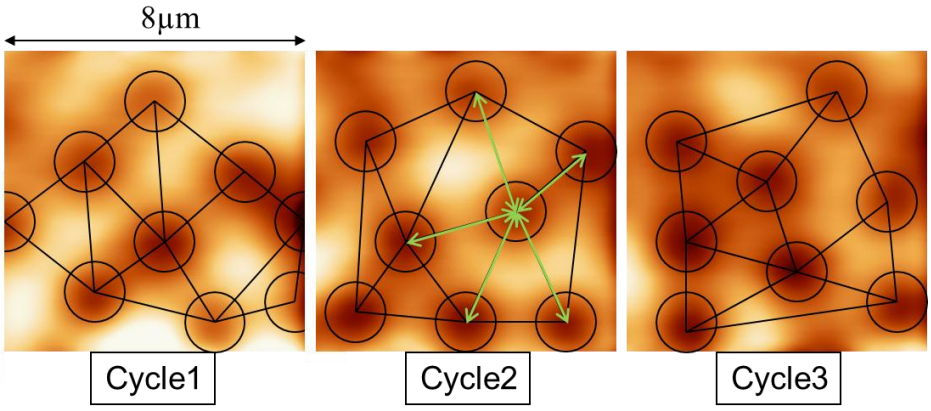

Figure 57: Vortex images captured after repeatedly field-cooling the sample from above T_c to T=8K in an applied magnetic field, H_z=+5 G.

Finally, figure 57 shows the results of an investigation of the microscopic vortex pinning landscape in the Co-doped $SrFe_2As_2$ single crystal whereby images captured after repeated field-cooling from above T_c to T=8K in the same applied field of H_z=+5G have been compared. Here, images captured after three successive cooling cycles are shown and it is noted that, although each image contains approximately the same number of vortices, the local vortex structure (as illustrated by the superimposed net) is qualitatively different in each case. This suggests that the stabilisation of vortex structures in the presence of quite a high density of microscopic pinning sites leads to a different structural realisation each time.

5.5. Discussion of $SrFe_2As_2$ sample

Figure 55 shows that the fitting of the two-gap model is slightly better than the one-gap model especially at low temperatures and has a 3% lower root mean square (RMS) error, although the difference is clearly quite small. It is generally assumed that the smaller gap is situated on the hole pockets at the Γ-point, and it can be seen that in this case the superfluid density appears to be fairly equally shared between these hole pockets and the electron pockets at the M-points. The hole gap is generally expected to be isotropic s-wave (a_2=1), and the fitted value of a_1=0.94 is rather close to unity within experimental errors indicating that there is an approximately isotropic s-wave order parameter at the electron pockets with no clear evidence for nodes. However, this conclusion needs to be examined more critically since it was found that the temperature dependence of the fitted penetration depth is quite sensitive to the value of $\lambda(0)$ used as an input parameter to calibrate the scan height, z, at low temperatures. To explore this point further, the same fitting routine described above was repeated for $\lambda(0)$=315+50nm and $\lambda(0)$=315-50nm. Whilst it was found that the fitted weighting of superfluid density, p, for the two bands does depend quite sensitively on this choice, the fit parameter a_1 is rather insensitive to it, as shown in figure 56. Hence it is concluded

with some confidence that the electron pockets are indeed behaving with something close to an isotropic s-wave order parameter.

The disordered vortex structures observed in figure 57 were expected due to the direct substitution (doping) of Fe with Co in the superconducting planes of this sample. The deviation of the vortex structure from an ideal triangular lattice (Abrikosov lattice) is a measure of the local pinning force and it is interesting to compare this with values inferred from critical currents measured by other means. In practice, it was assumed that the force per unit length between a pair of vortices can be calculated from equation 5.4 [37]

$$\vec{f}^{v-v}(r) = \frac{2\phi_0^2}{4\pi\mu_0\lambda^3} K_1\left(\frac{r}{\lambda}\right)\hat{r} \cong \frac{2\phi_0^2}{4\pi\mu_0\lambda^3}\sqrt{\frac{\pi\lambda}{2r}}\, exp\left(-\frac{r}{\lambda}\right)\hat{r}, \qquad (5.4)$$

where, r is the separation between the vortices, $\hat{r}$ is a unit vector along the line joining the two vortex cores and $K_1(x)$ is a modified Bessel function of the second kind. The vortex-vortex distances (green arrows) from images like those in cycle 2 of figure 57 were estimated and the net force on a centrally positioned vortex due to its nearest neighbour vortices was calculated. This resultant force is typically in the range $f_p \sim 2 - 10 \times 10^{-9}$N/m, and represents a measure of the low field pinning force in the crystals. Using the relationship $j_c \approx f_p/\phi_0$ this translates into a critical current density in the range 1-5×10^2 A/cm^2, considerably smaller than other values estimated from high field magnetisation studies (e.g., j_c~2.6×10^5 A/cm^2 as estimated for $Ba(Fe_{0.93}Co_{0.07})_2As_2$ by a range of independent techniques at 5K [171]). Given the very large vortex-vortex spacings in the images they do not really explore the full pinning landscape in our samples, and this large discrepancy is not surprising. Moreover, isothermal magnetisation measurements on Co-doped 122 single crystals are known to exhibit a non-monotonic fishtail shape and, on the basis of magnetic relaxation measurements, have been shown to be consistent with collective pinning and creep models with a crossover to a plastic creep regime at fields above the position of the maximum in the

fishtail magnetisation[171]. Hence, it was fully expected that the measured low field pinning force would be significantly smaller than higher field measurements, where collective pinning effects becomes important.

5.6. Vortex structures in Co-doped $BaFe_2As_2$ samples with different doping level.

Figure 58 and 59 show typical magnetization loops for $Ba(Fe_{0.93}Co_{0.07})_2As_2$ and $Ba(Fe_{0.89}Co_{0.11})_2As_2$ single crystals at different temperatures below T_c. These results were captured by parking the Hall sensor a few hundred nanometres above the surface of the crystal and sweeping the applied magnetic field around a minor hysteresis loop between H=±70 G. The height of this loop, ΔM, averaged at H_z=+/-25G is a measure of the diamagnetic screening and is plotted in the main graph in figure 58 and 59 as a function of temperature. The diamagnetic signal above the critical temperature of both samples is probably due to weak diamagnetism in the normal state. Figure 58 shows the estimated value of the critical temperature Tc=23.3±0.05K of the $Ba(Fe_{0.93}Co_{0.07})_2As_2$ single crystal, which has been inferred from the intercept of the linear extrapolation of the ΔM with temperature. Figure 59 shows comparable data yielding the critical temperature T_c =9.62±0.05K of the $Ba(Fe_{0.89}Co_{0.11})_2As_2$ single crystal.

Figure 60 shows a set of vortex-resolved SHPM images of a $Ba(Fe_{0.93}Co_{0.07})_2As_2$ single crystal after field-cooling to T=12K from the normal state (T>25K) in small perpendicular applied magnetic fields between -6G and +2G. The applied field is in addition to the earth's field ~ -2G including stray fields from nearby ferrous materials.

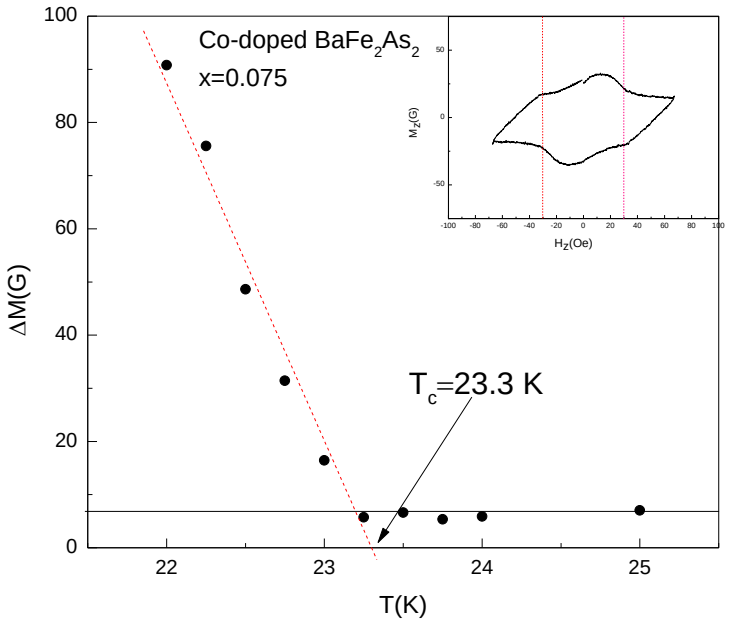

Figure 58: Diamagnetic signal estimated from 'local' magnetization measurements as a function of the temperature in the $Ba(Fe_{0.93}Co_{0.07})_2As_2$ single crystal. The inset shows a typical M_l–H_z hysteresis loop captured at T =22.75 K.

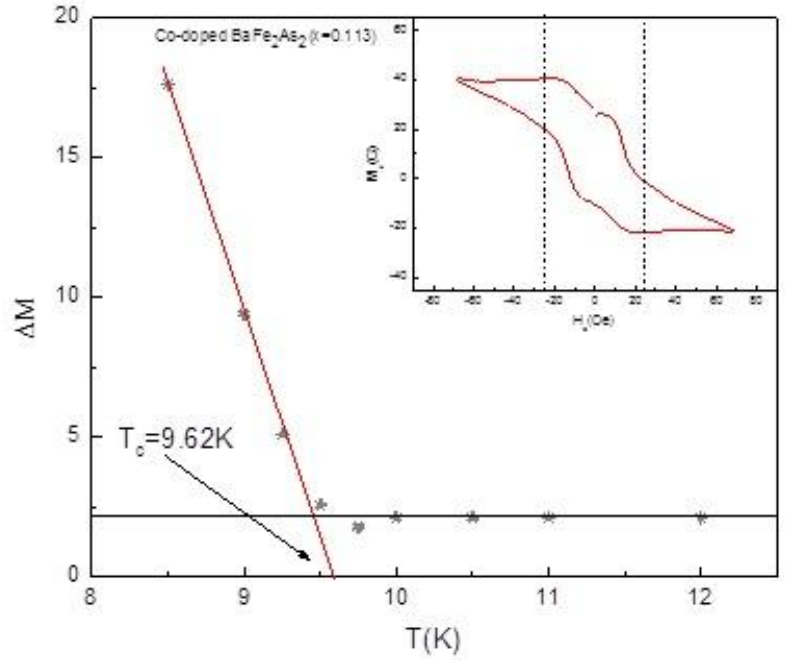

Figure 59: Diamagnetic signal estimated from 'local' magnetization measurements as a function of temperature in the $Ba(Fe_{0.89}Co_{0.11})_2As_2$ single crystal. The inset shows a typical hysteresis loop captured at T =8.5 K.

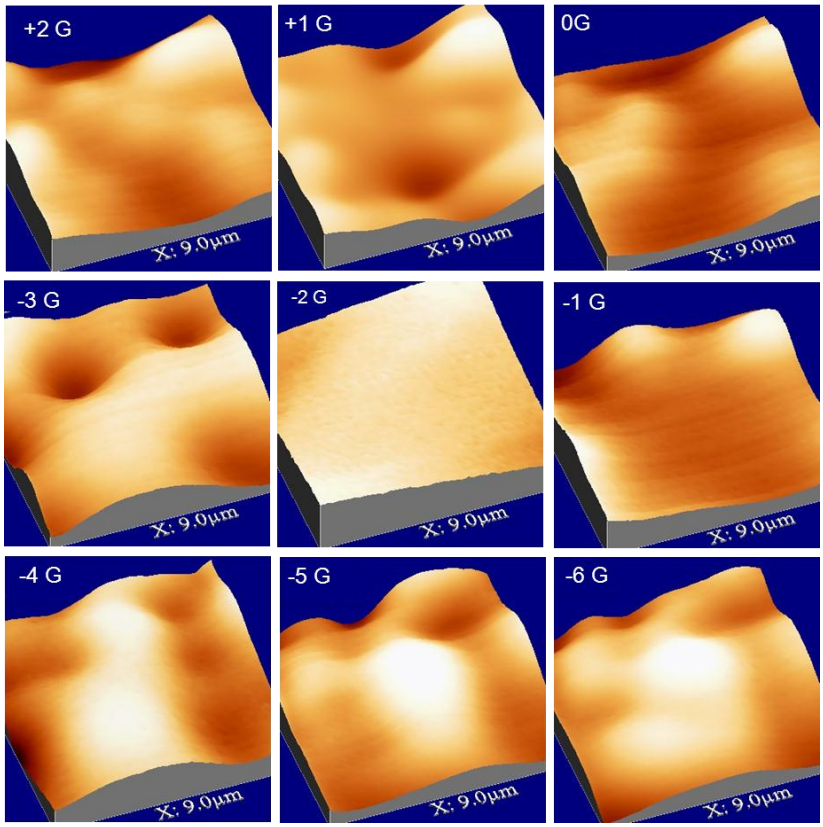

Figure 60: Three dimensional scanning Hall probe microscopy images of vortices in a $Ba(Fe_{0.93}Co_{0.07})_2As_2$ single crystal after field-cooling from above T_c to T=12K in various applied magnetic fields. The scan size is ~9µm×9µm.

Figure 61 shows comparable vortex images captured on a $Ba(Fe_{0.89}Co_{0.11})_2As_2$ single crystal after field-cooling to T=6K from the normal state (T>12K) in small perpendicular applied magnetic fields between -5G and +5G. The applied field is in addition to ~ +2G of earth's field including stray fields from nearby ferrous materials. At 6K the temperature-dependent scan range of the piezoelectric tube is ~7.84µm×3.8µm, the small scan area being required due to the complex topography of the sample.

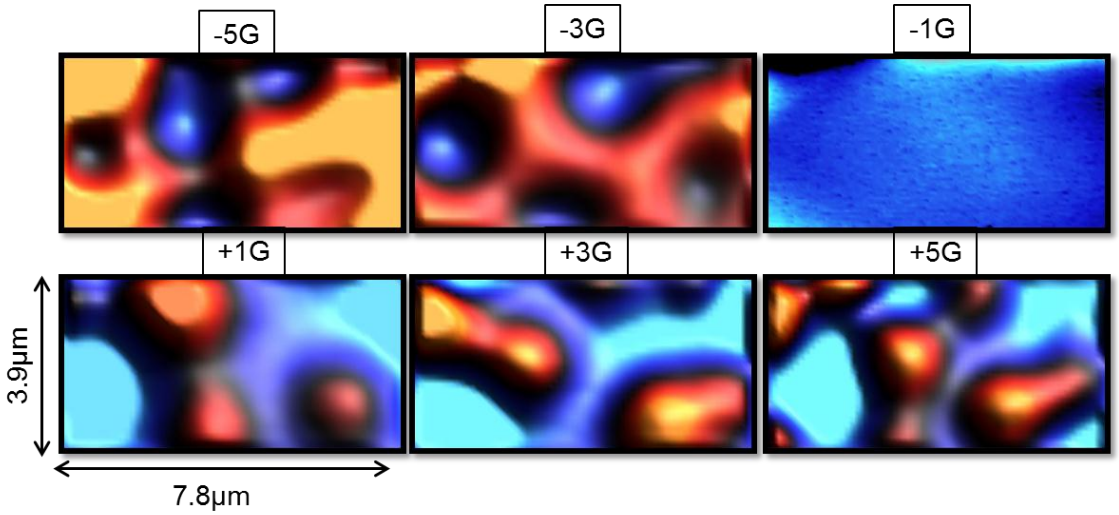

Figure 61: SHPM images of the Co-doped $Ba(Fe_{0.89}Co_{0.11})_2As_2$ single crystal after field-cooling from above T_c to T=6K in various applied magnetic fields (+5G to -5G). The scan size is ~ 7.8μm×3.9μm.

Calculation of the superfluid density in the pnictide superconductor $Ba(Fe_{1-x}Co_x)_2As_2$ across the superconducting dome.

The normalised temperature dependence of the superfluid density, $\overline{\rho_s}(T)$, of Co-doped $BaFe_{2x}Co_xAs_2$ single crystal samples has been probed at different x-concentrations across the superconducting 'dome'; optimally doped (OptD) x = 0.075, overdoped (OD) x = 0.113; [175]. Such investigations could shed light on the pairing mechanism in the family of iron-pnictide superconductors [181].

The temperature-dependent magnetic penetration depth, $\lambda(T)$, in $BaFe_{2x}Co_xAs_2$ (OptD x = 0.07) was extracted by fitting the magnetic profile of a well-isolated single vortex after field cooling at H=+1G at different temperatures up to T_c. A variational model due to Clem with a modification suggested by Kirtley *et al.* [93, 159] was used to fit the data assuming $\lambda(0)$=0.250 μm [181], with $\xi_v = 2.5\text{nm}/\sqrt{1-T/T_c}$, an active Hall probe width, w, of 800nm and z = 2.295μm as a fit parameter. The temperature-dependent normalised superfluid density, $\rho_s(T)/\rho_s(0) = \lambda(0)^2/\lambda(T)^2$, was calculated using the extracted values of penetration depth. These data were then fitted to a two band α-model with two full gaps. This model

assumes that $\rho_s(T) = p\rho_1(T) + (1-p)\rho_2(T)$, where $\rho_{1,2}(T)$ are the superfluid densities in the two different bands and p takes into account the relative contribution from each. The individual superfluid densities were calculated from equations (5.3), (5.4) for isotropic s-wave pairing[63] where a_i is a characteristic parameter that reflects the specific pairing state. Figure 62 (a) shows the extracted values of $\lambda(T)$ for the $BaFe_{2-x}Co_xAs_2$ (OptD x = 0.075) sample and figure 62(b) shows the calculated superfluid density for the same sample and fits to two gap α-model with parameters Δ_1=3.3kT$_c$, Δ_2=1.3kT$_c$ [181], p=0.614 for Δ_1, and a_1=0.236, a_2=1 [30], as well as the results of a one band model fitting (dashed line) with a=0.998, Δ =1.92kT_c .

Figure 63 (a,b) shows comparable data for the temperature dependence of the superfluid density for the $BaFe_{2x}CoxAs_2$ (OverD x= 0.113) sample, which was calculated by fitting $\Delta\lambda(T) = \lambda(T) - \lambda(0)$ on awell-isolated vortex at H=-1.5Oe where $\lambda(0)$=0.2752 μm [181], and z=1.547. The two gap α-model has been fitted to the data with Δ_1=4.25kT$_c$, Δ_2=1.92kT$_c$ [182], p=0.708, a_1=0.293 and a_2=1[30], as well as a one band model (dashed line) with a=0.996, Δ =1.43kT_c .

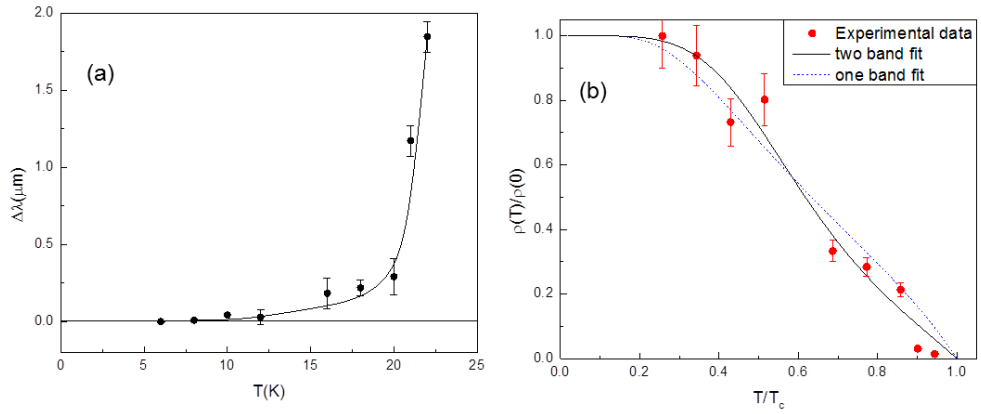

Figure 62:(a) $\boldsymbol{\Delta\lambda(T) = \lambda(T) - \lambda(0)}$ extracted from fits on the $BaFe_{2-x}Co_xAs_2$ (Opt. D x= 0.075) sample, (b) red points show the experimental dependence of the normalised superfluid density on the temperature. The black solid line is a fit to a two-band $\boldsymbol{\alpha}$-model with Δ_1=3.3kT$_c$, Δ_2=1.3kT$_c$, $\boldsymbol{p}$=0.614, and $\boldsymbol{a}_1$=0.236, $\boldsymbol{a}_2$=1. The dashed line is a fit to a one band model with $\boldsymbol{a}$= 0.998 with Δ =1.29kT$_c$.

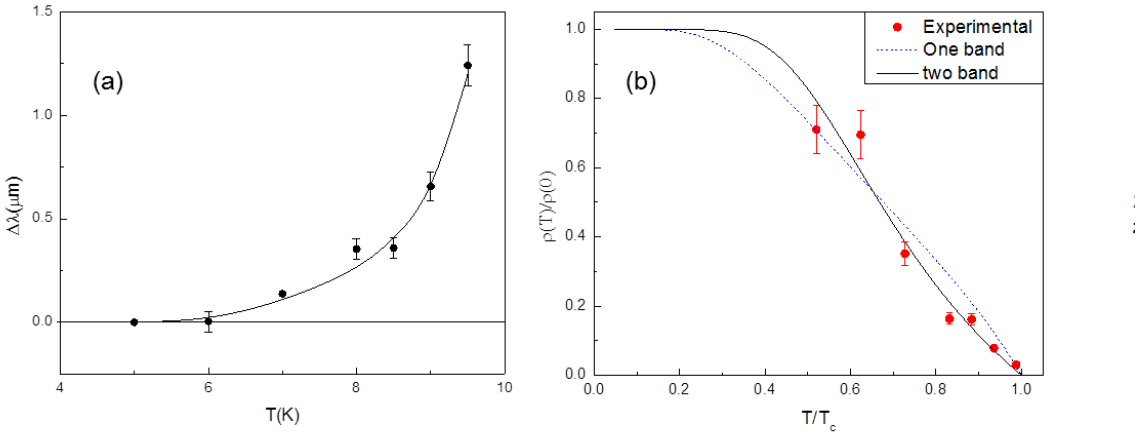

Figure 63:(a) $\boldsymbol{\Delta\lambda(T) = \lambda(T) - \lambda(T_c/2)}$ extracted from fits on the $BaFe_{2x}Co_xAs_2$ (OverD x= 0.113) sample, (b) red points show the experimental dependence of the normalised superfluid density on the temperature. The black solid line is a fit to a two-band $\boldsymbol{\alpha}$-model with Δ_1=4.25kT_c, Δ_2=1.95kT_c, $\boldsymbol{p}$=0.708, and $\boldsymbol{a}_1$=0.293, $\boldsymbol{a}_2$=1. The dashed line is a fit to a one band model with a= 0.996 with Δ =1.43kT_c.

5.7. Discussion of $BaFe_2As_2$ samples

Figures 62 and 63 show that the two-gap model is a much better fit to $\bar{\rho}_s(T)$ than the one-gap model and has a ≈8% lower RMS error, although the error bars are quite large. The fitted values of a_1=0.236 for $BaFe_{2-x}CoxAs_2$ (Opt. x= 0.075) and a_1=0.293 for $BaFe_{2-x}CoxAs_2$ (OverD x= 0.113) would tend to implicate non-monotonic d-wave symmetry for the superconductivity gap symmetry with 45° nodes characteristic of the d-wave order parameter [30]. However, these results contradict other results in electron-doped pnictides which give evidence for s± wave pairing [35, 182-184]. However some recent reports literatures suggest that the pairing symmetry in the $BaFe_2As_2$ compound undergoes a transition from s to d symmetry with potassium doping up to the fully doped KFe_2As_2 compound which has been identified as a d-wave superconductor[185, 186].

5.8. Conclusions

The temperature dependent magnetic profiles of a single vortex in a single crystal of the $SrFe_{2-x}Co_xAs$ (x=0.11) Fe-pnictide superconductor have

been fitted to extract the temperature dependence of the superfluid density. Fits to this data agree well with a two band α-model containing two full gaps. Moreover, the fit parameters suggest that the superfluid density is shared almost equally between hole and electron pockets and that the larger (electron pocket) gap appears to have an approximately isotropic s-wave order parameter. The superfluid density of $BaFe_{2-x}Co_xAs$ crystals (x=0.075 and 0.113) also fits well to a two band α-model with two full gaps, but the fitting parameters suggest that there is non-monotonic d-wave gap with nodes at the Fermi surface.

Finally, the deviation of vortex structures from an ideal triangular lattice has been used to calculate typical pinning forces at low magnetic fields. These can be converted to typical values of the critical current that are several orders of magnitude smaller than those estimated by other means for similar superconducting crystals and highlight the importance of collective pinning effects at high fields.

Chapter six: Experimental Results; Epitaxial MgB_2 thin films

6.1 Introduction

MgB_2 has attracted both theoretical and experimental attention since it was discovered to be a superconductor in 2001, due to its unusually high superconducting transition temperature, T_c=39K[10] for a binary intermetallic compound and its two-band superconductivity. The latter was conjectured theoretically soon after BCS theory was put forward [21], but had not been identified in a real materials system.

Recent experiments that probe the superconducting gap of MgB_2, such as tunnelling spectroscopy [187, 188], point-contact spectroscopy [104, 189], Raman scattering [105], and specific heat measurements [111, 190] provide strong evidence for two energy gaps with *s*-wave symmetry order parameters. In addition to the above measurements, the temperature dependence of the magnetic penetration depth $\lambda(T)$ has been used as a sensitive probe of the superconducting gap structure. Such measurements have the advantage that they directly probe the number of electrons in the superconducting state via estimates of the normalised superfluid density, $\bar{\rho_s} = (\lambda(0)^2/\lambda(\mathrm{T})^2)$, which contains information about the excited quasiparticles and hence pairing symmetry and superconducting gaps [191-195].

Recently many researchers have focused on the studies of vortex matter in MgB_2 using different techniques such as Bitter decoration [101], as well as scanning SQUID [196], scanning Hall probe microscopy [197], and molecular dynamics simulations [108]. Theoretical studies suggest the possibility of type1.5 superconductivity when vortices experience a short-range repulsion and long range attraction. In this case vortex matter is expected to contain vortex “islands” and “labyrinths” and this is consistent with the experimental outcomes from investigations of nearest neighbour vortex-vortex distributions [101].

In the present work, a high resolution scanning Hall probe microscope has been used to infer the local temperature-dependent normalised superfluid density from the measured magnetic penetration depth, $\lambda(T)$, extracted from fits to the magnetic profiles of well-isolated single vortices in MgB_2 thin films. The superfluid density has then been fitted to a two band α-model to provide insights into the nature of superconducting gaps at the Fermi surface. In addition, the nearest neighbour distribution of vortex structures is investigated over a large area ($\approx 50\mu m^2$) at different magnetic fields to identify symmetry breaking in thin films of different thicknesses [35].

6.2 Experimental set-up

High resolution scanning Hall probe microscopy (SHPM) and mK-SHPM have been used to generate two-dimensional maps of the local magnetic induction in MgB_2 thin film samples using a sub-micron (0.8 μm) Hall probe [156, 176]. The sensor was microfabricated in a GaAs/AlGaAs heterostructure chip by electron beam lithography and wet chemical etching (c.f. the discussion of SHPM systems provided in chapter four). The MgB_2 films were grown by van Erven *et al.* using molecular-beam epitaxy at a growth rate of 2.3 Å/s, with a flux ratio (Mg:B) of 1.8 on a silicon (111) substrate which was held at $\approx 300^oC$ [198].

Figure 64 shows the sharp superconducting transition ($\Delta T \simeq 0.1K$) at $T_c \sim 35.85K$ exhibited by the temperature-dependent resistance. The Residual Resistance Ratio, RRR = R(300K)/R(40K), for the thin film (160nm), is 1.2, as compared to typical literature values in the range 3.5 to 25 for single crystals[199-202], and 2.5-33.3 for thin films [203, 204].

Using the Drude relation $\ell = 3/N(0)v_F e^2 \rho_0$, the mean free path can be estimated for thin films where v_F is an average Fermi velocity of $4.8 \times 10^5 ms^{-1}$ [205, 206], $N(0)$ is the density of states = 0.7 eV $^{-1}$ unit Cell^{-1} [34, 207] and ρ_0 is the residual resistivity where $\rho_0 = \rho(36K) = 15\mu\Omega cm$ (see figure 64). This analysis yields a value for the mean free path of $\ell = 11nm$ in 160nm thin film. This estimation is smaller than any discussed in the

literature which fall in the range $38 \leq \ell \leq 100\text{nm}$ [202, 208-212]. Moreover, the value for the RRR as well as the mean free path of our sample suggest that the films studied here are somewhat more disordered than any similar samples in the literature.

Vortices are well separated and easy to identify at 1.25G, 1.7G and 2.8G in the 160nm film and at 1.25G and 2.8G in the 77nm film. Due to the higher vortex density at 5G, they are relatively difficult to identify in the 160nm sample. In this case a self-consistency check was used to confirm the correct number of vortices based on the known flux in the scanned area of the sample at this applied field.

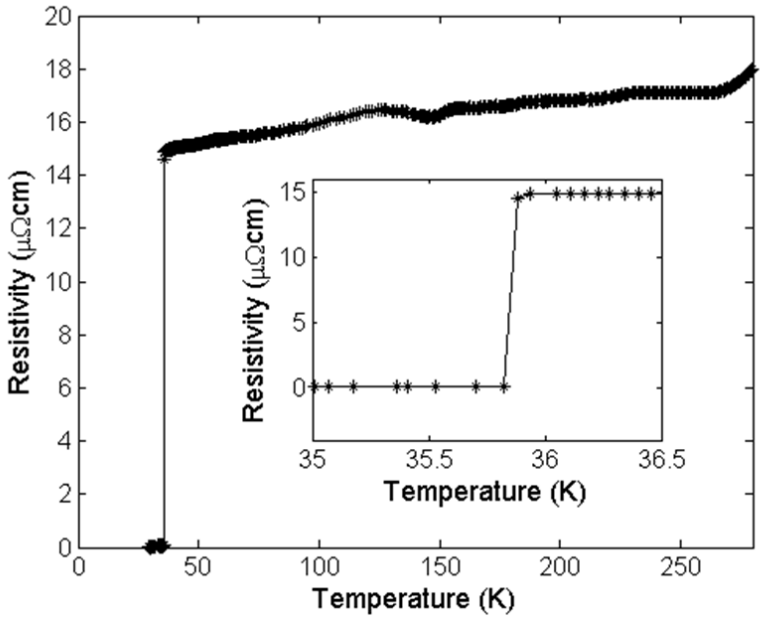

Figure 64: The temperature dependence of the resistance of the 160 nm MgB_2 thin film prepared by molecular-beam epitaxy. Insert shows an expanded view of the resistive transition.

6.3 MgB_2 results

Figure 65 shows typical SHPM images for the 160nm MgB_2 thin film after field-cooling to T=20K from the normal state (T>36K) in small perpendicular applied magnetic fields between -3G and +3G. In all case a scan size of ~10.7μm×10.7 μm is used. Note that this varies with temperature due to the temperature-dependent scan range of the piezoelectric tube.

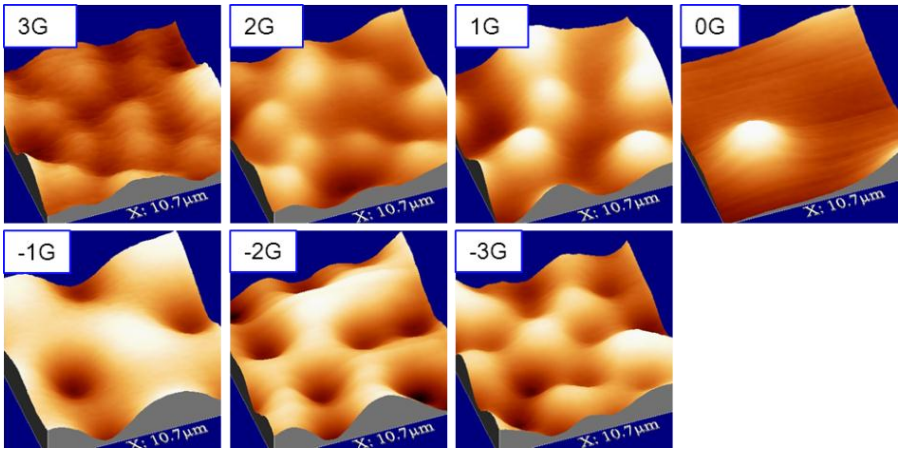

Figure 65: Three dimensional SHPM vortex images for a 160 nm MgB_2 film after field-cooling from above T_c to T=20K in various applied magnetic fields (-3G to +3G). Scan size ~10.7µm×10.7µm.

In order to measure the T-dependent penetration depth, the sample was field-cooled in H_z=+2.5G from above T_c to generate a single well-isolated vortex. As shown in Figure 66, the first image was captured at T=5K, then the temperature increased and the sample re-imaged in 2K temperature steps up to T_c. Great care was taken to keep the scan height the same at each temperature by approaching to tunnelling and lifting off a known fixed height. In addition, the temperature-dependent scan range of the piezoelectric scanner tube was carefully accounted for and vortex profiles were fitted to a theoretical model for the vertical component of the magnetic field near a vortex in a superconducting film given by [213]:

$$B(x,\lambda,B_o)=\frac{1}{w^2}\int_{\frac{-w}{2}}^{\frac{w}{2}}\int_{x-\frac{w}{2}}^{x+\frac{w}{2}}\frac{\phi_o}{2\pi\lambda^2}\int_0^s\frac{J_o\left(q\sqrt{x_1^2+y^2}\right)}{\sqrt{q^2+\lambda^{-2}}\left(coth\left(\sqrt{q^2+\lambda^{-2}}\frac{d}{2}\right)\right)+\frac{\sqrt{q^2+\lambda^{-2}}}{q}}exp(-qz)dqdx_1dy+B_o, \quad (6.1)$$

This theoretical model was developed for response of Hall probe for a magnetic flux smaller than the Hall probe geometrical size in the case of $\lambda \gg \xi$, where λ is the penetration depth, λ is coherence length, z is the sensor scan height measured from the surface of the sample, ϕ_o is the

flux quantum, w is the width of the active area of the Hall probe, d is thin film thickness, B_o accounts for the Hall probe voltage offset and s is integration cut off. As illustrated in figure 67, the agreement between our experimental data (magnetic profile) and the model is excellent using the two fit parameters, $\lambda(T)$ and z, assuming $\lambda(0)$=200nm [214] and z=1.563μm. Owing to the excellent fit quality, we are able extract values for the temperature-dependent penetration depth, $\lambda(T)$, at each measurement temperature and the values of $\Delta\lambda(T)= \lambda(T)-\lambda(0)$ obtained are plotted in figure 68.

These data were then used to calculate the normalised superfluid density $\rho_s(T)/\rho_s(0) = (\lambda(T)/\lambda(0))^2$ and fitted to a two band α-model [35, 179] with two full gaps (as described in chapter five using equations 5.5, 5.6). In MgB_2, the pairing state is believed to be isotropic s-wave and so the values of the characteristic parameter that reflect the specific pairing state are set to be a_1=a_2=1. Under this assumption, the values Δ_1=1.86±0.3 kT_c, Δ_2=0.52±0.1 kT_c and p=0.4 for band 1 were extracted from an automated fitting routine. These values for the energy gaps are fairly consistent with the values of the two gaps measured by point contact spectroscopy [211]. Figure 69 shows the temperature-dependent superfluid density and fits to the two-band α-model (solid line). In addition, figure 69 shows the result of fitting a one band model (dashed line) with a=0.998 and Δ=0.839kT_c for comparison. A quantitative comparison of the two fits reveals that the two-gap model is a somewhat better fit than the one-band model and has a 5% lower root mean square (RMS) error.

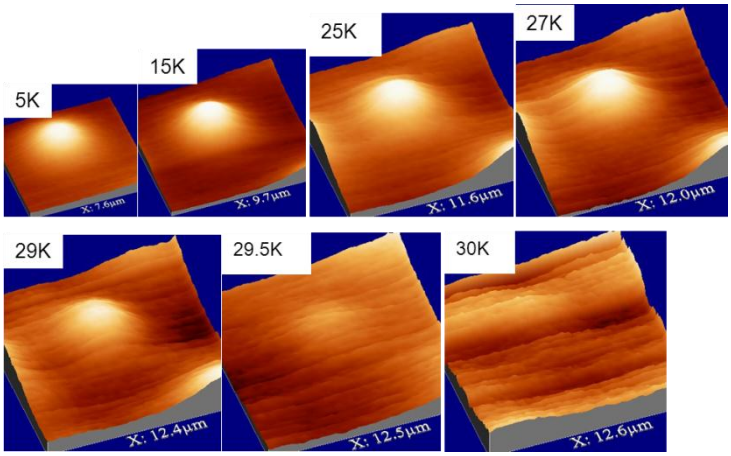

Figure 66: Three dimensional SHPM images of a single vortex after field-cooling at H=+2.5 G at various temperatures in a 160nm MgB_2 thin film.

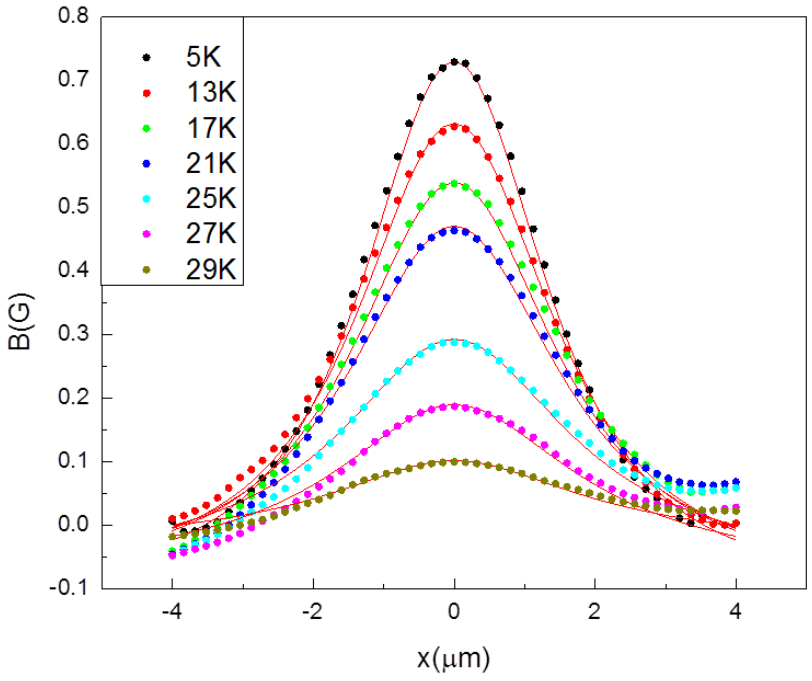

Figure 67: Magnetic field profiles across a single vortex in a 160nm MgB_2 thin film (points) after field-cooling in H_z=+2.5G at different temperatures. Solid lines show fits to a theoretical model (see text) data (solid lines).The insert shows the location of linescan across a vortex image at T=5K.

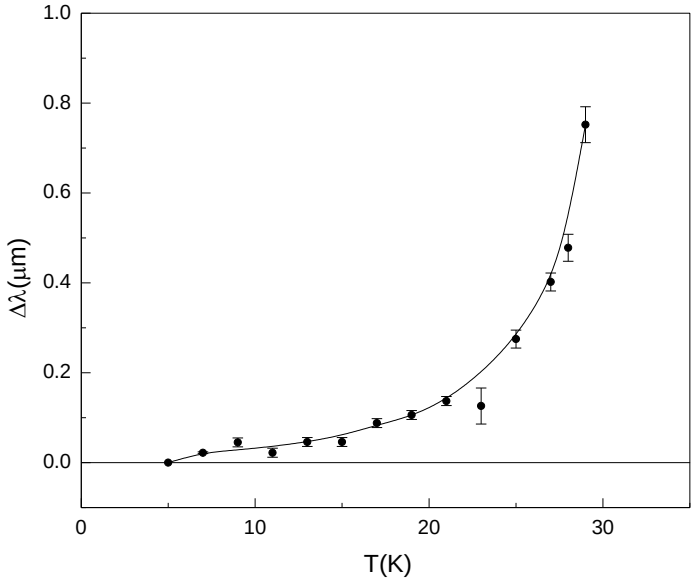

Figure 68: The temperature dependence of $\boldsymbol{\Delta\lambda = \lambda(T) - \lambda(0)}$ extracted from fits to vortex profiles.

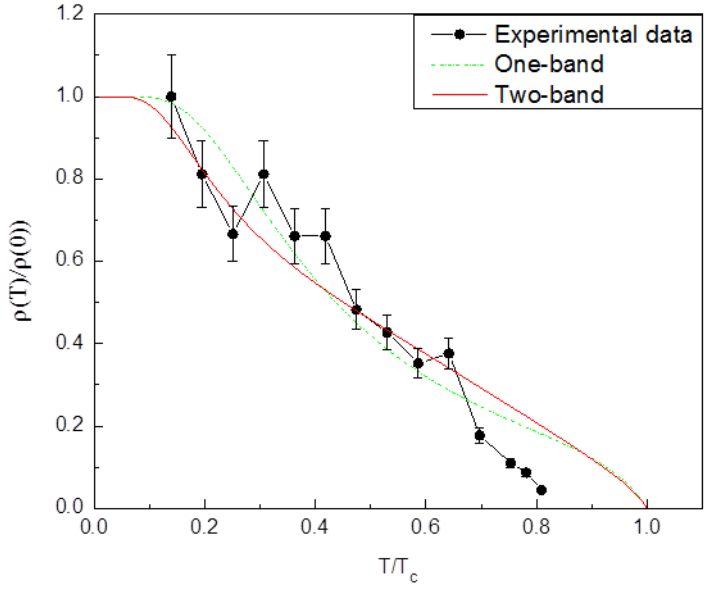

Figure 69: Temperature dependence of the normalised superfluid density $\boldsymbol{\overline{\rho}_s(T)}$ (points) and fits to a two band $\boldsymbol{\alpha}$-model (red solid line), where $\boldsymbol{p}$=0.4 ($\boldsymbol{a}_1$=$\boldsymbol{a}_2$=1, Δ_1=1.86kT$_c$, Δ_2=0.521kT$_c$). The results of fitting to a one band model where $\boldsymbol{a}$=0.998, Δ =0.8391kT$_c$ are shown in green (dashed).

Figure 70 shows the results of investigations of the vortex pinning landscape in the 160nm MgB_2 thin film by comparing images which were captured after repeated field-cooling from above T_c to 20K in two different fixed applied fields (H_z=+2.5Oe and H_z=+5Oe). Figure 70 (a) illustrates the three different field cooling cycles at 5G and it can be seen that the local vortex labyrinth-like structure is completely different after each cycle. In contrast Figure 70 (b) shows two cycles at 2.5G the vortex structure is nearly the same for both cycles with only small vortex shifts.

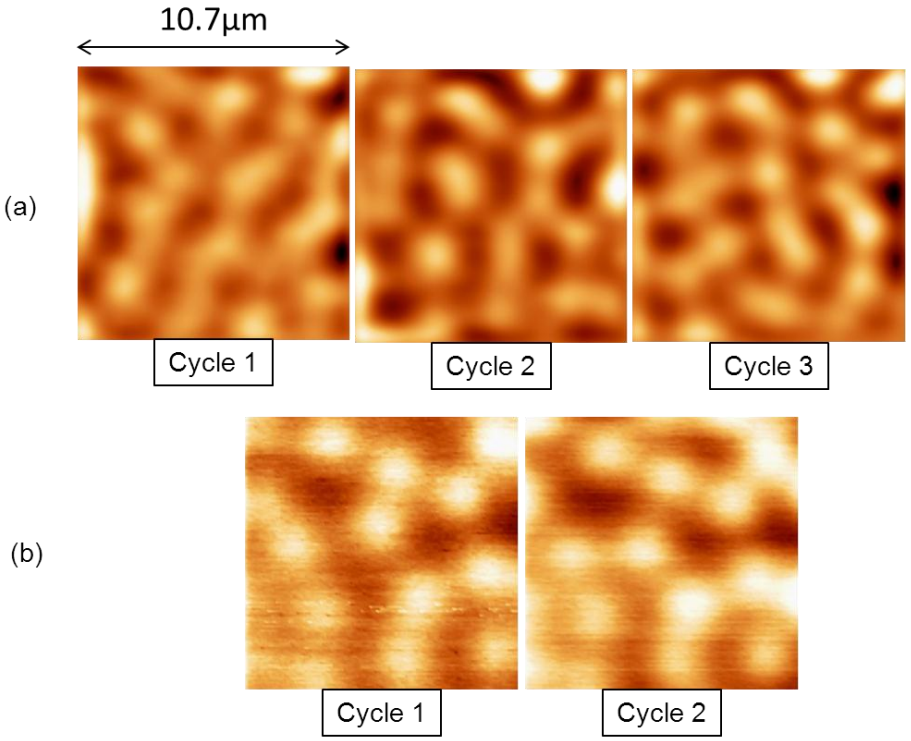

Figure 70: A series of vortex images captured after repeatedly field-cooling the 160nm MgB_2 sample from above T_c to T=20K in applied magnetic fields of (a) H_z=+5 Oe and (b) +2.5 Oe.

Finally, the nearest neighbour distribution of vortices in the two MgB_2 thin films (160nm and 77nm) was investigated at different applied fields. Figure 71 illustrates SHPM images of the vortex distribution in the 160nm MgB_2 thin film after field cooling from above T_c to 1.7K in various perpendicular magnetic fields (1.25, 1.7, 2.8 and 5G). At each magnetic field, a composite image is formed by aligning between 16 and 25 individual

scans in a jigsaw-like fashion. The whole area of the composite was ≈ 50×50 μm^2, yielding an overview of the vortex structure over a large area. The results show that for the three lowest fields, the vortices exhibit pronounced chain formation linked to distortions of the ideal Abrikosov lattice. At the highest field more labyrinth-like vortex structures are observed.

In an ideal Type-II superconductor vortices arrange themselves in a triangular Abrikosov lattice with a lattice constant of $a = \left(2\phi_o / B\sqrt{3}\right)^{1/2}$. Investigations of the nearest neighbour distribution after Delaunay triangulation is a powerful statistical technique for capturing information about deviations from this ideal lattice structure. Figure 72 shows histograms of the nearest neighbour vortex-vortex separations after Delaunay triangulation at different magnetic fields. In a field of 1.25G it can be seen that there is a weakly split bi-modal distribution around the normal lattice constant, $a_{1.25G}$. The histogram shows two distinct peaks corresponding to the average intra- and inter-chain bond lengths, rather than a single peaked Gaussian distribution. The vortex distribution does become more Gaussian as the field is increased up to 2.8G but with clear evidence for a short bond length shoulder (= intra-chain spacing). This shoulder is even more evident at 5G.

Figure 73a shows comparable data for the vortex distributions in a 77nm MgB_2 film, captured by SHPM after field-cooling from above T_c to 1.7K , at two different perpendicular magnetic fields (1.25 and 2.8). Composite images have been assembled over an area of ≃ 50×50μm^2 which again show pronounced chain formation. Figure 73b shows the nearest neighbour bond length histogram for both samples after Delaunay triangulation. The histogram at 1.7G again exhibits a weakly split bi-modal distribution whereas that at 2.8G shows an approximately Gaussian distribution, with clear evidence of small shoulder at shorter bond lengths.

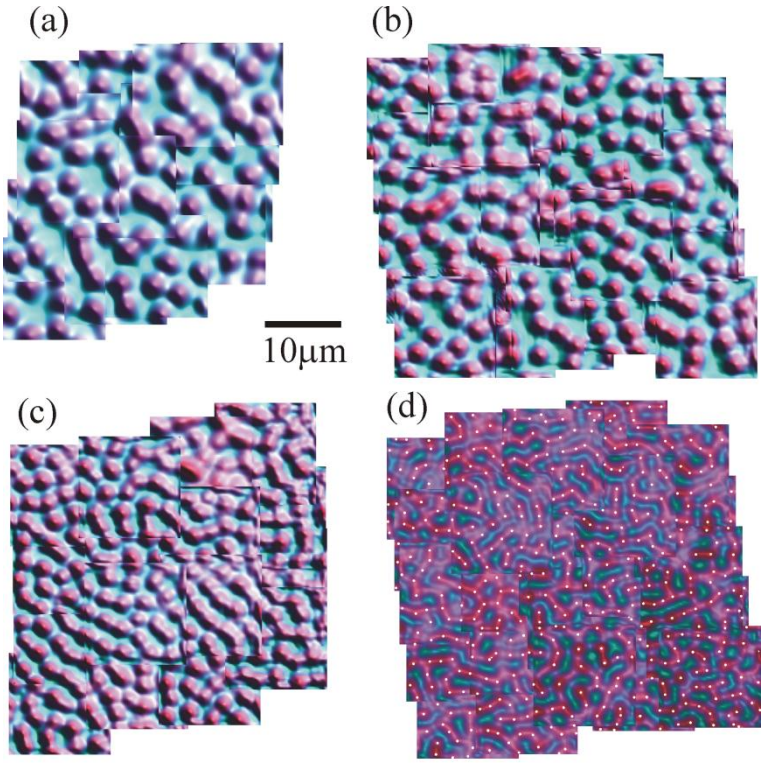

Figure 71: Composite SHPM images assembled from 16 to 25 individual scans of the 160nm MgB_2 thin film taken at T≈1.6K after field-cooling in a perpendicular magnetic field of (a) 1.25G, (b) 1.7 G, (c) 2.8 G and (d) 5G.

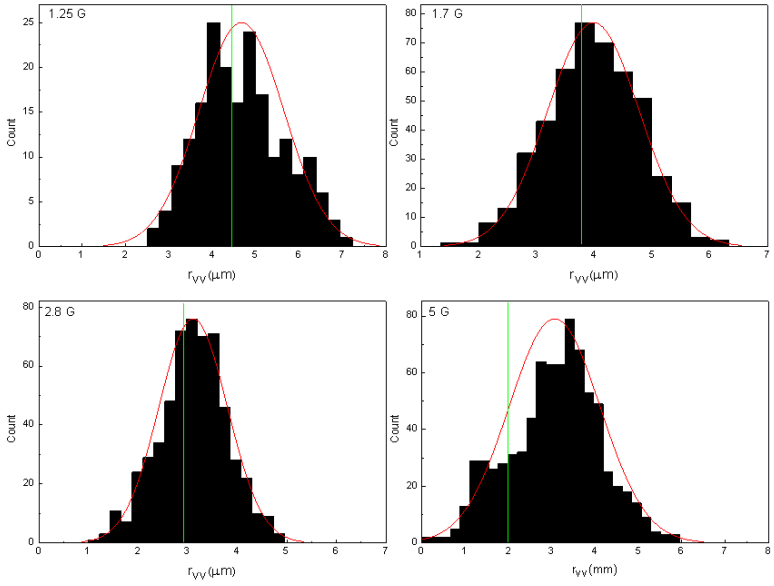

Figure 72: Histograms of the nearest neighbour vortex bond length distributions after Delaunay triangulation with superimposed Gaussian fits (red line). Green lines indicate the estimated lattice constant for an ideal Abrikosov lattice.

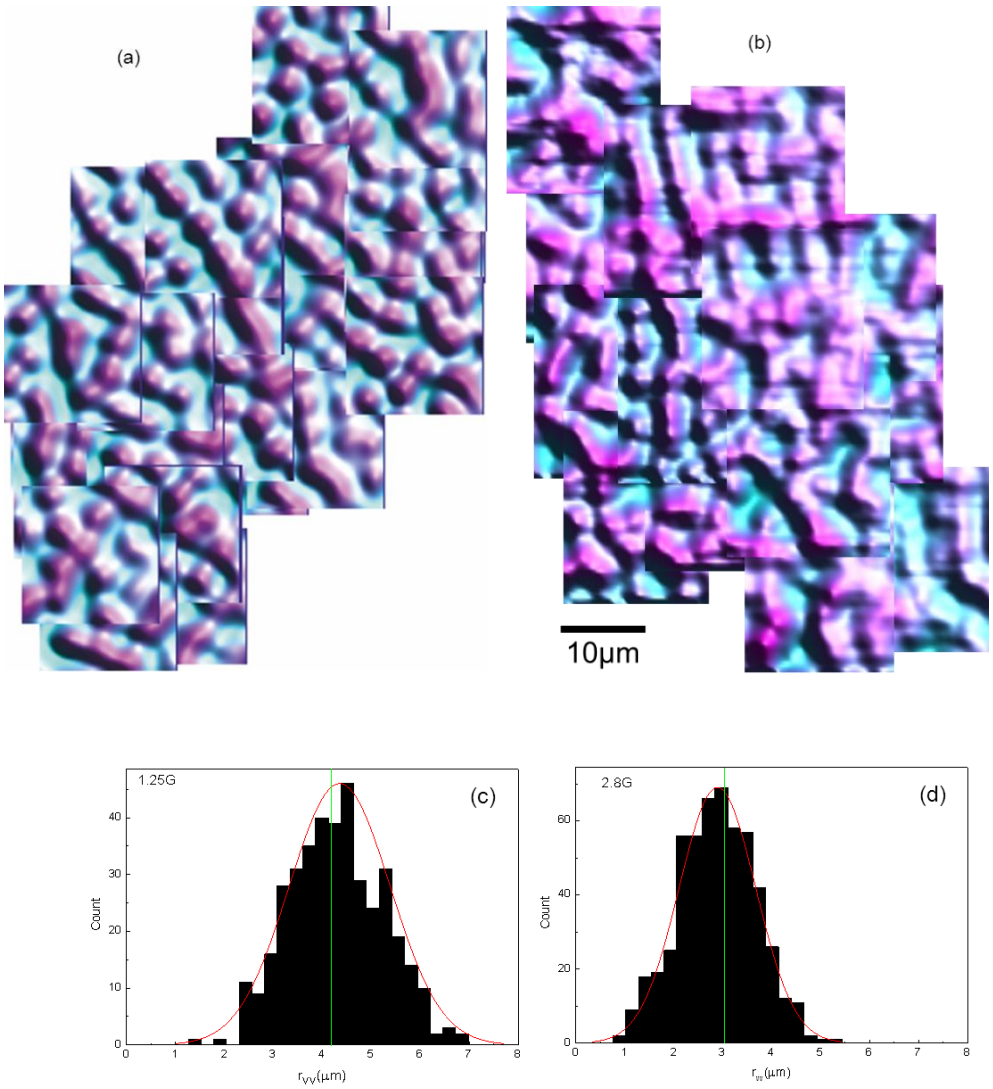

Figure 73 a,b: Composites of 16 to 25 SHPM images for the 77nm MgB_2 thin film imaged at T≈1.6K after field-cooling from above T_c in a perpendicular magnetic field of ((a)1.25G and (b) 2.8G). The whole scan area is ≈50×50μm^2.(c,d) Vortex nearest neighbor bond length histograms after Delaunay triangulation with superimposed Gaussian fits (red line). The estimated lattice spacing for an ideal Abrikosov lattice is indicated by vertical green lines.

6.4 Discussion

We have estimated the temperature-dependent superfluid density for a 160nm thick MgB_2 thin film from penetration depths extracted from theoretical fits to the magnetic profiles of a single vortex [213]. Figure 69 reveals that we obtain better fits of our experimental superfluid density data to a two gap model than a one gap model.

The Fermi surface of MgB_2 is comprised of four sheets [36]. Our fitting suggests that the smaller cylindrical σ sheets (two sheets) sited around the four Γ-A lines have a superconducting energy gap of $\Delta_1 \sim 1.86 \pm 0.3 kT_c$. The other two sheets which resemble webbed tunnels and are generated from the π-bonding of boron and sited around the K-M and H-L lines, have an energy gap of $\Delta_2 \sim 0.52 \pm 0.1 kT_c$. Assuming that both bands have an isotropic s-wave gap (a_1=a_2=1) the fitted value of $p \simeq 0.4$ for band 1 indicates that there is nearly equal contribution to the superfluid density from each of the bands, in agreement with several other results [34, 104, 188-190, 213].

From figure 71, it can be seen that there is clear evidence for the formation of vortex chains whose direction varies by $\sim 45^o$ at different fields, and which vanish at the highest applied field. These observations suggest that this behaviour is not related to some form of disorder in the samples. Furthermore, the observation that repeatedly cooled vortex structures at 2.5G are very similar, while at 5G they are entirely different (see figure 70) suggests that there is relatively low density of quite strong pinning sites. These pinning sites are able to pin nearly all vortices at low fields, but not at high fields when we see the labyrinth-like structure. This suggests that the broken symmetry of the vortex lattice in these MgB_2 films is probably not related to material defects [215].

At 1.25G, in figure 72, weak peak-splitting of the vortex nearest neighbour bondlength distribution was found after Delaunay triangulation, reflecting the average intra-chain and inter-chain bond lengths. To confirm statistically whether this is the case, we estimated the intra (4μm yellow) and inter (5μm black) vortex bond lengths and superimposed these on a

small number of vortices in an individual scan. Figure 74 shows that these estimated values of bond lengths are consistent with the two peaks in the 1.25G distribution curve (see figure 72).

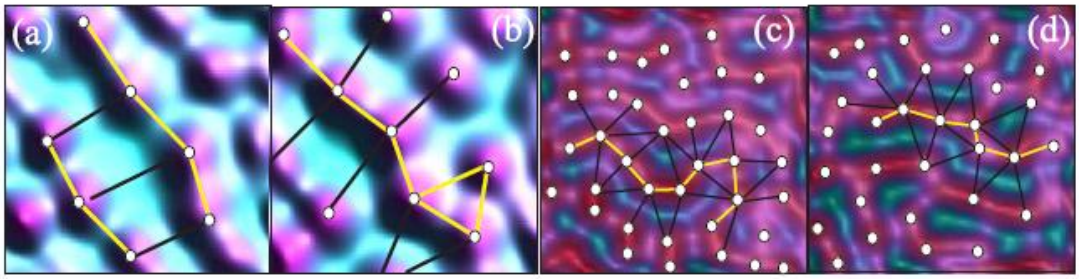

Figure 74: Individual vortex images at magnetic field of 1.25G (a), (b) and 5G (c), (d), with superimposed nets representing the vortex intra- and inter-chain bond lengths (see text).

At intermediate fields (1.7 G and 2.8 G), the vortex bond length histogram becomes nearly Gaussian, with peak spacings of 4μm and 3.1μm at 1.7G and 2.8G, respectively. These values are very close to the calculated values for an ideal triangular lattice at these fields, i.e. a_{tri} (1.7G) = 3.8μm and a_{tri}(2.8G) = 2.9μm.

At the same time, deviations from an ideal vortex distribution are evident as a small low bond length shoulder at 2.8G. This shoulder becomes much more pronounced at 5G and the two spacings appear plausible when both bonds (short and long) are fitted by eye, as shown in figure 74 (a)&(b). Moreover, the histogram at 5G shows an approximately bi-modal distribution with longer inter-chain bond length and shorter intra-chain bonds. Note that each vortex in the chain only has two short bonds whereas there are typically 4 bonds to adjacent ‘chains’. Figure 73 shows the same behaviour for a 77nm thin film. The bond length histogram again shows evidence for peak-splitting at 1.25G and a Gaussian distribution at 2.8G with a small shoulder at short bond lengths.

From previous discussion in the literature, there are many different mechanisms involved in the transition from a chained vortex structure to a labyrinth-like structure in a system with repulsive and attractive

interactions [216]. Indeed, the existence of long-range attraction and short-range repulsion can lead to formation of an ideal triangular lattice as the ground state (minimum potential) and has been used to describe the unusual vortex structures (Type II clusters surrounded by Type I) found in low-κ Type II materials in so called Type-II\1 systems [217, 218].

Some recent theoretical studies (e.g. molecular dynamics simulations), have predicted that vortices in the presence of non-monotonic interactions form clumps as the ground state of a system with short-range repulsive (SRR) and long-range attractive (LRA) interactions, which subsequently evolve into "labyrinths" at higher fields [219]. In this light vortex structures containing clumps, labyrinths and voids are expected, but the chain-like structures we observe may follow the physics of low-κ Type-II\1 materials theory rather than type 1.5 ones [218].

Several techniques have been used to investigate low-field vortex structures in MgB_2 and results suggest the existence of an attractive component in the vortex interaction in MgB_2 [101, 196, 197]. For instance, in 2012, Gutierrez *et al.* [197] found that the vortex structure in a MgB_2 single crystal are characteristic of stabilisation under a long-range and short-range repulsion combined with an intermediate-range attraction (IRA) [220, 221].

In our experiments, the average intra-chain vortex spacing decreased with increasing magnetic field from 4μm for the lowest field (B =1.25G) to 1.6μm for the highest field (B=5G) for the 160nm film. The same behaviour was observed for the thinner 77nm film, with an intra-chain vortex spacing of 4.2μm at 1.25G falling to 3μm at 2.8G (see Figure73). This field-dependence of the intra-chain vortex spacing is not expected and may be due to the broad and shallow vortex-vortex interaction potential in our samples. Note that molecular dynamics simulations for an SRR/IRA/LRR inter-vortex potential are consistent with field-dependent intra-chain vortex spacings [220]. In contrast vortex patterns in MgB_2 single crystals and Type-II\1 superconductors [197, 217] suggest that there is field-independent intra-

chain or intra-cluster spacing which is consistent with existence of a minimum in the vortex-vortex interaction potential. In general, the histogram of vortex bond lengths at 1.25G, 2.8G and 5G in the 160nm film indicate that there is a broken symmetry as reflected in the bi-modal distributions, whilst the nearest neighbour distribution at 1.7G shows an approximately Gaussian distribution suggesting a convergence of intra- and inter-chain bond lengths. However, the nearest neighbour distribution in the 77nm thin film shows broken symmetry at both fields (1.25G, 2.8G). It is expected theoretically that there should be a vortex-vortex spacing at which an ideal Abrikosov lattice spacing is the ground state we speculate that at around 1.7G the Gaussian distribution of nearest neighbour bond lengths in the 160nm film approximately reflects this equilibrium spacing.

Besides the six theories which were described by Brandt and Das to explain vortex-vortex attraction, the identification of type 1.5 superconductivity has led to a seventh theory. In the remainder of this chapter the results of our research will be considered in the light of these theories, i.e., whether they support them or provide alternative avenues for further investigation. The first of these theories relates to BCS corrections to GL theory [222], important for vortex structures in low-κ Type-II\1 superconductors. These have been verified to be important experimentally in the range $0.45 \leq \kappa \leq 1.1$ around the Type-II\1 / Type-II\2 phase boundary [223]. In this work, the values of $\kappa_i \approx 2{,}3$ estimated for individual bands put our samples outside the range of this mechanism, whereas calculations for MgB_2 crystals in the clean limit certainly put κ_π within it [101]. The second theory pertains to tilted fields in highly anisotropic superconducting crystals [224]. Chains are observed in cuprate superconductors such as BSCCO and YBCO in tilted fields ($> 70^o$ from high symmetry c-axis), due to the highly anisotropic nature of these materials ($\gamma_{BSCCO} \approx$50 to 200) [225-229]. In our experimental system, the applied magnetic fields are nearly perpendicular to the MgB_2 films and this anyway is a relatively low anisotropy material ($\gamma_{MgB2} \approx$1.1)[105].

The third and fourth theories relate to a type of “Casimir” force in layered materials [230], and a thermally activated van der Waals (vdW) type of interaction [231] respectively. It is argued that the former can occur at temperatures near T_c, whilst the latter can occur at the sample edge. Neither mechanism is relevant in our samples, because all measurements were at 1.7K, which is far from the critical temperature of MgB_2, and the scan area was situated at the centre of the sample far from the edges [232]. The fifth theory involves an impurity activated vdW-like interaction [233], and has been developed for highly anisotropic BSCCO-2212. The vortex-vortex interaction in our samples cannot be described by this approach, because MgB_2 has relatively low anisotropy as compared to the cuprates [197, 233].

The sixth theory relates to corrections to simple GL or London theories [234], due to a non-local extension of the London theory with Pippard theory. An attraction between the vortices is expected to exist when $\Re[\Lambda^{-1}] < \xi_0^{-1}$, where Λ and ξ_0 are the magnetic and order parameter (decay length) [234] and $\Re[-]$ means the real part of the argument number. Both parameters Λ and ξ_0 are strongly dependent on the electronic mean free path [235].

The final theory relates to Type-1.5 physics, for which it has been conjectured that attraction may occur in the two component GL model of a two-band superconductor in the range $\xi_1 < \sqrt{2}\lambda < \xi_2$, where λ is the magnetic penetration depth and ξ_1, ξ_2 are the inverse field masses (not coherence lengths) linked to the π and σ bands, which describe the behaviour of the density fields [110]. These length scales become equivalent to ξ_π, ξ_σ, in the interband Josephson coupling range.

In the dirty limit when $\ell \ll \xi$, the superconducting coherence length can be estimated from [50].

$$\lambda_{eff}(T) = \frac{\lambda_L}{(2(1-t))^{\frac{1}{2}}}\left(\frac{\xi_0}{1.33\ell}\right)^{\frac{1}{2}}, \qquad (6.1)$$

and

$$\xi_{eff}(T) = \frac{0.855(\ell\xi_0)^{\frac{1}{2}}}{(1-t)^{\frac{1}{2}}} \ , \qquad (6.2)$$

where ξ_0 is the BCS coherence length and $t = T/T_c$, where T_c is the superconducting critical temperature and ℓ is the mean free path. The values of the coherence lengths $\xi_o^{\pi} \simeq 64\text{nm}$ and $\xi_o^{\sigma} \simeq 14\text{nm}$ are generally estimated using the equation ($\xi_0 = \hbar v_F/\pi\Delta_o$), where v_F is the Fermi velocity (v_F^{π}= 5.35×10^{5}ms^{-1}, v_F^{σ} = 4.4×10^{5}ms^{-1}) [236] and Δ_o is the energy gap ($\Delta_\pi(0)$= 1.73 meV , $\Delta_\sigma(0)$ = 6.2 meV from our fitting procedure) [36, 112, 237, 238]. From equation 6.1 and 6.2, the values of ξ_{eff}^{π}≃23.2nm, ξ_{eff}^{σ}≃11.2nm and λ_{eff}^{π} = 34.7nm, λ_{eff}^{σ}= 50.8nm are calculated inputting our estimated value of the mean free path (ℓ = 11nm), the measurement temperature T=1.6K and $\lambda_L^{\pi} = 33.6\text{nm}$ and $\lambda_L^{\sigma} = 47.8\text{nm}$ inferred from the plasma frequency measurement for both band ($\omega_{p\pi}, \omega_{p\sigma}$)[50] and the equation $\lambda_L = {}^{c}/_{\omega_p}$ [97]. Thus, for the estimated magnetic penetration depth is λ=61.5nm, where $\lambda = [\lambda_\pi^2 + \lambda_\sigma^2]^{-1/2}$ [101], these suggests that our samples lie outside the type 1.5 range ($\xi_1 < \sqrt{2}\lambda < \xi_2$), noting that the link to the G-L coherence length is only valid when the interband Josephson coupling is small.

6.5 Conclusion

The estimated temperature-dependent superfluid density for our MgB_2 thin film fits well to a two band α-model with two full gaps within experimental errors. The superfluid density was calculated from penetration depths extracted from fits of vortex profiles to a theoretical model for thin films. Our fit parameters suggest that the superconducting gaps on the two different band are given by Δ_1~1.86±0.3kT_c and Δ_1~0.52±0.1kT_c, with the fractional contribution of the first band p=0.4.

The vortex-vortex interaction in MgB_2 thin films with different thicknesses (77nm, 160nm) has been investigated with SHPM. The vortex patterns spontaneously break symmetry with a dominant chain direction at fields of 1.25G, 1.7G and 2.8G, and a labyrinth-like structure at 5G in the 160nm thin film. In a thinner 77nm film, chain formation is again observed at 1.25G and 2.8G.

A statistical analysis provides evidence for a peak-splitting in the distribution of nearest neighbour bond lengths at the lowest field in both films, and a short bond length shoulder at all other fields. This splitting is attributed to the intra- and inter-chain bond lengths. At the other fields a distorted Gaussian distribution is obtained due to the presence of chain-like structures and the average distance between each vortex was roughly equal to the expected isotropic Abrikosov lattice parameter. The results for both films may be consistent with a system of short-range repulsive, intermediate range attractive and long-range repulsive interactions.

The viability of seven possible theories for attractive vortex interactions has been assessed and reviewed in the light of the extremely short electronic mean free path in our samples. Five of these theories can be eliminated due to the low level of anisotropy in our samples and the angle of the applied field. Careful analysis of the thin films reveal that their superconducting length scales appear to lie outside the range required to observe type 1.5 behaviour. Finally, the sixth theory may provide some explanation for the observed vortex structures under the condition of this theory, but more theoretical work needs to be carried out to confirm this.

Chapter seven: Final conclusions and future work

7.1 Local measurement of the superfluid density in different 122 iron-based superconductors.

Scanning Hall probe microscopy images have been exploited to make a quantitative analysis of the magnetic profiles of well-isolated single vortices in single crystals of $SrFe_{2-x}Co_xAs$ (x=0.11) and $BaFe_{2-x}Co_xAs$ (x=0.075 and 0.113). The superfluid density is inferred from the penetration depths calculated by fitting vortex profiles to an established model. Fits of the temperature-dependent superfluid density have provided good agreement with a two band α–model in all samples. The fit parameters for $SrFe_{2-x}Co_xAs$ (x=0.11) suggest that the electron pocket gap appears to be approximately isotropic s-wave, while the fit parameters of the $BaFe_{2-x}Co_xAs$ (x=0.075 and 0.113) samples indicate that the gap is strongly anisotropic, possibly non-monotonic d-wave with nodes at the Fermi surface.

Typical pinning forces at low magnetic fields were calculated from deviations of the vortex structure from an ideal triangular lattice in the $SrFe_{2-x}Co_xAs$ (x=0.11) sample, allowing lower bound estimates of the critical current. Our estimates are smaller than other values found in the literature for similar superconducting crystals by several orders of magnitude and this may be due to the presence of collective pinning effects in these materials at high fields. Repeating these measurements in samples with different doping levels may provide a deeper understanding of the mechanism of superconductivity in iron-based materials and could help to understand the physics of other high temperature superconductors and multiband superconductor materials. Finally, investigations of vortex-vortex interactions in single crystal and different film thicknesses of iron-based superconductors over a large area may help to identify the details of inter-vortex interactions in another family of multiband superconducting materials such as Pb and $NbSe_2$.

7.2 Local measurements of the superfluid density and the vortex-vortex interaction in MgB_2 thin films.

The local temperature-dependent superfluid density of a 160nm thick MgB_2 thin film was mapped experimentally using a scanning Hall probe microscope. The resulting data fit well to a two band α-model with two full gaps and the fit parameters have been used to infer the value of the gaps on the two bands, and the fractional contribution to the superfluid density from each. These are in reasonable agreement with other results in the literature.

In addition, the vortex-vortex interaction in different thickness (77nm and 160nm) MgB_2 thin films was probed using SHPM. Vortices have generally been observed to have a tendency to order into chains with one single dominant direction. The exception to this is in the 160nm sample at 5G, when a labyrinth-like structure is observed. The reproducibility of vortex structures after repeated field-cooling suggests that the observed broken symmetry vortex structures are probably not the result of material defects. Our results are surprisingly similar to other measurements of vortices in MgB_2 single crystals even though our films must be much more disordered. Clearly further theoretical analysis is needed to understand vortex-vortex interactions and vortex structures in these thin films. Repeating this work with different film thicknesses over a wide range of applied magnetic fields with more theoretical studies should be carried out to explore the physics further. In particular, at high field vortex densities the structure is expected to revert to an ideal triangular lattice. Measurements with smaller Hall probes would be required help to resolve vortex structures at higher magnetic fields. In addition, studying the vortex structure in other multiband superconducting materials such as Pb, $NbSe_2$ and iron-based with more theoretical studies (such as molecular dynamic simulation) on the subject of unconventional vortex-vortex interactions with stress on the calculation of short- and long-range interaction.

7.3 List of publications

1) Desoky, W. M., Bending, S. J. and Sebastian, S. E., 2012. Multiband superconductivity in Co-doped $SrFe_2As_2$ investigated using local magnetic imaging. Superconductor Science and Technology, 25 (4), 045011.
2) Bending, S. J., Curran, P. J., Desoky, W. M. A., Khotkevych, V. V., Gibbs, A., Mackenzie, A. P., Tamegai, T. and Sebastian, S. E., 2012. Vortex imaging in unconventional superconductors. Physica C: Superconductivity and its Applications, 479, pp. 65-68.

References

1 H. K. Onnes, Leidden Comm, 120b (1911).

2 D. R. Patel CKN, Proceedings of the national academy of science of the United States Of America **85**, 4945 (1988).

3 W. Meissner and R. Ochsenfeld, Die Naturwissenschaften **21**, 787 (1933).

4 F. London and H. London, Royal Society of London (London) **A149** (1935).

5 V. L. Ginzburg and L. D. Landau, Zh. Eksperim. i Teor. Fiz **20** (1950).

6 A. A. Abrikosov, Sov. Phys. JETP **5**, 1174 (1957).

7 J. Bardeen, L. N. Cooper, and J. R. Schrieffer, Physical Review **108**, 1175 (1957).

8 G. Bednorz and K. Müller, Z. Phys **B 64**, 189 (1986).

9 Z . Z. Sheng and A. M. Hermann, Nature **332**, 55 (1988).

10 J. Nagamatsu, N. Nakagawa, T. Muranaka, Y. Zenitani, and J. Akimitsu, Nature **410**, 63 (2001).

11 Y. Kamihara, T. Watanabe, M. Hirano, and H. Hosono, Journal of the American Chemical Society **130**, 3296 (2008).

12 Z.-A. Ren, et al., Europhysics Letters **83** 17002 (2008).

13 S. Uchida, J. Phys. Soc. Jpn. **77**, 9 (2008).

14 C. P. Poole, H. A. Farach, and R. J. Creswick, Superconductivity, Academic Press (1995).

15 D. R. Tilley and J. Tilley, *Superfluidity and Superconductivity* (Adam Hilger, Bristol and Boston 1986).

16 A. C. Rose-Innes and A. C. Rhoderick, *Introduction to Superconductivity* (Pergamon Press, 1978).

17 M. Tinkham, *Introduction to Superconductivity* (McGraw-Hill, New York, 1996).

18 H. Frohlich, Phys. Rev **79**, 845 (1950).

19 A. Carrington and F. Manzano, Physica C: Superconductivity **385**, 205 (2003).

20 M. Cyrot and D. Pavuna, *Introduction to superconductivity and high-Tc materials*, 1992).

21 H. Suhl, B. T. Matthias, and L. R. Walker, Physical Review Letters **3**, 552 (1959).

22 M. Iavarone, et al., Physical Review Letters **89**, 187002 (2002).

23 R. Nagarajan, C. Mazumdar, Z. Hossain, S. K. Dhar, K. V. Gopalakrishnan, L. C. Gupta, C. Godart, B. D. Padalia, and R. Vijayaraghavan, Physical Review Letters **72**, 274 (1994).

24 Y. Nakajima, T. Nakagawa, T. Tamegai, and H. Harima, Physical Review Letters **100**, 157001 (2008).

25 L. P. Gor'kov, Sov. Phys. JETP **9**, 1364 (1959).

26 K. Kuroki, S. Onari, R. Arita, H. Usui, Y. Tanaka, H. Kontani, and H. Aoki, Physical Review Letters **101**, 087004 (2008).

27 I. I. Mazin, D. J. Singh, M. D. Johannes, and M. H. Du, Physical Review Letters **101**, 057003 (2008).

28 J. Charles P. Poole, Horacio A. Farach, Richard J. Creswick, *Superconductivity* (Elsevier, 2007).

[29] W. N. Hardy, D. A. Bonn, D. C. Morgan, R. Liang, and K. Zhang, Physical Review Letters **70**, 3999 (1993).
[30] R. Prozorov and R. W. Giannetta, Superconductor Science and Technology **19**, R41 (2006).
[31] B. Muhlschlegel, Z. Phys. **155**, 313 (1959).
[32] R. T. Gordon, et al., Physical Review Letters **102**, 127004 (2009).
[33] P. W. Anderson, Journal of Physics and Chemistry of Solids **11**, 26 (1959).
[34] F. Bouquet, R. A. Fisher, N. E. Phillips, D. G. Hinks, and J. D. Jorgensen, Physical Review Letters **87**, 047001 (2001).
[35] W. M. Desoky, S. J. Bending, and S. E. Sebastian, Superconductor Science and Technology **25**, 045011 (2012).
[36] H. J. Choi, D. Roundy, H. Sun, M. L. Cohen, and S. G. Louie, Nature **418**, 758 (2002).
[37] R. Huebener, *Magnetic Flux Structures in Superconductors* (Springer, Berlin, 2003).
[38] J. Bardeen and M. J. Stephen, Physical Review **140**, A1197 (1965).
[39] P. W. Anderson and Y. B. Kim, Reviews of Modern Physics **36**, 39 (1964).
[40] Z. Z. Sheng and A. M.Hermann, Nature **332**, 55 (1988).
[41] M. H. Julien, et al., Physical Review B **63**, 144508 (2001).
[42] G. Shirane, J. Als-Nielsen, M. Nielsen, J. M. Tranquada, H. Chou, S. Shamoto, and M. Sato, Physical Review B **41**, 6547 (1990).
[43] Ito T, Takagi H, Ishibashi S, Ido T, and U. S, Nature **350**, 596 (1991).
[44] Y. Sidis, C. Ulrich, P. Bourges, C. Bernhard, C. Niedermayer, L. P. Regnault, N. H. Andersen, and B. Keimer, Physical Review Letters **86**, 4100 (2001).
[45] C. Stock, et al., Physical Review B **73**, 100504 (2006).
[46] I. Felner, U. Yaron, I. Nowik, E. R. Bauminger, Y. Wolfus, E. R. Yacoby, G. Hilscher, and N. Pillmayr, Physical Review B **40**, 6739 (1989).
[47] A. Kebede, et al., Physical Review B **40**, 4453 (1989).
[48] D. W. Cooke, et al., Physical Review B **41**, 4801 (1990).
[49] A. Crisan, S. J. Bending, S. Popa, Z. Z. Li, and H. Raffy, Physical Review B **72**, 214509 (2005).
[50] I. I. Mazin, O. K. Andersen, O. Jepsen, O. V. Dolgov, J. Kortus, A. A. Golubov, A. B. Kuz'menko, and D. van der Marel, Physical Review Letters **89**, 107002 (2002).
[51] V. K. Vlasko-Vlasov, A. Koshelev, U. Welp, G. W. Crabtree, and K. Kadowaki, Physical Review B **66**, 014523 (2002).
[52] M. J. Geselbracht, T. J. Richardson, and A. M. Stacy, Nature **345**, 324 (1990).
[53] Y. Maeno, H. Hashimoto, K. Yoshida, S. Nishizaki, T. Fujita, J. G. Bednorz, and F. Lichtenberg, Nature **372**, 532 (1994).
[54] K. Takada, H. Sakurai, E. Takayama-Muromachi, F. Izumi, R. A. Dilanian, and T. Sasaki, Nature **422**, 53 (2003).
[55] E. Morosan, H. W. Zandbergen, B. S. Dennis, J. W. G. Bos, Y. Onose, T. Klimczuk, A. P. Ramirez, N. P. Ong, and R. J. Cava, Nat Phys **2**, 544 (2006).

[56] S. Yamanaka, K.-i. Hotehama, and H. Kawaji, Nature **392**, 580 (1998).
[57] H.-H. Wen, G. Mu, L. Fang, H. Yang, and X. Zhu, EPL (Europhysics Letters) **82**, 17009 (2008).
[58] G. F. Chen, Z. Li, D. Wu, G. Li, W. Z. Hu, J. Dong, P. Zheng, J. L. Luo, and N. L. Wang, Physical Review Letters **100**, 247002 (2008).
[59] Z.-A. Ren, et al., EPL (Europhysics Letters) **82**, 57002 (2008).
[60] S. Matsuishi, Y. Inoue, T. Nomura, M. Hirano, and H. Hosono, Journal of the Physical Society of Japan **77**, 113709 (2008).
[61] L. F. Peng Cheng, Huan Yang, Xiyu Zhu, Gang Mu, Huiqian Luo, Zhaosheng Wang, Hai-Hu Wen, arXiv:0804.0835 [cond-mat.supr-con].
[62] M. Rotter, M. Tegel, and D. Johrendt, Physical Review Letters **101**, 107006 (2008).
[63] K. Sasmal, B. Lv, B. Lorenz, A. M. Guloy, F. Chen, Y.-Y. Xue, and C.-W. Chu, Physical Review Letters **101**, 107007 (2008).
[64] M. S. Torikachvili, S. L. Bud'ko, N. Ni, and P. C. Canfield, Physical Review Letters **101**, 057006 (2008).
[65] C. Wang, et al., EPL (Europhysics Letters) **83**, 67006 (2008).
[66] S. H. Baek, N. J. Curro, T. Klimczuk, E. D. Bauer, F. Ronning, and J. D. Thompson, Physical Review B **79**, 052504 (2009).
[67] C. de la Cruz, et al., Nature **453**, 899 (2008).
[68] K. Kitagawa, N. Katayama, K. Ohgushi, M. Yoshida, and M. Takigawa, Journal of the Physical Society of Japan **77**, 114709 (2008).
[69] M. A. McGuire, et al., Physical Review B **78**, 094517 (2008).
[70] Y. Kamihara, H. Hiramatsu, M. Hirano, R. Kawamura, H. Yanagi, T. Kamiya, and H. Hosono, Journal of the American Chemical Society **128**, 10012 (2006).
[71] J.-W. G. Bos, G. B. S. Penny, J. A. Rodgers, D. A. Sokolov, A. D. Huxley, and J. P. Attfield, Chemical Communications **0**, 3634 (2008).
[72] X. H. Chen, T. Wu, G. Wu, R. H. Liu, H. Chen, and D. F. Fang, Nature **453**, 761 (2008).
[73] R. Che, R. Xiao, C. Liang, H. Yang, C. Ma, H. Shi, and J. Li, Physical Review B **77**, 184518 (2008).
[74] H. Okada, K. Igawa, H. Takahashi, Y. Kamihara, M. Hirano, H. Hosono, K. Matsubayashi, and Y. Uwatoko, Journal of the Physical Society of Japan **77**, 113712 (2008).
[75] A. S. Sefat, R. Jin, M. A. McGuire, B. C. Sales, D. J. Singh, and D. Mandrus, Physical Review Letters **101**, 117004 (2008).
[76] A. Leithe-Jasper, W. Schnelle, C. Geibel, and H. Rosner, Physical Review Letters **101**, 207004 (2008).
[77] L. J. Li, et al., New Journal of Physics **11**, 025008 (2009).
[78] P. L. Alireza, Y. T. Ko, J. Gillett, C. M. Petrone, J. M. Cole, G. G. Lonzarich, and S. E. Sebastian, Journal of physics. Condensed matter : an Institute of Physics journal **21**, 012208 (2009).
[79] K. Igawa, H. Okada, H. Takahashi, S. Matsuishi, Y. Kamihara, M. Hirano, H. Hosono, K. Matsubayashi, and Y. Uwatoko, Journal of the Physical Society of Japan **78**, 025001 (2009).
[80] M. Reehuis and W. Jeitschko, J. Phys. Chem. Solids **51**, 961 (1990).
[81] C. W. Chu, et al., Physica C: Superconductivity **469**, 326 (2009).

[82] K. Sasmal, B. Lv, Z. J. Tang, F. Chen, Y. Y. Xue, B. Lorenz, A. M. Guloy, and C. W. Chu, Physical Review B **79**, 184516 (2009).
[83] J. H. Tapp, Z. Tang, B. Lv, K. Sasmal, B. Lorenz, P. C. W. Chu, and A. M. Guloy, Physical Review B **78**, 060505 (2008).
[84] S. Li, C. de la Cruz, Q. Huang, G. F. Chen, T. L. Xia, J. L. Luo, N. L. Wang, and P. Dai, Physical Review B **80**, 020504 (2009).
[85] J. W. Lynn and P. Dai, Physica C: Superconductivity **469**, 469 (2009).
[86] M. H. Fang, H. M. Pham, B. Qian, T. J. Liu, E. K. Vehstedt, Y. Liu, L. Spinu, and Z. Q. Mao, Physical Review B **78**, 224503 (2008).
[87] K.-W. Yeh, et al., EPL (Europhysics Letters) **84**, 37002 (2008).
[88] S. Margadonna, Y. Takabayashi, Y. Ohishi, Y. Mizuguchi, Y. Takano, T. Kagayama, T. Nakagawa, M. Takata, and K. Prassides, Physical Review B **80**, 064506 (2009).
[89] K. Nakayama, et al., EPL (Europhysics Letters) **85**, 67002 (2009).
[90] D. J. Singh and M. H. Du, Physical Review Letters **100**, 237003 (2008).
[91] I. I. Mazin and J. Schmalian, Physica C: Superconductivity **469**, 614 (2009).
[92] V. Brouet, et al., Physical Review B **80**, 165115 (2009).
[93] K. Terashima, et al., Proceedings of the National Academy of Sciences **106**, 7330 (2009).
[94] H. Shishido, et al., Physical Review Letters **104**, 057008 (2010).
[95] H. Luetkens, et al., Nat Mater **8**, 305 (2009).
[96] R. Khasanov, et al., Physical Review B **80**, 140511 (2009).
[97] M. Eisterer, Supercond. Sci. Technol. **20**, R47 (2007).
[98] S. L. Bud'ko, G. Lapertot, C. Petrovic, C. E. Cunningham, N. Anderson, and P. C. Canfield, Physical Review Letters **86**, 1877 (2001).
[99] Sergey LEE, Hatsumi MORI, Takahiko MASUI, Yuri ELTSEV, Ayako YAMAMOTO, and Setsuko TAJIMA, Journal of the Physical Society of Japan **70**, 2255 (2001).
[100] B. B. Jin, N. Klein, W. N. Kang, H.-J. Kim, E.-M. Choi, S.-I. Lee, T. Dahm, and K. Maki, Physical Review B **66**, 104521 (2002).
[101] V. Moshchalkov, M. Menghini, T. Nishio, Q. H. Chen, A. V. Silhanek, V. H. Dao, L. F. Chibotaru, N. D. Zhigadlo, and J. Karpinski, Physical Review Letters **102**, 117001 (2009).
[102] H. Suo, C. Beneduce, M. Dhallé, N. Musolino, J. Y. Genoud, and R. Flükiger, Applied Physics Letters **79**, 3116 (2001).
[103] D. C. Larbalestier, et al., Nature **410**, 186 (2001).
[104] P. Szabó, P. Samuely, J. Kačmarčík, T. Klein, J. Marcus, D. Fruchart, S. Miraglia, C. Marcenat, and A. G. M. Jansen, Physical Review Letters **87**, 137005 (2001).
[105] X. K. Chen, M. J. Konstantinović, J. C. Irwin, D. D. Lawrie, and J. P. Franck, Physical Review Letters **87**, 157002 (2001).
[106] M. Hanna, et al., Superconductor Science & Technology **21**, 045005 (2008).
[107] B. H. Moeckly and W. S. Ruby, Superconductor Science & Technology **19**, L21 (2006).
[108] E. Babaev and M. Speight, Physical Review B **72**, 180502 (2005).

[109] E. Babaev, J. Carlström, J. Garaud, M. Silaev, and J. M. Speight, Physica C: Superconductivity **479**, 2 (2012).
[110] J. Carlström, E. Babaev, and M. Speight, Physical Review B **83**, 174509 (2011).
[111] F. Bouquet, Y. Wang, R. A. Fisher, D. G. Hinks, J. D. Jorgensen, A. Junod, and N. E. Phillips, Europhys. Lett. **56**, 856 (2001).
[112] A. A. Golubov, J. Kortus, O. V. Dolgov, O. Jepsen, Y. Kong, O. K. Andersen, B. J. Gibson, K. Ahn, and R. K. Kremer, Journal of Physics: Condensed Matter **14**, 1353 (2002).
[113] G. Binnig, H. Rohrer, C. Gerber, and E. Weibel, Physical Review Letters **49**, 57 (1982).
[114] G. Binnig, C. F. Quate, and C. Gerber, Physical Review Letters **56**, 930 (1986).
[115] M. G and A. N. M, Appl. Phys. Lett. **57**, 12089 (1990).
[116] W. J. Kaiser and L. D. Bell, Physical Review Letters **60**, 1406 (1988).
[117] C. B. Prater, P. K. Hansma, M. Tortonese, and C. F. Quate, Rev. Sci. Instrum. **62**, 2634 (1991).
[118] A. Lewis, S. Lieberman, S. Haroush, V. Habib, R. Kopelman, and M. Isaacson, *Light microscopy beyond the limits of diffraction and to the limits of single molecule resolution, in Optical Microscopy for Biology* (Wiley- Liss, New York, 1993).
[119] H. K. Wickramasinghe, Scientific American **260**, 98 (1989).
[120] P. Muralt and D. W. Pohl, Appl. Phys. Lett. **48**, 514 (1986).
[121] S. J. Bending, Adv. Phys. **48**, 449 (1999).
[122] J. R. Kirtley, Physica C: Superconductivity **368**, 55 (2002).
[123] A. J. Heinrich, J. A. Gupta, C. P. Lutz, and D. M. Eigler, Science **306**, 466 (2004).
[124] V. V. Khotkevy and S. J. Bending, Journal of Physics: Conference Series **150**, 012021 (2009).
[125] A. Oral, S. J. Bending, and M. Henini, Appl. Phys. Lett. **69**, 1324 (1996).
[126] F. Bitter, Physical Review **38**, 1903 (1931).
[127] U. Essmann and H. Trauble, Physics Letters **24A**, 526 (1967).
[128] P. Rice and J. Moreland, Rev. of Scientific Inst. **62**, 844 (1991).
[129] A. Hubert and R. Schafer, *The analysis of magnetic microstructure* (Spring Berlin, New York, 1998).
[130] V. M. Hallmark, S. Chiang, J. F. Rabolt, J. D. Swalen, and R. J. Wilson, Physical Review Letters **59**, 2879 (1987).
[131] R. M. Feenstra and J. A. Stroscio, Physcia Scripta **T19**, 55 (1987).
[132] S. H. Pan, et al., Nature **413**, 282 (2001).
[133] M. F. Crommie, C. P. Lutz, and D. M. Eigler, Science **262**, 218 (1993).
[134] J. Bardeen, Physical Review Letters **6**, 57 (1961).
[135] C. J. Chen., *Introduction to Scanning Tunneling Microscopy* (Oxford University Press, 1993).
[136] J. Tersoff and D. R. Hamann, Physical Review Letters **50**, 1998 (1983).
[137] J. Tersoff and D. R. Hamann, Physical Review B **31**, 805 (1985).
[138] F. Ohnesorge and G. Binnig, Science **260**, 1451 (1993).
[139] M. Vogel, B. Stein, H. Pettersson, and K. Karrai, Appl. Phys. Lett. **78**, 2592 (2001).

[140] Y. Martin, D. W. Abraham, and H. K. Wickramasinghe, Appl. Phys. Lett. **52**, 1103 (1988).
[141] Y. Martin and H. K. Wickramasinghe, Appl. Phys. Lett. **50**, 1455 (1987).
[142] G. Meyer and N. M. Amer, Appl. Phys. Lett. **53**, 1045 (1988).
[143] R. Erlandsson, G. M. McClelland, C. M. Mate, and S. Chiang, J. Vac. Sci. Technol. A **6**, 266 (1988).
[144] M. Tortonese, R. C. Barrett, and C. F. Quate, Appl. Phys. Lett **62**, 834 (1993).
[145] L. Abelmann, et al., Journal of Magnetism and Magnetic Materials **190**, 135 (1998).
[146] http://www.idbscb.com/suppliers-products/nanomagnetics-instruments/low-temperature-scanning-hall-probe-microscope-lt-shpm/.
[147] C. Kittel, *Introduction to solid state physics* (Willey, Singapore, 1991).
[148] R. S. Popovic, *Hall effect devices, magnetic sensors and characterization of semiconductors* (Adam Hilger 1990).
[149] J. H. Davies, *The physics of low-dimensional semiconductors* (Cambridge University Press, 1998).
[150] K.S. Novoselov, S.V. Morozov, S.V. Dubonos, M. Missous, A.O. Volkov, D.A. Christian, and A. K. Geim., Journal of Applied Physics **93**, 10053 (2003).
[151] S. Liu, H. Guillou, A.D. Kent, G.W. Stupian, and M. S. Leung, Journal of Applied Physics **83**, 6161 (1998).
[152] H. Levinson, *Principles of lithography* (SPIE, Bellingham, Washington, 2005).
[153] Z. Cui, *Micro-nanofabrication technologies and application* (Springer, 2005).
[154] R. Williams, *Modern GaAs processing methods* (Artech House, Boston, London, 1990).
[155] K. V. V. a. S. J. B. S. J, Journal of Physics: Conference Series **150** (2009).
[156] S. J. Bending, Physica C: Superconductivity **470**, 754 (2010).
[157] Z.-A. Ren, et al., EPL (Europhysics Letters) **83**, 17002 (2008).
[158] S. K. Jun Sung Kim, Liqin Yan, N Manivannan, Yong Liu, Ingyu Kim, G R Stewart and Kee Hoon Kim, J. Phys.: Condens. Matter **21**, 102203 (2009).
[159] G. Wu, et al., EPL (Europhysics Letters) **84**, 27010 (2008).
[160] E. Colombier, M. S. Torikachvili, N. Ni, A. Thaler, S. L. Bud'ko, and P. C. Canfield, Supercond. Sci. Technol. **23** (2010).
[161] H. Ding , et al., Europhys. Lett. **83**, 47001 (2008).
[162] Evtushinsky D, et al., New Journal of Physics **11** (2009).
[163] D. V. Evtushinsky, et al., Physical Review B **79**, 054517 (2009).
[164] N. S. Hanaguri T, Kuroki K and Takagi H Science **328**, 5977 (2010).
[165] T. Kondo, et al., Physical Review Letters **101**, 147003 (2008).
[166] R. T. Gordon, et al., Physical Review B **79**, 100506 (2009).
[167] K. Hashimoto, et al., Physical Review Letters **102**, 207001 (2009).
[168] K. Hashimoto, et al., Physical Review B **81**, 220501 (2010).
[169] C. Martin, et al., Physical Review B **80**, 020501 (2009).
[170] Y. Nakajima, Y. Tsuchiya, T. Taen, T. Tamegai, S. Okayasu, and M. Sasase, Physical Review B **80**, 012510 (2009).

[171] R. Prozorov, et al., Physical Review B **78**, 224506 (2008).
[172] A. Yamamoto, et al., Appl. Phys. Lett. **94**, 062511 (2009).
[173] R. Prozorov, M. A. Tanatar, B. Shen, P. Cheng, H.-H. Wen, S. L. Bud'ko, and P. C. Canfield, Physical Review B **82**, 180513 (2010).
[174] J. C. Loudon, C. J. Bowell, J. Gillett, S. E. Sebastian, and P. A. Midgley, Physical Review B **81**, 214111 (2010).
[175] Y. Nakajima, T. Taen, and T. Tamegai, Physica C: Superconductivity **470, Supplement 1**, S408 (2010).
[176] A. Oral , S. J. Bending, and M. Henini, Appl. Phys. Lett. **69**, 1324 (1996).
[177] R. Prozorov, M. A. Tanatar, B. Roy, N. Ni, S. L. Bud'ko, P. C. Canfield, J. Hua, U. Welp, and W. K. Kwok, Physical Review B **81**, 094509 (2010).
[178] J. R. Kirtley, C. Kallin, C. W. Hicks, E. A. Kim, Y. Liu, K. A. Moler, Y. Maeno, and K. D. Nelson, Physical Review B **76**, 014526 (2007).
[179] L. Luan, et al., Physical Review B **81**, 100501 (2010).
[180] J. D. Fletcher, A. Carrington, O. J. Taylor, S. M. Kazakov, and J. Karpinski, Physical Review Letters **95**, 097005 (2005).
[181] L. Luan, T. M. Lippman, C. W. Hicks, J. A. Bert, O. M. Auslaender, J.-H. Chu, J. G. Analytis, I. R. Fisher, and K. A. Moler, Physical Review Letters **106**, 067001 (2011).
[182] J. Yong, S. Lee, J. Jiang, C. W. Bark, J. D. Weiss, E. E. Hellstrom, D. C. Larbalestier, C. B. Eom, and T. R. Lemberger, Physical Review B **83**, 104510 (2011).
[183] C.-L. Song, Hoffman, and J. E., Current Opinion in Solid State and Materials Science, http://dx.doi.org/10.1016/j.cossms.2013.03.005.
[184] A. Chubukov, Annual Review of Condensed Matter Physics **3**, 57 (2012).
[185] J-Ph Reid, et al., Superconductor Science and Technology **25**, 084013 (2012).
[186] J. K. Dong, et al., Physical Review Letters **104**, 087005 (2010).
[187] F. Giubileo, et al., Physical Review Letters **87**, 177008 (2001).
[188] P. Seneor, et al., Physical Review B **65**, 012505 (2001).
[189] H. Schmidt, J. F. Zasadzinski, K. E. Gray, and D. G. Hinks, Physical Review Letters **88**, 127002 (2002).
[190] H. D. Yang, J. Y. Lin, H. H. Li, F. H. Hsu, C. J. Liu, S. C. Li, R. C. Yu, and C. Q. Jin, Physical Review Letters **87**, 167003 (2001).
[191] L. F. C. A A Zhukov, K Yates, G K Perkins, Y Bugoslavsky, M Polichetti, A Berenov, J L Macmanus Driscoll, A D Caplin, L Hao and J Gallop 2001 **14** (Supercond. Sci. Technol. 14 No 5 (May 2001) L13-L16).
[192] R. A. Kaindl, M. A. Carnahan, J. Orenstein, D. S. Chemla, H. M. Christen, H.-Y. Zhai, M. Paranthaman, and D. H. Lowndes, Physical Review Letters **88**, 027003 (2001).
[193] S. L. Li, H. H. Wen, Z. W. Zhao, Y. M. Ni, Z. A. Ren, G. C. Che, H. P. Yang, Z. Y. Liu, and Z. X. Zhao, Physical Review B **64**, 094522 (2001).
[194] C. Panagopoulos, B. D. Rainford, T. Xiang, C. A. Scott, M. Kambara, and I. H. Inoue, Physical Review B **64**, 094514 (2001).
[195] A. V. Pronin, A. Pimenov, A. Loidl, and S. I. Krasnosvobodtsev, Physical Review Letters **87**, 097003 (2001).
[196] T. Nishio, V. H. Dao, Q. Chen, L. F. Chibotaru, K. Kadowaki, and V. V. Moshchalkov, Physical Review B **81**, 020506 (2010).

[197] J. Gutierrez, B. Raes, A. V. Silhanek, L. J. Li, N. D. Zhigadlo, J. Karpinski, J. Tempere, and V. V. Moshchalkov, Physical Review B **85**, 094511 (2012).
[198] A. J. M. van Erven, T. H. Kim, M. Muenzenberg, and J. S. Moodera, App. Phys. Lett. **81**, 4982 (2002).
[199] P. C. Canfield, D. K. Finnemore, S. L. Bud'ko, J. E. Ostenson, G. Lapertot, C. E. Cunningham, and C. Petrovic, Physical Review Letters **86**, 2423 (2001).
[200] S. M. Kazakov, R. Puzniak, K. Rogacki, A. V. Mironov, N. D. Zhigadlo, J. Jun, C. Soltmann, B. Batlogg, and J. Karpinski, Physical Review B **71**, 024533 (2005).
[201] S. Lee, T. Masui, H. Mori, Y. Eltsev, A. Yamamoto, and S. Tajima, Supercond. Sci. Technol. **16**, 213 (2003).
[202] U. Welp, et al., Physica C: Superconductivity **385**, 154 (2003).
[203] M. H. Jung, M. Jaime, A. H. Lacerda, G. S. Boebinger, W. N. Kang, H. J. Kim, E. M. Choi, and S. I. Lee, Chemical Physics Letters **343**, 447 (2001).
[204] H. Yang, et al., Physical Review Letters **101**, 067001 (2008).
[205] J. M. An and W. E. Pickett, Physical Review Letters **86**, 4366 (2001).
[206] J. Kortus, I. I. Mazin, K. D. Belashchenko, V. P. Antropov, and L. L. Boyer, Physical Review Letters **86**, 4656 (2001).
[207] Y. Wang, T. Plackowski, and A. Junod, Physica C: Superconductivity **355**, 179 (2001).
[208] A. Carrington, et al., Physical Review B **72**, 060507 (2005).
[209] A. Carrington, et al., Physical Review Letters **91**, 037003 (2003).
[210] J. R. Cooper, et al., Physica C: Superconductivity **385**, 75 (2003).
[211] J. D. Fletcher, A. Carrington, S. M. Kazakov, and J. Karpinski, Physical Review B **70**, 144501 (2004).
[212] E. A. Yelland, J. R. Cooper, A. Carrington, N. E. Hussey, P. J. Meeson, S. Lee, A. Yamamoto, and S. Tajima, Physical Review Letters **88**, 217002 (2002).
[213] A. M Chang, H. D. Hallen, H. F. Hess, H. L. Koa, J. Kwo, A. Sudbo, and T. Y. Chang, Europhys. Lett. **20**, 645 (1992).
[214] Jeehoon Kim, et al., Supercond. Sci. Technol. **25**, 112001 (2012).
[215] A. I. Larkin and Yu. N. Ovchinnikov, Journal of Low Temperature Physics **34**, 409 (1979).
[216] M. Seul and D. Andelman, Science **267**, 476 (1995).
[217] E. H. Brandt, Rep. Prog. Phys **58**, 1465 (1995).
[218] E. H. Brandt and M. P. Das, J. Supercond. Nov. Magn. **24**, 57 (2011).
[219] H. J. Zhao, V. R. Misko, and F. M. Peeters, Physica C: Superconductivity **479**, 130 (2012).
[220] C. J. Olson Reichhardt, C. Reichhardt, and A. R. Bishop, Physical Review E **82**, 041502 (2010).
[221] X. B. Xu, H. Fangohr, Z. H. Wang, M. Gu, S. L. Liu, D. Q. Shi, and S. X. Dou, Physical Review B **84**, 014515 (2011).
[222] E. H. Brandt, Physics Letters A **51**, 39 (1975).
[223] H. W. Weber, E. Seidl, M. Botlo, C. Laa, E. Mayerhofer, F. M. Sauerzopf, R. M. Schalk, H. P. Wiesinger, and J. Rammer, Physica C: Superconductivity **161**, 272 (1989).

[224] A. I. Buzdin and A. Y. Simonov, Physica C: Superconductivity **168**, 421 (1990).
[225] S. L. Lee, et al., Physical Review B **55**, 5666 (1997).
[226] M. B. Gaifullin, Y. Matsuda, N. Chikumoto, J. Shimoyama, and K. Kishio, Physical Review Letters **84**, 2945 (2000).
[227] P. L. Gammel, D. J. Bishop, J. P. Rice, and D. M. Ginsberg, Physical Review Letters **68**, 3343 (1992).
[228] A. N. Grigorenko, S. J. Bending, I. V. Grigorieva, A. E. Koshelev, T. Tamegai, and S. Ooi, Physical Review Letters **94**, 067001 (2005).
[229] J. C. Martínez, S. H. Brongersma, A. Koshelev, B. Ivlev, P. H. Kes, R. P. Griessen, D. G. de Groot, Z. Tarnavski, and A. A. Menovsky, Physical Review Letters **69**, 2276 (1992).
[230] E. H. Brandt, R. G. Mints, and I. B. Snapiro, Physical Review Letters **76**, 827 (1996).
[231] G. Blatter and V. Geshkenbein, Physical Review Letters **77**, 4958 (1996).
[232] M. Zehetmayer, M. Eisterer, J. Jun, S. M. Kazakov, J. Karpinski, A. Wisniewski, and H. W. Weber, Physical Review B **66**, 052505 (2002).
[233] S. Mukherji and T. Nattermann, Physical Review Letters **79**, 139 (1997).
[234] M. Leung, J. Low Temp. Phys. **12**, 215 (1973).
[235] M. Leung and A. Jacobs, J. Low. temp. Phys. **11**, 395 (1973).
[236] A. Brinkman, A. A. Golubov, H. Rogalla, O. V. Dolgov, J. Kortus, Y. Kong, O. Jepsen, and O. K. Andersen, Physical Review B **65**, 180517 (2002).
[237] M. R. Eskildsen, M. Kugler, S. Tanaka, J. Jun, S. M. Kazakov, J. Karpinski, and Ø. Fischer, Physical Review Letters **89**, 187003 (2002).
[238] G. Rubio-Bollinger, H. Suderow, and S. Vieira, Physical Review Letters **86**, 5582 (2001).